
KERR-MEDIATED SYMMETRY BREAKING OF COUNTERPROPAGATING LIGHT IN MICRORESONATORS

Leonardo Del Bino

Submitted for the Degree of Doctor of Engineering

HERIOT-WATT UNIVERSITY

SCHOOL OF ENGINEERING AND PHYSICAL SCIENCES

ACADEMIC SUPERVISOR: Derryck T. Reid

INDUSTRIAL SUPERVISORS: Pascal Del'Haye

Helen Margolis

October 2020

Abstract

Nonlinear Optics has been a source of surprises for physicists for almost a century comprising both fundamental physics and real-world applications. To access optical nonlinearities, significant light intensities are required; thus nonlinear optics often involves a resonant cavity to amplify the light intensity. Microresonators have proven to be an ideal platform for this kind of experiment since the cavity mode area can be as small as a few μm^2 and their high Q-factor traps light for many round trips while more light is coupled in. Also, light interacts with the nonlinear material, of which the resonator is made, for the whole round trip. However, the interaction between counter-propagating light in microresonators is still a relatively unexplored field.

This thesis reports on the first observation of Kerr-induced spontaneous symmetry breaking in a microresonator, whereby light can circulate in only one direction inside the resonator. I develop a theoretical model describing the steady-state solutions and the dynamics of how the symmetry-broken regime responds to the input changes. I show experimentally how the symmetry breaking can be used to realise all-optical isolator, circulators, memories and logic gates. These devices, based on the Kerr-nonreciprocity, represent a promising alternative for the realisation of integrated all-optical passive photonics circuits.

To water.
In all its forms
and manifestations.

Acknowledgements

I would like to acknowledge the EPSRC, NPL, CDT in Applied photonics and ERC for funding my EngD and my research.

This thesis was possible. Full stop. When someone starts a PhD, the submission of a thesis is expected. It would have been written sooner or later, better or worse, maybe on a different topic.

The life experiences of the past four years, the work environment and all the little things that are hidden in between the bits of this pdf document... These are the things that would not have been possible without all the great people I met along the way. I will clumsily try to express my gratitude to them in the next few lines.

My sincere gratitude goes to my supervisors.

To Pascal for his passionate support as a supervisor and his trust and respect as a colleague. I could not have asked for better.

To Derryck for his cordial advice. And for being hands-off when everything was smooth but prompt and thorough at the minimum sign of an issue.

To Helen for being my anchor and point of reference at NPL, and for stepping in as a supervisor in the last turbulent times on my EngD.

I owe a lot of what I learned to my research group:

Jonathan that patiently trained me when I was an unfledged PhD and answered all my questions, and they were not few.

My “twin” Michael that gave me a new perspective on theoretical physics and the funny discussions on imaginary optical power.

Thanks to Shuangyou for the hours spent together in the yellow room and for being a model for what hard-working and focus means.

George that got me into gliding, kept me up with ~~daily~~ hourly memes, and significantly delayed the submission of this thesis.

Niall that continuously sparked new ideas and sometimes even EDFAs.

Andreas Diameter that tough me meticulousness and the difference between \emptyset and \emptyset .

Thanks to all the colleagues at NPL. Charles (the best random neighbour that could happen to me), Alissa (for making it impossible to be sad), Billy (for pushing me up the wall), Sean, Alvise, Marco, Nicola, Beppe, Caitlyn, Ed, Emma, Ben and all the other colleagues and friends in the UK. Not to mention a bunch of physicists and friends from the University of Florence: Elisa, Jack, Matteo, Giambra, Eleonora, Giovanni. You had a positive influence on who I am as a physicist and as a person. A thought goes to my CDT in Applied Photonics colleagues: Hollie, Andy, Stefi, Juan, Peter, Chris and $2\times$ Ben, I really enjoyed the months I spent with you in Glasgow and every time we met again, I regret not spending more time with you.

A final appreciation goes to my family that made me what I am now, and hopefully are happy with the result. To my father Marcello for passing down to me the passion for motorbikes and technology and to my mother Simona for supporting me from my home-country and missing me but trying to hide it. Finally thanks to my ~~girlfriend~~ wife Cele for keeping my life in movement, as water.

Grazie di cuore.

LEONARDO DEL BINO

April 2020



E-Thesis Submission

Name of student: Leonardo Del Bino

Student ID: H00247391

School: EPS

Degree sought: EngD

Supervisor(s): Derryck Reid

Title of Thesis:

**Kerr-mediated symmetry breaking
of counterpropagating light
in microresonators**

Limited Access approved: Yes N/A

Declaration

In accordance with the appropriate regulations I hereby submit an electronic copy of my thesis and I declare that:

- 1) The thesis embodies the results of my own work and has been composed by myself.
- 2) Where appropriate, I have made acknowledgement of the work of others and have made reference to work carried out in collaboration with other persons.
- 3) The thesis is the correct version of the thesis for submission and is the same version as submitted presentation bound theses*.
- 4) My thesis for the award referred to, deposited in the Heriot-Watt University Library, should be made available for loan or photocopying and be available via the Institutional Repository and subject to such conditions as the Librarian may require.
- 5) I understand that as a student of the University I am required to abide by the Regulations of the University and to conform to its discipline.
- 6) The electronic copy of my thesis has been submitted in the file format specified in the *Submission and Format of Thesis Guidelines*

** Please note that it is the responsibility of the candidate to ensure that the correct version of the thesis is submitted.*

Signature of student: Leonardo Del Bino

Date: 02/10/2020

Research Thesis Submission

Name:	Leonardo Del Bino		
School:	Engineering and Physical Sciences		
Version: <i>(i.e. First, Resubmission, Final)</i>	Final	Degree Sought:	Doctorate of Engineering

Declaration


In accordance with the appropriate regulations I hereby submit my thesis and I declare that:

1. The thesis embodies the results of my own work and has been composed by myself
2. Where appropriate, I have made acknowledgement of the work of others
3. The thesis is the correct version for submission and is the same version as any electronic versions submitted*.
4. My thesis for the award referred to, deposited in the Heriot-Watt University Library, should be made available for loan or photocopying and be available via the Institutional Repository, subject to such conditions as the Librarian may require
5. I understand that as a student of the University I am required to abide by the Regulations of the University and to conform to its discipline.
6. I confirm that the thesis has been verified against plagiarism via an approved plagiarism detection application e.g. Turnitin.


ONLY for submissions including published works

7. Where the thesis contains published outputs under Regulation 6 (9.1.2) or Regulation 43 (9) these are accompanied by a critical review which accurately describes my contribution to the research and, for multi-author outputs, a signed declaration indicating the contribution of each author (complete)
8. Inclusion of published outputs under Regulation 6 (9.1.2) or Regulation 43 (9) shall not constitute plagiarism.

* Please note that it is the responsibility of the candidate to ensure that the correct version of the thesis is submitted.

Signature of Candidate:		Date:	02/10/2020
-------------------------	---	-------	------------

Submission

Submitted By <i>(name in capitals)</i> :	Leonardo Del Bino
Signature of Individual Submitting:	
Date Submitted:	02/10/2020

For Completion in the Student Service Centre (SSC)

Limited Access	Requested	Yes	No	Approved	Yes	No
<i>E-thesis Submitted (mandatory for final theses)</i>						
Received in the SSC by <i>(name in capitals)</i> :				Date:		

Inclusion of Published Works

Declaration

This thesis contains one or more multi-author published works. In accordance with Regulation 6 (9.1.2) I hereby declare that the contributions of each author to these publications is as follows:

Citation details	
Author 1	
Author 2	
Signature:	
Date:	

Citation details	
Author 1	
Author 2	
Signature:	
Date:	

Citation details	
Author 1	
Author 2	
Signature:	
Date:	

Internal Examiners Declaration Form
 (This form must be typed and all sections completed)

Candidate's Name:	Leonardo Del Bino	Heriot-Watt Person ID:	H00247391
School:	EPS/IPaQS	Degree Sought:	EngD
Campus: <i>(If off-campus please state location)</i>	Edinburgh		

Declaration

- I confirm that the corrections to the thesis of the above named have been carried out to the satisfaction of the examiners Yes No N/A
- I confirm that the Joint Examiners Report Form states recommendation (b) - 'Award degree following satisfactory completion of minor corrections' Yes No

If yes,

- Please provide details below to demonstrate that the particular corrections are satisfactory.
- Confirm that the corrections have been completed within the period of time given, if not please give an explanation.

After checking the final manuscript I can certify that the candidate has implemented all the corrections as requested by both internal and external examiners. Corrections pertained plots, figure captions, main text, table, list of references, paragraphs titles, and few small structural changes.

- I confirm that the Joint Examiners Recommendation was originally: Re-submit (decision (c or d) on the previous Joint Examiners Form) Yes No
- I confirm that thesis title has changed since the temporary thesis was submitted. **If yes,** please provide details of amended title here: Yes No

- I confirm that I have seen the presentation (final bound) thesis and it has been bound in accordance with University regulations. Yes

Electronic Thesis

As the Internal Examiner, I confirm that the student has prepared an electronic copy of the thesis in accordance with University guidelines **and it is an exact copy of the final bound thesis.**

Yes No

In accordance with [Heriot-Watt University Regulations](https://www.hw.ac.uk/students/studies/examinations/thesis.htm), all students submitting research theses to the University for the awards of Doctor of Philosophy, Doctor of Philosophy by Published Research, Doctor of Engineering, Doctor of Business Administration, Master of Philosophy and/or Higher Degrees of Master (Research), must provide an electronic version of their final thesis. Further information on electronic thesis submission is available in the Submission and Format of Thesis Guidelines, available at <https://www.hw.ac.uk/students/studies/examinations/thesis.htm>

Internal Examiner

Print Name:	Marcello Ferrera	Date:	01-10-2020
-------------	------------------	-------	------------

Signature:		School:	EPS/IPaQS
------------	---	---------	-----------

Notes

1. Please note that under current University Regulations one presentation (final bound) and one electronic copy of the thesis are required for final submission.
2. The Internal Examiner's Declaration Form should be submitted along with the presentation (final bound) and electronic copy of the thesis to the Student Service Centre.

Contents

Acknowledgements	2
List of Symbols and notation	29
List of Acronyms	30
1 Introduction	32
1.1 The Kerr effect	33
1.2 Microresonators	34
1.3 Kerr effect in microresonators	34
1.4 The unforeseen	36
1.5 Why?	37
1.6 Aim	39
1.7 Outline	39
2 Microresonators	41
2.1 Coupling of light into the microresonator	41
2.1.1 Low-loss (Lorentzian) approximation	46
2.1.2 Light loss channels (bending, absorption, scattering)	49
2.2 Measurable parameters	52
2.2.1 Linewidth	52
2.2.2 Coupling efficiency	54
2.2.3 Free spectral range	55
2.2.4 Finesse	56
2.2.5 Q-factor	56
2.3 Normalised theory	57
2.3.1 Electric field, power and intensity	58
2.3.2 Characteristic frequency	59

2.3.3	Coupled Power	59
2.4	Thermal effects	61
2.4.1	Thermoelasticity and thermorefractivity	62
2.4.2	Passive thermal locking	62
2.4.3	Neglecting the thermal effect	64
2.5	Why Microresonators?	65
2.5.1	The quest for high-intensity	65
2.6	Platforms and microfabrication	68
2.6.1	Modes inside the resonator	69
2.7	Glass rods	70
2.8	Microdisks and Microtoroids	73
2.8.1	Photolithography	74
2.8.2	HF etching	77
2.8.3	XeF ₂ etching	78
2.8.4	Reflowing	79
2.9	Alternative microresonator platforms	81
2.10	Tapered optical fibres	84
2.11	Beyond fused silica	87
2.12	Conclusions	88
3	Symmetry breaking	90
3.1	The Kerr effect	91
3.1.1	XPM is twice as much as SPM	91
3.1.2	Kerr effect in a ring resonator	94
3.1.3	Power dependency of the refractive index	97
3.1.4	Characteristic power for the Kerr Effect	97
3.2	Symmetry breaking	101
3.2.1	Qualitative description	101
3.2.2	Theory	103
3.2.3	Special points	107
3.3	Methods	109
3.4	Results and discussion	112
3.4.1	Measuring the resonator parameters	116

4	Microresonator-based implementation of isolators and circulators	119
4.0.1	The Faraday isolator	120
4.0.2	What is an isolator?	121
4.0.3	Miniaturising isolators	123
4.1	Coupling two fibres to a microresonator	124
4.2	Isolator	130
4.2.1	Optimising the parameters	130
4.2.2	Methods	135
4.2.3	Results and discussion	137
4.2.4	Simulations for other materials	139
4.3	Circulator	140
4.3.1	Methods	140
4.3.2	Results and discussion	140
4.4	Conclusions	142
5	All-optical memory and switching dynamics	144
5.1	Introduction	144
5.2	Theory	145
5.3	Time-step simulation	148
5.4	Methods	150
5.4.1	Square waves: AOM vs EOM	151
5.4.2	EOM overdrive	152
5.5	Results and discussion	155
5.5.1	Hysteresis	155
5.5.2	Effect of the input parameters on the switching profile	158
5.5.3	Speed and Eye diagram	164
5.5.4	Different materials and platforms	168
5.6	Alternative technologies	170
5.7	Applications	172
5.7.1	Memory	172
5.7.2	Router or switch	173
5.7.3	Logic gate	173
5.8	Conclusions	177

6	Conclusions and outlook	178
6.1	Summary	178
6.2	Outcomes	178
6.3	Outlook	180

List of Figures

1.1	Illustration of a microresonator based frequency comb. (1) Degenerate four-wave mixing and (2) Non-degenerate four wave mixing. Adapted from [30]	35
2.1	A schematic of the coupling region and the parameters used to describe the coupling of a resonator to a tapered fibre. t and k are the transmission and coupling respectively. α is the round trip transmission.	43
2.2	Comparison between the exact model and the Lorentzian approximation. In blue, the shape of a resonance without the small angle approximation, and in orange, the same resonance in small angle approximation. $\alpha = 0.8$, $t = 0.9$	48
2.3	(a) Refractive index profile of a disk resonator, (b) Modelling the curvature of the resonator as a gradient in the refractive index. Adapted from [66].	50
2.4	Definition of the coupled power. In blue, a schematized transmission spectrum of a microresonator resonance when scanning the laser towards lower frequency. The cold resonance is at ω_0 but it is deformed by the thermal and Kerr effect. The input power P_{in} is equal to the transmitted power P_{trans} outside the resonance. The coupled power P_{coup} is measured as the power missing from the out of resonance transmission.	61
2.5	Thermal effects. (a) the transmitted power through the taper as a function of the laser frequency of a high-Q resonance. The different traces have been acquired at different scanning speed and aligned at the cold cavity resonance. (b) the thermal triangle amplitude, measured as the difference between the resonance and the point of jumping out, as a function of the laser scan speed.	63

2.6	A sea turtle skimming the sea surface and, above, the total internal reflection from the water-to air interface.	68
2.7	Intensity of the optical modes inside a round resonator calculated with COMSOL Multiphysics. Pictures show a radial section of a resonator with 1 mm rod diameter and 50 μm radius of curvature at a wavelength of 1550 nm. Panel (a) shows the fundamental mode, the four panels (b-e) show some of the higher order modes.	69
2.8	Fabrication of glass rod microresonators. On the left, a photograph of the CO ₂ machining setup. One of the galvo mirrors and the focusing lens are visible in the foreground, the spindle is on the left and the air extractor is on the right. On the background the beam-block is visible and part of the enclosure and imaging camera are on the top. Middle, a machined glass rod resonator. Right, a sketch clarifying the geometry of the system. The three panels have the same perspective.	71
2.9	Steps of the photolithographic process. a) Thermally oxidised Si wafer. b) Spin coating. c) Exposure. d) Development. e) HF wet etching. f) Photoresist removal. g) XeF ₂ dry etching. h) CO ₂ laser reflowing.	74
2.10	Photomask used in the microdisks and microtoroids fabrication. The black color correspond to the parts covered in Cr. The top row contains disks with diameter of 20, 30 and 40 μm , there are also some alignment features for the reflow CO ₂ laser. The mid row contains larger resonators from 1 mm to 4 mm that do not need alignment feature. The bottom row is a pattern of resonators slightly tilted with respect to the lattice structure. Cleaving this pattern likely results in having a disk on the edge of the chip for prism coupling.	76
2.11	Schematic of the XeF ₂ etching machine as represented on the control software. The red circles represent electro-actuated valves.	78
2.12	Scanning electron microscope images. a) Microdisc resonator not reflowed with the CO ₂ laser. b) Microtoroid resonator after the CO ₂ laser reflowing. c) The same resonator as b) seen from the side.	80
2.13	Three kind of resonators. (a) Microsphere. (b) Microtoroid. (c) Microbottle. Adapted from [99].	82

2.14	A Si_3N_4 waveguide resonator and waveguide on SiO_2 substrate. Courtesy of Shuangyou Zhang.	83
2.15	Schematic of the tapering setup. The fibre is clamped on translation stages that are pulled apart while the fibre is heated to the softening point. The source of heat could be either a electric oven or an hydrogen flame.	84
2.16	Tapering setups. On the left, the one based on a ceramic heater that is the white cube in the centre of the picture. On the right, the setup based on the H_2 flame. The brass nozzle emitting the flame is visible in the centre of the picture.	85
3.1	Illustration of the Kerr interaction between counter-propagating light in the case of one direction being significantly more powerful than the other. Adapted from [87].	92
3.2	Definition of the detuning. A plot of the normalised coupled power as the laser (black) is scanned across the resonance towards lower frequencies. The 0 for the x axis is arbitrarily set to the cold cavity resonance frequency (in grey), i.e. the resonance as it appears when the power is too low to observe any nonlinearity. At higher power, the resonance is tilted by the thermal and Kerr effect (blue). The detuning is represented as an orange arrow. The effective resonance (red) moves with the laser (black). The effective detuning, i.e. the difference between the laser frequency and the effective resonance is indicated in green. The frequency axis is reversed to match the experimental measurements shown later.	96
3.3	Illustration of the symmetry breaking. At low power, both directions couple equally into the resonator resulting in a standing wave in the resonator. Increasing the input power splits the resonance frequency so that only one random direction couples into the resonator. Adapted from [87].	101

3.4	Step by step description of the symmetry breaking. The laser frequency is represented in black. Coupled powers in each direction are represented by the red and blue dots while the resonance is shown in the same colour. (a) The initial symmetric state with light from both direction equally coupled into the resonator on the high-frequency side of the resonance. Small perturbations increase the light coupled in the red direction (b), this causes a greater shift away from the resonance in the blue direction (c) resulting in less power coupled. Hence, the red direction is now less shifted by the XPM and moves closer to the resonance (d).	102
3.5	On the left, plot of the solving function s for input power $\tilde{p} = 1.9$ and detuning of $\delta = -3$. On the right, the bubble with the detuning of interest highlighted.	105
3.6	Same as in Fig. 3.5 for $\tilde{p} = 3$ and $\delta = -5$	105
3.7	Same as in Fig. 3.5 for $\tilde{p} = 5.5$ and $\delta = -5.8$. (The 2 solutions for low p_1 are overlapped. One arise from the negative branch and one from the positive one)	105
3.8	Solutions of equation Eq. (3.31) for different input power \tilde{p} . Coloured lines represent stable solutions, faint lines represent unstable solutions, and dashed lines represent oscillatory solutions.	106
3.9	Circulating power in the resonator when one direction is fully coupled. In blue, the solution corresponding to the tip of the tilted Lorentzian, Eq. (3.38), the circulating power is the same in both directions. The other two solutions appear for $\tilde{p} \geq 2$. In the graph the fully coupled direction is plotted with a line while the power in the other direction is plotted dashed. Orange is Eq. (3.39), green is Eq. (3.40)	108
3.10	Picture of the experimental setup used in Chapters 4 and 5 of this thesis. The microresonator, tapered optical fibres, translation stages and alignment cameras are protected from dust and airflow by an acrylic enclosure. The black optical breadboard is separated from the pneumatically-suspended optical table by sorbothane feet.	110

3.11	Detail of the coupling region. Two USB microscope cameras are used to align the fibres to the resonator on each side and to illuminate the area. Two aluminium brackets hold the tapered fibres (highlighted in red by the background illumination) in the evanescent field of the rod microresonator that can be seen in the middle.	111
3.12	Scheme of the optical setup used to measure the symmetry breaking. The laser light is amplified and equally split in two branches. An attenuator on each branch allows to precisely balance the power in the two directions. A pair of circulators allow to send light in counter-propagating directions into the tapered fibre coupled to the resonator and observe the transmission in each direction. Adapted from [87]. . .	112
3.13	One of the first observed instances of symmetry breaking. The transmitted power through the tapered fibre in both directions is plotted as a function of the laser frequency for two consecutive scans. Adapted from [87].	113
3.14	An example of a tunable potential that leads to spontaneous symmetry breaking. (a) the potential has a single minimum at the point of symmetry with positive second derivative. The ground state is the bottom of the well. (b) There still a single minimum but the second derivative is 0. This is the limit situation before symmetry breaking. (c) The potential is still symmetric and the point of symmetry is a stationary point. However, there are now two possible ground states, each of them does not follow the same symmetry as the potential. . .	114
3.15	(a) Experiment and (b) simulation of the coupled power in the resonator as a function of the laser frequency. The colour red and blue correspond to the direction of light and the brightness of the trace indicate the input power. In both (a) and (b) the input power is 10% higher in the CW direction to prevent random switching. (c) The maximum difference between the power coupled in the two directions. The black dots are calculated from the measurements in (a) and the green line is the theoretical prediction. Adapted from [87]. . .	115

4.1	Scheme of the idea behind the isolator: once the symmetry is broken, light of a given frequency can circulate just in one direction in the resonator. It would be out of resonance in the other direction. Adapted from [51].	119
4.2	Schematic of the coupling region and the parameters used to describe the coupling of a resonator to a tapered fibre. In this chapter the input port will be the one in the bottom left of the figure.	125
4.3	(a) Plot of $\eta_{\text{out,B}}$ as a function of t_B for the value of $\alpha = 0.95$. (b) Plot of $\eta_{\text{in,A}}$ as a function of α for $t_A = 0.9$ and $t_A = 0.97$. The exact value from the alpha model is plotted in blue, the approximated model is in orange. Note that the two models diverge just when one of t_A, t_B, α are significantly less than 1.	128
4.4	Plot of the circulating power P_1 in blue and the transmitted power $\tilde{P}_{2,\text{out}}$ in orange, for the conditions of resonance and critical coupling at the input $\kappa_A = \gamma_0 + \kappa_B$ and for resonator losses of $\alpha = 0.95$	132
4.5	(a) Simulation of the transmission through the isolator in the condition of equal coupling (yellow) and critical coupling at the input (red) (higher is better). All the coupling strengths are normalised to $\gamma_0 = 1$. (b-c) Return power to the input and isolation as a function of the input power for different transmissions (lower is better). The continuous curves are obtained for $T = 25\% \rightarrow \kappa_A = \frac{4}{3}, \kappa_B = \frac{1}{3}$; $T = 50\% \rightarrow \kappa_A = 2, \kappa_B = 1$; $T = 75\% \rightarrow \kappa_A = 4, \kappa_B = 3$. The dotted line represents $T = 50\%$ with equal coupling ($\kappa_A = \kappa_B = 1.21$). The dashed line represents $T = 50\%$ with critical coupling at the output ($\kappa_B = 2, \kappa_A = 1$).	133
4.6	Optical setup for the isolator experiment. Adapted from [51].	135
4.7	Characterisation of the isolator. The data-points and error-bars are from the experimental measurements while the line is the theoretical fit. (a) Power measured at the return photodiode as a function of the input power. Note how for increasing input power, the return power actually decreases. (b) Isolation improves with the input power while insertion loss is roughly constant. (c) The isolation fitted with our model and the extension to different materials with the parameters found in the literature. Adapted from [51].	138

4.8	(a) Scheme and simplified setup of the circulator configuration. (b) Measurement of transmission through different ports of the circulator as a function of the frequency of the laser. The ideal working point for the circulator is at the resonance point on the right of the graph corresponding to a detuning of -1.2 GHz from the cold resonance. Adapted from [51].	141
5.1	Scheme of the experimental setup used in the switching experiment. .	150
5.2	Fit of the EOM response to a step function. The traces for the fit (green) and the measure (blue) are almost indistinguishable. The red trace is the difference between the two multiplied by a factor of 100. .	153
5.3	The response of the EOM to a square wave input without modifications (a), with a single component exponential fit overdrive (b), and with three components overdrive (c). Pink \rightarrow the output voltage of the function generator on a high impedance load. Yellow \rightarrow the voltage at the EOM input. Green \rightarrow optical power transmitted through the EOM. The graphs represent a time span of $200 \mu\text{s}$	154
5.4	The EOM response without overdrive (left) and with overdrive(right). Pink \rightarrow the output of the function generator on a high impedance load. Yellow \rightarrow the voltage at the EOM input. Green \rightarrow optical power transmitted through the EOM.	155
5.5	Different regimes of symmetry breaking and hysteretical behaviour. (a) A contour plot of the solution of the symmetry breaking equations as a function of the detuning. The black thick line is the solution for equal input power in both directions as already seen in Chapter 3. The case of imbalanced input is colour coded in red and blue and the three regimes are highlighted. (b) A measure of the different regimes. The laser is scanned through the resonance while the power imbalance oscillates. The inset shows the same resonance with equal powers in both directions. Adapted from [87].	156
5.6	Panels (a-f) Hysteresis profile for increasing circulating power in the resonator. Panel (g) Amplitude of the hysteresis, a comparison between the theoretical model and the experiment. Adapted from [52]. .	157

5.7	Definition of the modulation amplitude for a signal around its average power as used in this chapter. In this example $P_{\text{avg}} = 2.5P_0$ and $M = 60\%$	160
5.8	The input signal in each direction (blue \rightarrow CW, red \rightarrow CCW) used to measure the response to different modulation amplitude. A cycle of the signal is highlighted: part (a) and (b) of the signal are constant while (c) changes slightly every cycle. Adapted from [52].	161
5.9	Switching profile as a function of the modulation amplitude. On the left, a simulation of the switching profile for the input in Fig. 5.8 and the following parameters: $P_{\text{avg}} = 3.7P_0$, $\delta = -3.5\gamma$, $Q = 1.6 \times 10^8$, modulation amplitude ranging from 0% to 70%. On the right, the measurement of the switching profile with the same Q and the same input as the simulation. Adapted from [52].	162
5.10	Switching profile as a function of the total power in the resonator, for a modulation amplitude of 70% and a Q-factor of 10^8 . Adapted from [52].	163
5.11	Switching profile as a function of the average power offset between the two input directions. In the yellow curve the levels are equal for both directions $P_{\text{HIGH}} = 4P_0$ and $P_{\text{LOW}} = 1P_0$. This is gradually changed maintaining the absolute modulation amplitude to $P_{\text{CCW}} = 0 \sim 3$ and $P_{\text{CW}} = 2 \sim 5$. The other parameters are: $\gamma = 1$ MHz, $\delta = -3.5\gamma$	164
5.12	Switching profile as a function of the detuning. The detuning varies from -1 (yellow) to -4 (black). The simulation parameters are: $P_{\text{avg}} = 2.5P_0$, modulation amplitude of 60%, $\gamma = 1$ MHz corresponding to $Q = 10^8$	164
5.13	An example of a random bit input sequence.	165
5.14	Eye diagram of the microresonator used as optical memory for different input bitrates. (a) 75 kbps, (b) 1.8 Mbps, (c) 3.8 Mbps, and (d) 4.9 Mbps. Adapted from [52].	166
5.15	One of the preliminary measurements of the eye diagram for a modulation amplitude of 50% performed with a single tapered fibre coupled to the resonator. (Top) the input signal, (bottom) the coupled power calculated from the transmission.	167

5.16	Expected bitrate and threshold power for different materials. *Only for silicon a wavelength of 3.1 μm is used instead of 1.55 μm . Adapted from [52].	169
5.17	Simulation of the logic gate A & \overline{B} . The lower part of each panel shown the inputs A and B , while the upper part shows the output Q and the other circulating direction, not used in the logic gate x . The value of ξ for each panel is 0.2(a), 0.5(b), 0.8(c).	176
5.18	Experimental results of the logic gate setup. Panel (a) shows the input powers A in red and B in blue, panel (b) shows the output. Adapted from [53].	177

List of publications

Publications

- Preprint** A. Svela, J. Silver, L. Del Bino, et al., “Coherent suppression of backscattering in optical microresonators” arXiv:2002.12379 [physics.optics] (27 Feb 2020)
- Preprint** L. Del Bino, et al., “Optical memories and switching dynamics of counterpropagating light states in microresonators” arXiv:2002.02954 [physics.optics] (7 Feb 2020)
- Preprint** J. Silver, L. Del Bino, et al., “A Nonlinear Enhanced Microresonator Gyroscope”, arXiv:2001.05479 [physics.optics] (15 Jan 2020)
- Article** N. Moroney, L. Del Bino, et al., “Logic Gates Based on Interaction of Counterpropagating Light in Microresonators”, *Journal of Lightwave Technology*, vol. 38 no. 6 pp. 1414-1419, (15 Mar 2020)
doi:10.1109/JLT.2020.2975119
- Article** S.Zhang, J. Silver, X. Shang, L. Del Bino, N. Ridler, and P. Del’Haye, “Terahertz wave generation using a soliton microcomb”, *Optics Express* **27** (24), 35257-35266 (18 Nov 2019)
doi:10.1364/OE.27.035257
- Article** M. Rowley, L. Del Bino, et al., “Thermo-optical pulsing in a microresonator filtered fiber-laser: a route towards all-optical control and synchronization”, *Optics Express* **27** (14), 19242-19254 (25 Jun 2019)
doi:10.1364/OE.27.019242
- Article** S. Zhang, L. Del Bino, et al., “Sub-milliwatt-level microresonator solitons with extended access range using an auxiliary laser”, *Optica* **6** (2),

206-212 (19 Feb 2019)

doi:10.1364/OPTICA.6.000206

- Article** F. Copie, M. Woodley, L. Del Bino, J. Silver, S. Zhang, and P. Del’Haye, “Interplay of Polarization and Time-Reversal Symmetry Breaking in Synchronously Pumped Ring Resonators”, *Physical Review Letters* **122**, 013905 (10 Jan 2019)
doi:10.1103/PhysRevLett.122.013905
- Article** G. Enzian, L. Del Bino, et al., “Observation of Brillouin optomechanical strong coupling with an 11 GHz mechanical mode”, *Optica* **6** (1), 7-14 (21 Dec 2018)
doi:10.1364/OPTICA.6.000007
- Article** M. Woodley, L. Del Bino, et al., “Universal symmetry-breaking dynamics for the Kerr interaction of counterpropagating light in dielectric ring resonators”, *Physical review A* **98**, 053863 (30 Nov 2018)
doi:10.1103/PhysRevA.95.033835
- Article** L. Del Bino, J. Silver, M. Woodley, S. Stebbings, X. Zhao, and P. Del’Haye, “Microresonator isolators and circulators based on the intrinsic nonreciprocity of the Kerr effect”, *Optica* **5** (3), 279-282 (9 Mar 2018)
doi:10.1364/OPTICA.5.000279
- Article** E. Lucioni, L. Del Bino, et al., “A new setup for experiments with ultracold dysprosium atoms”, *The European Physical Journal Special Topics* **226**, 12:2775–2780 (26 Jul 2017)
doi:10.1140/epjst/e2016-60387-6
- Article** J. Silver, C. Guo, L. Del Bino, and P. Del’Haye, “Kerr superoscillator model for microresonator frequency combs”, *Physical review A* **95**, 033835 (27 Mar 2017)
doi:10.1103/PhysRevA.95.033835
- Article** L. Del Bino, J. Silver, S. Stebbings, P. Del’Haye, “Symmetry Breaking of Counter-Propagating Light in a Nonlinear Resonator”, *Scientific Reports* **7**, 43142 (21 Feb 2017).
doi:10.1038/srep43142

Conferences

2019

- Poster** L. Del Bino, “Towards all-Optical computing”, *PGI conference*, NPL, Teddington 6 Nov 2019
- Proceeding** M. Rowley, L. Del Bino et al., “Thermo-optical pulsing in a microresonator filtered fiber-laser”, *Advanced Photonics Congress*, Burlingame, CA, 29 Jul-1 Aug 2019,
- Proceeding** J. Silver, L. Del Bino et al., “Critical Dynamics of a Nonlinear Enhanced Microresonator Gyroscope”, *CLEO/Europe-EQEC*, Munich, Germany, 23-27 Jun 2019,
doi:10.1109/CLEOE-EQEC.2019.8872419
- Proceeding** L. Del Bino et al. “All-Optical Switching in Microresonators using the Kerr Nonreciprocity”, *CLEO/Europe-EQEC*, Munich, Germany, 23-27 Jun 2019,
doi:10.1109/CLEOE-EQEC.2019.8873277
- Proceeding** M. Rowley, L. Del Bino et al. “Thermo-Optical Pulsing in a Resonator-Based Laser”, *CLEO/Europe-EQEC*, Munich, Germany, 23-27 Jun 2019,
doi:10.1109/CLEOE-EQEC.2019.8873107
- Poster** G. Ghalanos, L. Del Bino et al. “Direct Measurement of Cross-Phase Modulation in Microresonators”, *CLEO/Europe-EQEC*, Munich, Germany, 23-27 Jun 2019,
doi:10.1109/CLEOE-EQEC.2019.8872237
- Poster** M. Woodley, L. Del Bino et al. “Spontaneous Symmetry Breaking, Oscillations, and Chaotic Regimes in Bidirectionally-Pumped Ring Resonators”, *CLEO/Europe-EQEC*, Munich, Germany, 23-27 Jun 019,
doi:10.1109/CLEOE-EQEC.2019.8872598
- Proceeding** A. Svela, L. Del Bino et al. “Spontaneous Symmetry Breaking Based Near-Field Sensing with a Microresonator”, *CLEO*, San Jose, CA, 5-10 May 2019
doi:10.23919/CLEO.2019.8749945

Proceeding S. Zhang, L. Del Bino et al. “Microwatt-Level Soliton Frequency Comb Generation in Microresonators Using an Auxiliary Laser”, *CLEO*, San Jose, CA, 5-10 May 2019
doi:10.23919/CLEO.2019.8749700

Proceeding N. Moroney, L. Del Bino et al. “Logic Gates based on Interaction of Counterpropagating Light in Microresonators”, *CLEO*, San Jose, CA, 5-10 May 2019
doi:10.23919/CLEO.2019.8748932

2018

Talk L. Del Bino, J. Silver, M. Woodley, P. Del’Haye, “Isolators and Circulators Based on Kerr Nonreciprocity in Microresonators”, *PGI conference*, Glasgow, UK, 3 Oct 2018

Proceeding F. Copie, L. Del Bino, et al. “Temporal and Polarization Symmetry Breaking in Ring Resonators”, *FiO/LS*, Washington, DC, 16-20 Sep 2018
doi:10.1364/fio.2018.jw4a.32

Proceeding L. Del Bino “Microresonator isolators and circulators based on the intrinsic nonreciprocity of the Kerr Effect”, *Photon2018*, Aston University, Birmingham, UK 2-6 Sep 2018
doi:10.1364/iprsn.2018.jw3i.6

Proceeding J. Silver, L. Del Bino, et al. “A Diode Made of Light - Optical Isolators and Circulators Based on the Intrinsic Nonreciprocity of the Kerr Effect”, *Advanced Photonics congress*, Zurich, Switzerland, 2-5 Jul 2018
doi:10.1364/iprsn.2018.jw3i.6

Talk L. Del Bino, J. Silver, M. Woodley, and P. Del’Haye, “Isolators and Circulators Based on Kerr Nonreciprocity in Microresonators”, *CD-TAP annual conference*, St. Andrews, UK, 15 Jun 2018

Proceeding M. Woodley, L. Del Bino, J. Silver, S. Zhang, and P. Del’Haye “Interaction of Counter-Propagating Light in Microresonators: Theo-

retical Model and Oscillatory Regimes”, *CLEO*, San Jose, CA, 13-18 May 2018
doi:10.1364/CLEO_QELS.2018.FM3E.3

Proceeding L. Del Bino, M. Woodley, J. Silver, S. Zhang and P. Del’Haye “Switching Dynamics of Counter-propagating Light States in Microresonators”, *CLEO*, San Jose, CA, 13-18 May 2018
doi:doi.org/10.1364/CLEO_SI.2018.SM1D.4

Webinar L. Del Bino, “Light with Light Interaction: Applications of Symmetry Breaking and Kerr Non-Reciprocity in Microresonators”, *CDTAP webinars*, 21 Feb 2018

2017

Poster L. Del Bino, et al., “Isolators and Circulators Based on Kerr Non-reciprocity in Microresonators”, *653. W.E. Heraeus Seminar “Optical Microcavities and Their Applications”*, Physikzentrum, Bad Honnef, Germany, 5-10 Nov 2017.

Talk L. Del Bino, and M. Woodley, “Spontaneous Symmetry Breaking in Microresonators: Theory and Applications”, *PGI conference*, NPL, Teddington, 30 Oct 2017

Proceeding L. Del Bino, J. Silver, S. Stebbings and P. Del’Haye “Spontaneous symmetry breaking of counterpropagating light in microresonators”, *CLEO/Europe-EQEC*, Munich, Germany, 25-29 Jun 2017,
doi:10.1109/CLEOE-EQEC.2017.8087535

Proceeding L. Del Bino, J. Silver, X. Zhao, S. Stebbings and P. Del’Haye “Isolators and circulators based on kerr nonreciprocity in microresonators”, *CLEO/Europe-EQEC*, Munich, Germany, 25-29 Jun 2017,
doi:10.1109/CLEOE-EQEC.2017.8086519

Proceeding J. Silver, L. Del Bino and P. Del’Haye, “A nonlinear enhanced microresonator gyroscope”, *CLEO/Europe-EQEC*¹, Munich, 25-29 Jun 2017,
doi:10.1109/CLEOE-EQEC.2017.8086527

¹Conference on Lasers and Electro-Optics Europe & European Quantum Electronics Conference

- Proceeding** J. Silver, C. Guo, L. Del Bino and P. Del’Haye, “Kerr superoscillator model for microresonator frequency combs”, *CLEO/Europe-EQEC*, Munich, 25-29 Jun 2017,
doi:10.1109/CLEOE-EQEC.2017.8087481
- Poster** L. Del Bino, J.P. Godoy Vilar, et al., “Short-distance Free-space Optical Communication with a Non-Stationary Receiver”, *CDTAP annual conference*, Heriot-Watt University, UK, 23 Jun 2017
- Proceeding** L. Del Bino, J. Silver, S. Stebbings and P. Del’Haye “Spontaneous symmetry breaking of counterpropagating light in microresonators”, *CLEO²*, San Jose, CA, 14-19 May 2017.
doi:10.1364/CLEO_QELS.2017.FTh3D.6
- Proceeding** L. Del Bino, J. Silver, X. Zhao, S. Stebbings and P. Del’Haye “Isolators and circulators based on Kerr nonreciprocity in microresonators”, *CLEO*, San Jose, CA, 14-19 May 2017
doi:10.1364/CLEO_SI.2017.SM2N.6
- Proceeding** J. Silver, C. Guo, L. Del Bino and P. Del’Haye “Kerr superoscillator model for microresonator frequency combs”, *CLEO*, San Jose, CA, 14-19 May 2017
doi:10.1364/CLEO_AT.2017.JTh2A.67
- Proceeding** X. Zhao, J. Silver, L. Del Bino, and P. Del’Haye “Dual comb generation in a single microresonator”, *CLEO*, San Jose, CA, 14-19 May 2017
doi:10.1364/CLEO_SI.2017.STh3L.4
- Proceeding** J. Silver, L. Del Bino and P. Del’Haye, “A nonlinear enhanced microresonator gyroscope”, *CLEO*, San Jose, CA, 14-19 May 2017
doi:10.1364/CLEO_SI.2017.SM1M.2

2016

- Poster** L. Del Bino, “Symmetry Breaking of Counter-Propagating Light in a Nonlinear Resonator”, *MFCA*, organised by EPFL, Monte Verità, Switzerland, 6 Jul 2016

²Conference on Lasers and Electro-Optics

Poster L. Del Bino, “Microresonator-based frequency combs”, *SUSSP 72*, St.Andrews, Scotland, 25 Jun 2016

Patents

Patent L. Del Bino, S. Stebbings, P. Del’Haye, J. Silver, “Nonreciprocal light propagation systems and methods”, filed: GB1611046.2, 24 Jun 2016; extended: WO/2017/221028A1, 28 Dec 2017 and US 2019 / 10503048

List of Symbols and notation

Unless specified, the lowercase letters indicate the dimensionless or normalised quantities, while the uppercase letters indicate the quantities with dimensions.

p	circulating power in the resonator
\tilde{p}	input power at the coupling point
δ	detuning between the laser and cold resonance frequency
m	mode number
P	optical power
I	optical intensity
E	electric field
\tilde{P} or P_{in}	input power at the coupling point
P_{circ}	optical power circulating in the resonator
P_0	characteristic power for the Kerr effect
P_{th}	threshold power to observe symmetry breaking $P_{\text{th}} = 1.54P_0$
P_{trans}	optical power transmitted through the tapered fibre
P_{coupl}	optical power coupled into the resonator, $P_{\text{coupl}} = P_{\text{in}} - P_{\text{trans}}$
Δ	detuning between the laser and cold resonance frequency. Note: Δ followed by another quantity indicates a variation of that quantity.
t	electric field transmission at the coupling point
k	electric field coupling at the coupling point
α	electric field round trip transmission of the resonator
θ	phase accumulated in one round trip of the resonator
γ	half width half maximum coupled linewidth
κ	coupling half linewidth
η	coupling efficiency
$\chi^{(n)}$	n-th order susceptibility
ε_0	vacuum permittivity
c	speed of light in vacuum
L	length of the resonator round trip
r	resonator radius
d	resonator diameter

A_{eff}	effective mode cross-sectional area
V_{eff}	effective mode volume
ω	angular frequency
λ	wavelength
ν	frequency
n, n_0	refractive index
n_2	nonlinear refractive index
Q	Q-factor
\mathcal{F}	finesse

The subscripts follow the notation below:

1, 2, A, B or CW, CCW	in Chapters 3, 4, and 5, indicate that the quantity refers to one or the other direction
1, 2	in Chapter 1 indicate that the quantity refers respectively to the tapered fibre and the resonator
i, t	in Chapter 1 indicate that the quantity refers respectively to the input and the transmission of the coupling point
crit	the quantity refers to critical coupling condition
res	the quantity refers to resonant condition
0	the quantity refers to the ‘cold’ state, where the power is low enough to neglect thermal and Kerr effects. Furthermore, the quantity refers to the limit of no coupling between tapered fibre and resonator
in	input
trans	transmitted
FSR	referring to free spectral range

List of Acronyms

SPM	Self-phase modulation
XPM	Cross-phase modulation
MI	Modulation instability
WGM	Whispering gallery mode

LLE	Lugiato-Lefever equation
NLSE	Non-linear Schrödinger equation
ECDL	External-cavity diode laser
EDFA	Erbium-doped fibre amplifier
EOM	Electro-optic modulator
AOM	Acousto-optic modulator
CW	Clockwise
CCW	Counter-clockwise
HWHM	Half width half maximum
FWHM	Full width half maximum
FSR	Free spectral range
SEM	Scanning Electron Microscope
OSA	Optical spectrum analyser
c.c.	Complex conjugate

Chapter 1

Introduction

Nothing in life is to be feared, it is only to be understood. Now is the time to understand more, so that we may fear less.

Maria Salomea Skłodowska Curie

Life is nonlinear. Not just because events rarely follow a straight line, but because we are surrounded by nonlinear phenomena. We experience a lot of them daily: the wind flowing around trees, the fact that it is harder and harder to pedal your bike to work the faster you go, the sound of a distorted electric guitar are all examples of nonlinearities. To narrow down the definition, a nonlinear system has outputs that are not simply proportional to the inputs but follow a more complicated functional relation.

There are however forms of nonlinearity that we do not commonly experience in daily life because the inputs never reach values high enough for us to notice the deviation from a linear response. All of us are fascinated by the twin paradox where the sibling travelling at the speed of light comes back from his trip through the universe much younger than the other brother that stayed on Earth. But no twin actually experienced that, not because special relativity is wrong but because the effect is negligible at the speeds that current technology allows.

1.1 The Kerr effect

This thesis deals with one of these nonlinearities: the optical Kerr effect [1, 2]. The Kerr effect is a particular form of optical nonlinearity discovered by John Kerr in 1875, that describes a change in the refractive index of a medium proportional to the intensity of light that propagates through it [3].

The reason why we do not see the light interacting with other light or changing direction depending on its brightness is because the intensity needed for this effect to become significant is extreme. It is not surprising that the first reports of this effect were inside laser cavities or in optical fibres, where the intensity of light is sufficiently high to make these changes of refractive index detectable [4]. In the case of lasers, the intracavity light intensity can be orders of magnitude greater than the laser output because the mirrors constituting the laser cavity recirculate light multiple times. Optical fibres, instead, concentrate the light in a small mode volume, less than $100\ \mu\text{m}^2$. Furthermore, fibres can be several kilometres long and such an interaction length can enhance small effects.

When light intensity has a localised spatial or temporal profile, the change of refractive index is stronger at the point of peak intensity. If light is propagating in a spatially localised profile such as a Gaussian beam, the Kerr effect is manifested as Kerr lensing [5]. Usually the Kerr effect produces an increase of the refractive index of the medium, increasing the optical path length proportionally to the intensity. A converging lens has a similar path length profile, hence high intensity beams propagating in a nonlinear medium tend to self-focus. The combination of a Kerr lens followed by a pinhole transmits slightly less if the input consists of continuous wave radiation rather than pulses. This happens because the higher intensity in pulses focus them through the aperture better than low intensity cw light. This effect is commonly used in mode locked lasers to promote pulsed operation. Light pulses also have a temporal intensity profile, hence the middle of the pulse sees a higher refractive index than the leading and trailing edges. This manifestation of the Kerr effect is called self-phase modulation (SPM) [6, 7].

But the Kerr effect manifests itself even for continuous wave light: any ripple in the time envelope of the intensity induces a corresponding modulation of the refractive index that in turn affects the intensity profile. This phenomenon goes under the name of modulation instability (MI) and, interestingly, was well studied

in water waves as long ago as 1847 [8, 9, 10, 11], before being transported to the field of nonlinear optics [12, 13, 14, 15].

1.2 Microresonators

The other key ingredient of this thesis is microresonators, but what are they? Let us make a step back to 1910 when Lord Rayleigh coined the term “whispering gallery” referring to the property of the dome of St. Paul’s cathedral [16]. A person whispering close to the wall in the gallery at the base of the dome can be heard clearly on the other side. Rayleigh theorised that the sound waves are guided by the gallery, continuously bouncing at shallow angles on the wall. Hence, the wave travels in a confined area reaching the other side with a higher intensity than propagating in every direction across the dome.

The same principle applies to electromagnetic waves in circular dielectric structures. As long as the dielectric has a higher refractive index than the surrounding medium, light is guided by total internal refraction in a closed loop. In 1938 Robert Richtmyer [17] applied the concept of Rayleigh to electromagnetic radiation and, 31 years ago the first fused silica resonator working in the optical domain was realised by melting the tip of an optical fibre [18].

These structures are called whispering gallery mode (WGM) resonators because they use the same principle discovered by Lord Rayleigh. The term microresonator is used when these kinds of cavities are not as large as a cathedral dome but their diameter is from a few tens of microns up to a few centimetres and the mode of the gallery, i.e. the cross-sectional area of the propagating light, is a few μm^2 . Also, to be a resonator, the losses need to be small enough such that light can interfere with itself roundtrip after roundtrip. The interference is constructive if the round trip optical length is a multiple of the wavelength and destructive otherwise.

1.3 Kerr effect in microresonators

We can now see why microresonators are an ideal platform for the study of the Kerr effect and nonlinear optics in general [19]: they combine a mode volume even smaller than optical fibres, with the light recirculation of a cavity. In recent times WGM resonators have been built with incredibly small losses [20, 21, 22, 23]. This

means that resonant light can be trapped inside the ring structure for millions of roundtrips allowing powers up to a megawatt to be concentrated in an area much smaller than the cross-section of a human hair¹.

One of the most notable discoveries was microcombs [24]. Modulation instability, also called four wave mixing or hyperparametric oscillation, is the nonlinear optical process that underpins frequency comb generation in microresonators [25]. The first observations of MI in the optical domain were in 1966 in optical fibres [26, 27]. It was observed in microresonators for the first time in 2004 [28, 29] and can be described in quantum mechanical terms as the annihilation of two pump photons to generate two other photons at different frequencies, generally called the signal and the idler (inheriting their names from electronics). Energy conservation links the frequencies of the four photons by the relation:

$$\omega_{p1} + \omega_{p2} = \omega_s + \omega_i. \quad (1.1)$$

When $\omega_{p1} = \omega_{p2}$ the effect is called degenerate four wave mixing, while in the non degenerate case $\omega_{p1} \neq \omega_{p2}$

This is the mechanism that leads to the generation of the frequency comb. First, degenerate FWM of the pump generates a couple of side bands, then cascaded non-degenerate FWM between the various side bands fills the remaining gaps in the comb as shown in Fig. 1.1.

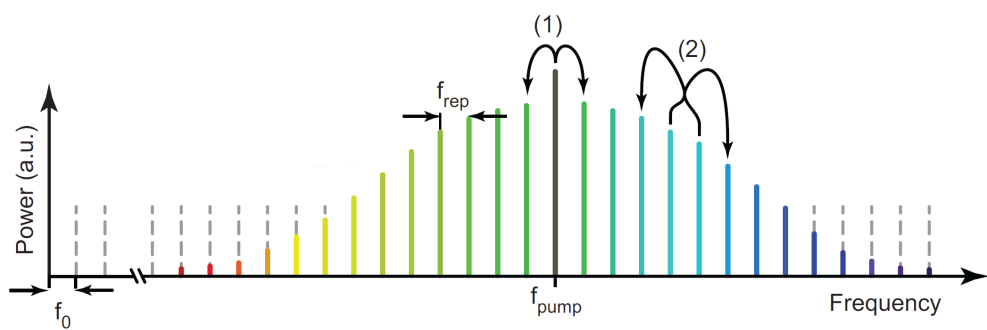


Figure 1.1: *Illustration of a microresonator based frequency comb. (1) Degenerate four-wave mixing and (2) Non-degenerate four wave mixing. Adapted from [30]*

Analysing the comb formation from the temporal point of view, one can imagine that the modulation instability tends to concentrate the propagating light in a series

¹The hair of the author have an average diameter of 90 μm corresponding to a cross sectional area of 8100 μm^2 . Microresonator have cross-sectional areas in a range spanning from 1 μm^2 to 500 μm^2 .

of peaks and, under appropriate pumping conditions, is a single pulse in the cavity called a soliton [31] as described by the Lugiato-Lefever equation (LLE) [32]. The propagation of a soliton in the microresonator results in an output that can be described as a pulsed laser with the repetition rate of the cavity round trip time. The spectrum of this pulsed output corresponds to the one in Fig. 1.1.

The discovery of frequency combs has been a revolution in precision spectroscopy [33]. For the first time, an accurate ruler in the frequency domain was available to finally measure the absolute frequency of atomic transitions, paving the way to the discovery and proof of many of the fundamental laws in atomic physics. Nowadays, frequency combs are used for a wealth of applications in physics [34] but they are still struggling to find their way in technology applications since they are expensive and bulky pieces of equipment that often requires a high degree of control to work properly. Microcombs, on the other hand, are astonishing simple and inexpensive devices, composed of just a continuous wave laser and a circular resonator that could make frequency combs finally available to a broader audience[35].

1.4 The unforeseen

This thesis was supposed to have a different title and describe Kerr frequency combs in microresonators. The first experiment of my EngD aimed to exploit the Kerr effect to generate two frequency combs in the same resonator by using counter propagating light. Ideally, using the same resonator in opposite directions would cancel out most of the differential noise with huge advantages for heterodyne detection [36], also part of the electronics could be shared between the two combs.

When trying to couple light in both directions in a microresonator at low power I observed the expected thermal triangle as shown in Fig. 3.2. However, as the input power increases to reach the four wave mixing intensity, something unexpected happens. I was able to couple just one direction in the resonator but not both (cf. Fig. 3.13). The input power and frequency were symmetric in both directions but the resulting light circulation was not. That was the first observation of spontaneous symmetry breaking between counter-propagating light in microresonators.

The reason why this happens is that the light circulating in the two counter-propagating directions interacts with each other via the Kerr effect, in particular light travelling in each direction experiences a change in refractive index due to its

own SPM but also twice as large as a change in n from the other direction because of cross phase modulation (XPM) [6, 37, 38]. Light circulating in each direction attempts to push away the resonance for light circulating in the other direction, resulting in light only being able to circulate in one direction in the resonator at high power. This effect was theorised at the beginning of the 1980s by Kaplan and Meystre [39, 40, 41], however, it was never observed before because it was not possible to reach the necessary continuous wave intensities. This discovery was completely tangential to the original project but it led to a series of insights that I will elaborate upon in the following chapters.

Was the original idea of generating counter-propagating frequency combs in single microresonator even possible? It was indeed and it has been demonstrated one year later by the Kerry Vahala group [42] and it is currently used [43, 44]. The reason why they do not observe a symmetry breaking is that they initiate one frequency comb at a time with a technique called power kicking [45]. With their procedure there is never a situation with high power continuous wave light counter-propagating in the cavity, instead they only have two counter-propagating light pulses that do not interact for most of the round trip apart for the moment when they overlap. This limited interaction between the two directions increases the threshold power for symmetry breaking.

1.5 Why?

Was it worth changing the research direction of the whole group to chase a theory developed in 1982? Kaplan and Meystre opened a research path with their paper [39] but at the time the technology was not ready to prove their theory experimentally, never mind the realization of commercial devices.

From the scientific point of view, spontaneous symmetry breaking is a fascinating phenomena widely studied for its interesting mathematical properties in many fields from particle physics with the Higgs mechanism [46] to ferromagnetism, superconductivity and superfluidity. It is the mechanism leading a symmetric system into a state that violates that symmetry. In my case a circular resonator pumped equally in both direction ends up coupling light just in one direction.

In particular, symmetry breaking in microresonators can be used in two different regimes that present almost opposite characteristics. At the onset of symmetry

breaking the system is very sensitive to any perturbation that creates differences between the circulating direction. The combination of the Kerr effect and the resonant nature of microresonators amplifies these perturbations and enables the realisation of different kind of sensors. As originally imagined by Kaplan and Meystre [40] the system can amplify the small resonance shifts caused by the Sagnac effect [47, 48], enabling the realisation of compact optical gyroscopes [49]. Also the system can be used to probe the refractive index in the vicinity of the resonator to make a refractive index or particle sensor [50].

The other regime is well into the symmetry broken region where the system shows almost opposite characteristics. Once the resonator is in a defined circulating state, being resonant with the input laser in one direction but not in the other, it tends to maintain the state despite the fluctuation of the inputs. Only large changes in the input can overcome this hysteresis and cause a fast response of the resonator. This regime results in non-reciprocal light propagation that can be used to realise all-optical isolators and circulators [51], while the hysteresis opens the way to optical memories, routing [52], and computing [53].

Non reciprocal propagation is one of the key components missing in photonics circuits. Hence, compared to the eighties, Demand for chip integrated non-reciprocal devices is growing: the photonic market is supposed to grow to over \$ 10^{12} within ten years [54] due to the shift from electronic to photonic technology for telecommunications and on chip interconnects, not to mention the increasing use of photonics for biological and medical applications. At the same time, the technology to realise these device is maturing, as proven also by the proof of principle devices shown in this thesis.

Personally I feel as a duty for a scientist to verify or add to the work of other scientists, not because a lack of confidence but to reinforce their research and prepare a solid basis for future work. Finding theoretical works on the effects that I was observing for the first time was very motivational. Also, most of the discoveries that turned out to be a breakthrough for humanity did not have that objective in mind at the beginning and I still wonder if I am now following one of these branches, well aware that for every breakthrough there are many dead ends.

The other reason why I wake up every morning to go to the lab is curiosity. It is the thrill of finally measuring the results I hoped from the experiment I designed and assembled in the last weeks, maybe months. And the even bigger thrill when

results are unexpected and lead into a completely different direction opening new challenges. That is what happened with this thesis!

1.6 Aim

This thesis aims to provide a theoretical basis for understanding the Kerr-effect-mediated interaction between counter-propagating light in microresonators and the consequent symmetry breaking between counter-propagating light states. Another aim is to demonstrate the validity of this theory and to show proofs of principle informing the possible applications through three main experiments.

1.7 Outline

The remainder of this thesis is structured as follows:

The objective of Chapter 2 is to introduce the common theoretical basis used in the rest of the thesis. The coupling between a microresonator and a waveguide is modelled in the linear regime. The theory is then adapted to the case of high-Q-factor resonators and described in terms of measurable parameters. The fabrication techniques for the two types of resonators used in this thesis and the coupling optical fibres are described and alternative choices are evaluated.

In Chapter 3, I introduce the Kerr nonlinearity in the model and study the effects, first from a theoretical point of view then experimentally. The mechanism leading to spontaneous symmetry breaking is described

In the following chapters I analyse the possible applications of the symmetry broken regime. Chapter 4 explains how the Kerr effect in microresonators can be used to realise non-reciprocal devices such as optical isolators or circulators. I analyse the requirements of an isolator and expand the coupling model from Chapter 2 to the case of coupling two waveguides simultaneously and discuss the optimisation of the coupling parameters for this application. Finally, I present the results of two experiments and discuss the results.

Chapter 5 analyses the switching between the two symmetry broken regimes. A dynamical model is developed from the Lugiato-Lefever equation and I describe the process to numerically solve the model. The design of the experimental setup is discussed with a particular focus on the light modulation technique. The experimental

results show a hysteretical behaviour and a dependence of the switching characteristics that are compared with the theoretical model. This chapter ends with a discussion on the possible application of the bistability to all-optical memories, switches, routers, and logic gates.

The conclusions presented in Chapter 6 summarise the thesis and briefly touch on other applications of the symmetry breaking and the outlook for this research.

Chapter 2

Microresonators

I am always amused by simplicity, in particular when complicated problems can be solved with a simple and elegant solution. At first glance, microresonators are simple tiny glass rings that make it possible to explore nonlinear optics thanks to their incredibly high optical intensities. But, like most of the uncomplicated solutions require effort and study to be implemented, there is a lot of effort and technology behind the realisation of a microresonator.

In this chapter, I introduce the theoretical basis for the rest of the thesis. I develop a model for the coupling between a microresonator and an optical fibre. I then specialise the theory for the case of high-Q microresonators and express it in a normalised form in term of experimentally measurable parameters. For now, the theory deals with the linear regime. The Kerr nonlinearity will be introduced in Chapter 3. Finally, I describe the fabrication methods for the microresonators used in this thesis.

2.1 Coupling of light into the microresonator

Light in optical fibres is guided through total internal refraction exactly in the same way it is trapped into the microresonator. In both cases, the optical mode has a component of evanescent field i.e. an electromagnetic field exponentially decaying over a distance of the order of the wavelength from the interface [55]. In the case of the microresonator, this field lies in the air around the resonator and can be used to couple light but also to probe the surrounding of the resonator [56, 57, 58, 59].

There are several techniques to create a phase matched evanescent field that can couple with the resonator. In this thesis, only fused silica resonators coupled with

tapered silica fibres are used.

In the case of an optical fibre, it is the interface between the core and the cladding that confines the light and the evanescent field is entirely contained in the cladding before the jacket area. For this reason, just removing the plastic coating of an optical fibre it is not sufficient for accessing the evanescent field. To access the light in the fibre it is possible to taper the fibre by heating it close to the melting point of glass and pulling it. This process stretches the core and cladding of the fibre and reduces the fibre diameter to the order of one micron until a single mode can travel through the taper but now the guiding interface is air-glass, making the evanescent field accessible (more on this topic appears in Section 2.10).

Alternatively, it is possible to polish the side of a fibre to remove the cladding until the mode area is accessed [60]. Another solution is to use angle cleaved fibres. This method is usually much resilient than tapered fibres, however, this allows the coupling of light just in one direction. It is still possible to use multiple cleaved fibres to couple light into and out of the resonator, but in this case the phase and coupling factor between different points have to be taken into account.

Fibres are not the only way of producing an evanescent field. Total internal reflection in a prism [61] also produces an evanescent field. Furthermore, it is possible to choose the prism material to match the resonator so that the wave-vectors are the same in both media which is critical to obtain phase matching (as described in [62, 63]) and a higher coupling.

Placing the fibre close to the resonator with a precision translation stage makes it possible to couple light in and out of the resonator. By close I mean that there should be significant overlap between the evanescent field of the taper and the part of the resonator mode that exists outside the interface between dielectric and air. Let us now model the coupling between the ring resonator and the tapered fibre as depicted in Fig. 2.1.

In developing the coupling model, I assume linear light propagation, meaning that all the coupling parameters and the phase acquired during one round trip are not affected by the light intensity. This allows us to consider just one direction of propagation at the time. Also, I assume that the resonator has a single optical mode and I do not consider the polarisation of light at the moment. This may seem counter-intuitive in a thesis about nonlinear interaction between light propagating in multiple directions, but the nonlinear effects will be later reintroduced as a change

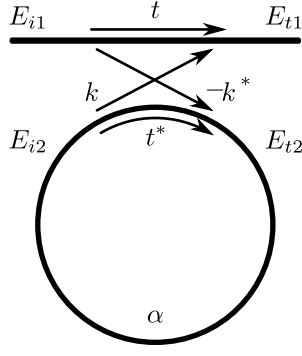


Figure 2.1: A schematic of the coupling region and the parameters used to describe the coupling of a resonator to a tapered fibre. t and k are the transmission and coupling respectively. α is the round trip transmission.

of the effective cavity length or, in other words, of the phase acquired per round trip in each direction. The input powers used in these experiments are low enough to neglect the Kerr effect in the optical fibres. Also, we consider the coupling point zero-dimensional and lossless (in case you are interested in when the coupling is not lossless I suggest [64, 65]). Despite being a wild approximation, it does not affect the validity of the model because of the phase matching between waveguide and resonator. Since the coupling is not adjusted during the experiment we can add any phase acquired at the coupling point to the length of the resonator and the fibre respectively.

The transmitted field through the fibre and the resonator can be described as follows. This model is well known for resonators and a general description of it can be found in [66]. However here I simplify it with the assumptions above and adapt it to the scope of this thesis.

$$E_{t1} = t \cdot E_{i1} + k \cdot E_{i2} \quad (2.1)$$

$$E_{t2} = -k^* \cdot E_{i1} + t^* \cdot E_{i2}, \quad (2.2)$$

where E is the electric field and the subscript i, t represent the input and transmission at the coupling point, while, in the context of this chapter, the subscripts 1, 2 indicate the tapered fibre and the resonator respectively. The coupling parameters t and k , and their complex conjugate t^* and k^* , are outlined in Fig. 2.1. For practical reasons E is normalised such that $|E|^2 = P$ the optical power of the mode (more on this choice in Section 2.3.1). This can be expressed also as a scattering matrix as

follows:

$$\begin{pmatrix} E_{t1} \\ E_{t2} \end{pmatrix} = \begin{pmatrix} t & k \\ -k^* & t^* \end{pmatrix} \begin{pmatrix} E_{i1} \\ E_{i2} \end{pmatrix} \quad (2.3)$$

The signs and complex conjugation make sure that under space inversion and time reversal the matrix still describes the correct phase delay acquired by light crossing the coupling region. In particular, the sign of k changes depending on light coupling in or out of the resonator, this is analogous to the phase shift that light experiences when scattered by an interface between two refractive index¹ and guarantee energy conservation at the coupling point. An eventual imaginary part of t and k represent a phase acquired by crossing the coupler. The fact that the resonator is closed on itself can be added with an additional equation:

$$E_{i2} = E_{t2} \cdot \alpha e^{i\theta} \quad (2.4)$$

where $(1 - \alpha)$ is the electric field loss in a round-trip and θ is the phase acquired by the field during the round trip that can be expressed as:

$$\theta = \frac{\omega L n}{c} = \frac{2\pi r \omega n}{c} = 4\pi^2 \frac{r}{\lambda} n, \quad (2.5)$$

by using the identity $\omega/c = k = 2\pi/\lambda$. Where ω is the angular frequency of the electric field, k is the wave vector, c is the speed of light, $L = 2\pi r$ is the circumference of the resonator, and λ is the wavelength of in vacuum. Note that the refractive index of the resonator n appears just here, we have to keep it in mind for Chapter 3, where I will introduce the Kerr nonlinearity and its effect on the refractive index.

Let me introduce some approximations. First let us assume that the coupling point is lossless which is equivalent of asking that the determinant of the scattering matrix is 1:

$$|t|^2 + |k|^2 = 1 \quad (2.6)$$

and also that I can normalise all the fields such that the only input field $E_{i1} = 1$.

The remaining fields have the following expressions

¹light refracted by a higher refractive index material is phase shifted by π while light refracted by a lower refractive index is not phase shifted. This arises from the Maxwell equations and particularly for the boundary conditions of the electric and magnetic fields.

$$E_{i1} = 1 \quad (2.7)$$

$$E_{t2} = \frac{-k^*}{1 - \alpha t^* e^{i\theta}} \quad (2.8)$$

$$E_{t1} = \frac{te^{-i\theta} - \alpha}{e^{-i\theta} - \alpha t^*} \quad (2.9)$$

$$E_{i2} = \frac{\alpha k^*}{\alpha t^* - e^{-i\theta}}. \quad (2.10)$$

We can now introduce the other assumption of a zero-dimensional coupling point. We can reasonably assume that there is no phase shift for light crossing from the resonator to the tapered fibre therefore we can assume $k \in \mathbb{R}$. Also, since the fibre and the resonator are made of the same material, any phase accumulated at the coupling point can be added to the round trip phase delay of the tapered fibre so also $t \in \mathbb{R}$. Now the fields are:

$$E_{i2} = 1 \quad (2.11)$$

$$E_{t2} = \frac{-k}{1 - \alpha t e^{i\theta}} \quad (2.12)$$

$$E_{t1} = \frac{te^{-i\theta} - \alpha}{e^{-i\theta} - \alpha t} \quad (2.13)$$

$$E_{i2} = \frac{\alpha k}{\alpha t - e^{-i\theta}}. \quad (2.14)$$

The corresponding powers are calculated as $P = E \cdot E^*$:

$$P_{i1} \equiv |E_{i1}|^2 = 1 \quad (2.15)$$

$$P_{t1} \equiv |E_{t1}|^2 = \frac{\alpha^2 + t^2 - 2\alpha t \cos(\theta)}{1 + \alpha^2 t^2 - 2\alpha t \cos(\theta)} \quad (2.16)$$

$$P_{i2} \equiv |E_{i2}|^2 = \frac{\alpha^2 (1 - t^2)}{1 + \alpha^2 t^2 - 2\alpha t \cos(\theta)} \quad (2.17)$$

$$P_{t2} \equiv |E_{t2}|^2 = \frac{(1 - t^2)}{1 + \alpha^2 t^2 - 2\alpha t \cos(\theta)}. \quad (2.18)$$

From now on let us just use the expressions for the power. It is worth evaluating these expressions in two special conditions. The first one is **resonance**, i.e. when the phase delay accumulated in one round trip is a multiple of a full cycle $\theta = m \cdot 2\pi$,

$$P_{t1} = \frac{(\alpha - t)^2}{(1 - \alpha t)^2} \quad (2.19)$$

$$P_{i2} = \frac{\alpha^2 (1 - t^2)}{(1 - \alpha t)^2} \quad (2.20)$$

$$P_{t2} = \frac{(1 - t^2)}{(1 - \alpha t)^2}. \quad (2.21)$$

The other condition is called **critical coupling** [67]. This happens when it is possible to completely cancel the transmission of the input fibre when in resonance. This condition is easily inferred from the equations above as $\alpha = t$. For critical coupling the fields have the following expressions:

$$P_{t1} = \frac{2\alpha^2 (1 - \cos(\theta))}{1 + \alpha^4 - 2\alpha^2 \cos(\theta)} \quad (2.22)$$

$$P_{i2} = \frac{\alpha^2 (1 - \alpha^2)}{1 + \alpha^4 - 2\alpha^2 \cos(\theta)} \quad (2.23)$$

$$P_{t2} = \frac{(1 - \alpha^2)}{1 + \alpha^4 - 2\alpha^2 \cos(\theta)}. \quad (2.24)$$

2.1.1 Low-loss (Lorentzian) approximation

In many works on resonators, the line-shape is assumed to be Lorentzian however the expressions in the previous section are not explicitly Lorentzian. It is worth investigating why, and under which conditions, a Lorentzian is a good approximation of this equation. This approximation for the resonance is generally taken because a polynomial form is more manageable than a trigonometric one. Furthermore, in most cases, we will be dealing with a single resonance and a single-peak decaying function is preferred to the trigonometric form that correctly shows periodical peaks every full rotation of θ , i.e. $\theta = 2\pi m$ with $m \in \mathbb{N}$. For small resonator losses $\alpha \sim 1$

it is possible to show that $P_{t1} = 1$ and $P_{i2} = 0$ unless also $\cos(\theta) \sim 1$.

To demonstrate this I expand the circulating power and the transmitted power substituting $\alpha^2 = 1 - \ell^2$ and expanding the Taylor series for $\ell \rightarrow 0$ up to the second order. For the sake of simplicity let us use the critical coupling condition.

Out of resonance

At first, I will assume that $(1 - \cos \theta)$ is finite (not close to 0). We will see later that this is the case of being out of resonance. The cavity power becomes

$$P_{i2} = \frac{(1 - \ell^2)\ell^2}{2(1 - \ell^2)(1 - \cos(\theta)) + \ell^4} \quad (2.25)$$

$$= \frac{\ell^2}{2(1 - \cos(\theta))} + O(\ell^4) \quad (2.26)$$

The approximation can be expressed as simply as

$$P_{i2} \sim 0 \quad (2.27)$$

Applying the same approximation to the power transmitted through the input fibre:

$$P_{t1} = \frac{2(1 - \ell^2)(1 - \cos(\theta))}{2(1 - \ell^2)(1 - \cos(\theta)) + \ell^4} \quad (2.28)$$

$$= \frac{(1 - \cos(\theta))}{(1 - \cos(\theta))} + O(\ell^4) \quad (2.29)$$

Again, the approximation can be expressed as

$$P_{t1} \sim 1 \quad (2.30)$$

Since all the input power is transmitted through the waveguide and none is coupled to the resonator the name of “out of resonance” is justified.

Close to resonance

One may be tempted to use this approximation even when the denominator is small but that is not how the Taylor expansion works. To analyse the second case let us start the Taylor expansion from scratch. The interesting case is when the laser

detuning from the resonance is small. In this case $\theta \sim 0$ so we can approximate the cosine at the second order:

$$\cos \theta = 1 - \theta^2/2, \quad (2.31)$$

getting:

$$P_{i1} = 1 \quad (2.32)$$

$$P_{t1} = \frac{\alpha^2 \theta^2}{(\alpha^2 - 1)^2 + \alpha^2 \theta^2} \quad (2.33)$$

$$P_{i2} = \frac{\alpha^2 (1 - \alpha^2)}{(\alpha^2 - 1)^2 + \alpha^2 \theta^2} \quad (2.34)$$

$$P_{t2} = \frac{1 - \alpha^2}{(\alpha^2 - 1)^2 + \alpha^2 \theta^2}. \quad (2.35)$$

These equations have now a Lorentzian form. Note how the assumption of small angle also removed all the resonances at a different free spectral range leaving just the peak at $\theta = 0$ (see Figure 2.2). Usually, this is not a problem since the only resonance contributing to the physics of the problem is the one closer to the laser line. In practice, the mode used is never the one corresponding to zero frequency, $m = 0 \rightarrow \theta = 0$ so we have to remember to bring back m in the equations when the absolute frequency is important instead of just the frequency difference. Note in Fig. 2.2 how the approximation holds even for a value of α significantly different from one.

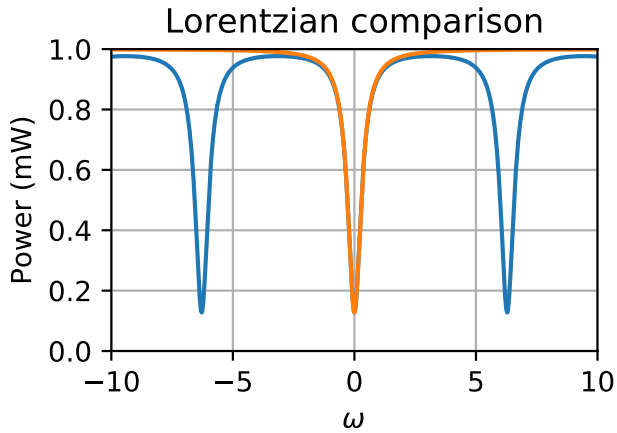


Figure 2.2: Comparison between the exact model and the Lorentzian approximation. In blue, the shape of a resonance without the small angle approximation, and in orange, the same resonance in small angle approximation. $\alpha = 0.8$, $t = 0.9$.

The algebra to get to the Lorentzian form is easier considering critical coupling but I hope that the reader is convinced that this would be the case also when $\alpha \neq t$.

$$P_{i1} = 1 \tag{2.36}$$

$$P_{t1} = \frac{(\alpha - t)^2 + \alpha t \theta^2}{(\alpha t - 1)^2 + \alpha t \theta^2} \tag{2.37}$$

$$P_{i2} = \frac{\alpha^2 (1 - t^2)}{(\alpha t - 1)^2 + \alpha t \theta^2} \tag{2.38}$$

$$P_{t2} = \frac{1 - t^2}{(\alpha t - 1)^2 + \alpha t \theta^2}. \tag{2.39}$$

To sum up, the resonance condition is given by $\theta = 0^2$ and the critical coupling condition is given by $\alpha = t$. Also, note how the intrinsic properties of the resonator are represented by α , the coupling parameters are t, k , and the laser characteristics are represented through its detuning from the frequency of interest θ .

So far the power of the laser is not taken into account because the model is linear. It will be introduced through its effect on the refractive index n thus in the variable θ .

2.1.2 Light loss channels (bending, absorption, scattering)

Before proceeding to the description of the theory in term of measurable parameters let us dwell on the reason why there are losses in the resonator. The relation between k, t and the coupling region is relatively straightforward: as the mode in the fibre and the resonator overlap, energy can be exchanged between the two. Also, because of energy conservation, if k increases, t has to decrease according to Eq. (2.6), so these two parameters are not describing losses but power transfer. The losses are represented in our model, by the fact that α differs from 1, and arise from different phenomena that I will now briefly analyse. In literature there are other quantities used to describe the losses. One of the most common is the quality factor of the resonator or Q-factor Q ; it is proportional to the ratio between the energy stored in the resonator and the energy lost each wave cycle. I will introduce a more practical

²Remember that we approximated the cosine function for small angles so only the case of $\theta = 0$ has to be considered insted of the usual the usual condition for resonance $\theta = 2m\pi$ with $m \in \mathbb{N}$.

definition in Section 2.2.5.

Bending losses

As we all know, light likes to travel in a straight line. It is possible however to confine light in waveguides that guide the light on curved paths. As the bend radius gets smaller, it is more and more difficult to steer the light and some of it escapes the waveguide and it is lost. Every ring resonator has to deal with this, being a closed structure. A better insight on why the light escapes the waveguide can be obtained by thinking that the light travelling at a larger radius needs to travel a longer distance to reach the same point of the bend. It is possible to transfer this difference in distance to a difference in refractive index [66], schematising a curved waveguide made of uniform dielectric as a straight waveguide with a gradient in the refractive index as shown in figure Fig. 2.3. The amount of losses depends on the

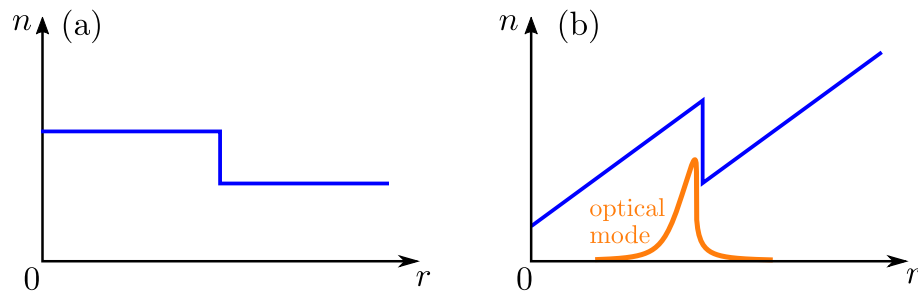


Figure 2.3: (a) Refractive index profile of a disk resonator, (b) Modelling the curvature of the resonator as a gradient in the refractive index. Adapted from [66].

radius of curvature and the refractive index step between the waveguide and the cladding. I observed that, for glass-to-air refractive index contrast, bending losses start to be a significant contributing factor to the losses for diameters below 40 μm . This transformation is also useful to understand why the light travels on the outer boundary of the ring and not in the middle. Given that the electric field in a mode tends to concentrate in the high refractive index area, in the right panel in Fig. 2.3, it is clear how a “potential well” is located at the outer edge of the circular structure.

Absorption

Another loss mechanism is absorption in the resonator. Fused silica is the material of choice for telecommunication fibres, not only for the availability and ease of manufacturing, but also for the low absorption in the C-band (1530 to 1565 nm).

If accounted alone, the losses due to absorption would limit the Q-factor at about 1.5×10^{11} at 1550 nm [68, 69]. Then why do the resonators presented in this thesis, and those in most of the literature, have lower Q? There are other sources of absorption. It is possible that the material constituting the rods is not pure fused silica but contains dopants or impurities. It is easy to notice when a batch of the silica rod used to machine microresonators is defective: the Q-factor of the resonators machined from that batch drops to 10^7 or below, despite all the fabrication process stays identical. Another source of losses is the adsorption of water moisture from air that create a layer of absorptive OH bonds on the surface of the glass. According to [68] this process happens at room temperature and reduces the Q by an order of magnitude in a few minutes after fabrication. Part of this adsorption may happen also during the fabrication process since machining the resonators in a laminar flow on N_2 improves the Q from about 4×10^8 to over 10^9 [58]. Absorption is the effect responsible for the heating of the resonator and the thermal effect described below in Section 2.4.

Scattering

The final source of losses worth mentioning is scattering. In this case, the light is not absorbed but is scattered out of the optical mode of interest. Light can leave the resonator or couple to different optical modes if they happen to have the same resonance frequency. Alternatively, light can couple to the same mode but in the opposite direction. This case is slightly different from the previous ones since it creates coupling between two identical modes, resulting in a doublet that becomes visible if the backscattering is strong enough [70].

There are various sources of scattering, and some of them also contribute to the absorption. Physical sources of scattering comprise impurities in the glass or dust deposited on the resonator. The latter can be prevented by ensuring that the resonator is handled in a dustproof environment and enclosing the setup in a dust-tight box as shown in Fig. 3.10. Scattering can arise also from the surface roughness of the resonator, this kind of scattering is low when the fabrication process involves melting the resonator surface because the surface tension is strong enough to level most of the roughness below the μm level, but could be significant when the material is etched or deposited.

The final source of scattering is related to the crystalline structure of the glass; despite using amorphous fused silica, the material still exhibits some periodic structure in the small scale. These kinds of scattering are called Raman scattering[71, 72, 73] when the optical phonon band is involved, or Brillouin scattering[74, 75] when the acoustic band is involved.

2.2 Measurable parameters

Let us continue with the mathematical description of a lossy resonator coupled to a waveguide. The model developed so far is very accurate despite its simplicity and can easily be modified to account for other effects. However, there is a major drawback: in the real world, it is almost impossible to measure directly the parameters involved in the model. Hence, to apply this model to the prediction of experimental results, it needs to be expressed in dimensionalised terms.

2.2.1 Linewidth

The linewidth is one of the most straightforward things to measure of a resonator. In the case of microresonators, it is enough to scan the laser frequency keeping the power constant and monitor the transmission through the taper. I can measure the half width half maximum linewidth (HWHM) just with the oscilloscope cursors; the only knowledge required is how much the frequency is changing per unit of time, i.e. the scan rate of the laser. This can be calibrated by adding an electro optic modulator (EOM) to the input to generate two sidebands at a known frequency difference from the laser frequency. The sidebands will cross the resonance at different times with respect to the main laser frequency and, from the time difference, it is possible to calibrate the scan speed in frequency difference over time.

The same HWHM can be calculated from the expression for powers from the theory. For convenience let's use P_{t2} . This is equivalent to defining the θ_{HWHM} such that $P_{t2}(\theta_{\text{HWHM}}) = P_{t2}(\theta = 0)/2$.

$$\theta_{\text{HWHM}} : P_{t2}(\theta_{\text{HWHM}}) = P_{t2}(\theta = 0)/2 \quad (2.40)$$

This results in

$$\theta_{\text{HWHM}} = \frac{1 - \alpha t}{\sqrt{\alpha t}} \quad (2.41)$$

We can also describe the intrinsic linewidth, i.e. the linewidth when there is no coupling with the tapered fibre as the limit for this quantity for $t \rightarrow 1$:

$$\theta_{\text{HWHM},0} = \frac{1 - \alpha}{\sqrt{\alpha}} \quad (2.42)$$

Similarly, under the condition for critical coupling $\alpha = t$ we get:

$$\theta_{\text{HWHM,crit}} = \frac{1 - \alpha^2}{\alpha} \quad (2.43)$$

To compare these values of θ_{HWHM} with the measurable linewidth in terms of angular frequency γ , we need to recall the relation between θ and ω .

$$\theta = m 2\pi r n \frac{\omega}{c} \quad (2.44)$$

In this case we are interested in small variations about the resonance, so we can use the small angle approximations and calculate the variation around $m = 0$

$$\gamma = \Delta\omega_{\text{HWHM}} = \frac{c}{2\pi r n} \theta_{\text{HWHM}} \quad (2.45)$$

Hence we can define all the relevant linewidths:

$$\boxed{\gamma = \left(\frac{c}{\pi d n}\right) \frac{1 - \alpha t}{\sqrt{\alpha t}} \quad \gamma_0 = \left(\frac{c}{\pi d n}\right) \frac{1 - \alpha}{\sqrt{\alpha}} \quad \gamma_{\text{crit}} = \left(\frac{c}{\pi d n}\right) \frac{1 - \alpha^2}{\alpha}} \quad (2.46)$$

Where d is the diameter of the resonator.

This model is supposed to deal with real life scenarios and the resonators suitable for the observation of nonlinear effects that are described in this thesis have a Q-factor of at least 10^7 . These Q-factors correspond to $\alpha \sim 1 - 10^{-4}$, as shown at the end of this section, hence we can safely approximate for $\alpha \rightarrow 1$. Under this assumption the linewidth for critical coupling is twice the intrinsic linewidth: $\alpha \rightarrow 1$, $\gamma_{\text{crit}} = 2\gamma_0$. This provides a method to measure the intrinsic linewidth of a resonator, by simply measuring the linewidth at critical coupling and halving it. If the coupling losses are much smaller than the losses in the resonator $\gamma \simeq \gamma_0$. Hence, an alternative way to determine the intrinsic linewidth is to measure the linewidth in the regime of very low coupling.

Since α and t play an identical role in the transmission through the ring resonator,

for consistency we can define accordingly a quantity κ that represents the coupling linewidth (or coupling strength):

$$\kappa = \left(\frac{c}{\pi dn} \right) \frac{1-t}{\sqrt{t}} \quad (2.47)$$

If the resonator is not strongly overcoupled we can assume the limit $\alpha, t \rightarrow 1$. This condition makes the various linewidths additive as in the case:

$$\gamma \simeq \gamma_0 + \kappa \quad (2.48)$$

Finally, the detuning between the laser and the resonance Δ as an angular frequency can be expressed in the small angle approximation as,

$$\Delta = \frac{c}{\pi dn} \theta \quad (2.49)$$

2.2.2 Coupling efficiency

The parameters regarding the width of the resonance having been dealt with, let us now focus on the ones describing the intensities. The coupling efficiency η represents how efficiently the power is transferred from the fibre to the resonator, it is defined as the fraction of pump power that is subtracted from the input field at resonance. We choose the resonance condition because this parameter represents the efficiency arising from the optical coupling, independently from the frequency mismatch between laser and resonator.

$$\eta \equiv \left. \frac{P_{i1} - P_{t1}}{P_{i1}} \right|_{\theta=0} \quad (2.50)$$

Using Eqs. (2.36) and (2.37) we find that:

$$\boxed{\eta = \frac{(1 - \alpha^2)(1 - t^2)}{(1 - \alpha t)}} \quad (2.51)$$

It is possible to demonstrate that in the limit of $\alpha, t \rightarrow 1$ this expression is equivalent to the expression of the coupling efficiency in terms of the other representation:

$$\boxed{\eta = \frac{4\kappa\gamma_0}{(\kappa + \gamma_0)^2}} \quad (2.52)$$

This can be demonstrated by writing Equation (2.51) and substituting Equations (2.46) and (2.47) and using the approximation $\alpha, t \rightarrow 1$:

$$\begin{aligned}\eta &= \frac{1 - \alpha^2}{\alpha} \frac{1 - t^2}{t} \frac{\alpha t}{(1 - \alpha t)^2} \\ &\simeq 2 \frac{1 - \alpha}{\sqrt{\alpha}} 2 \frac{1 - t}{\sqrt{t}} \frac{1}{\gamma^2} \\ &\simeq \frac{4\kappa\gamma_0}{(\kappa + \gamma_0)^2}\end{aligned}\tag{2.53}$$

2.2.3 Free spectral range

To define the free spectral range (FSR) we can refer back to our resonator model. To be in resonance, The light have to fit an integer number of wavelength in the circumference of the resonator so that it will interfere constructively every round trip. This corresponds to set the phase acquired in a round trip θ as a integer multiple of 2π :

$$\theta_{\text{res}} = 2\pi m \quad m \in \mathbb{N},\tag{2.54}$$

There is a series of equally spaced values of θ that correspond to a resonance. The FSR is defined as the difference between the resonance corresponding to the mode number m and the next one. So in the units of the acquired phase, the FSR is simply

$$\boxed{\Delta\theta_{\text{FSR}} = 2\pi.}\tag{2.55}$$

We can straightforwardly convert to angular frequency ω by using Eq. (2.5) since the two are proportional to each other.

$$\boxed{\Delta\omega_{\text{FSR}} = 2\pi \frac{c}{\pi d n}.}\tag{2.56}$$

We are not considering dispersion so $n(\omega) = \text{constant}$. Thus, for any geometrical mode, the possible resonant frequencies form an equally spaced set in the frequency domain.

If we are interested in the FSR in terms of wavelength we have to remember that there is a nonlinear relation between the two:

$$\omega = \frac{2\pi n c}{\lambda}\tag{2.57}$$

We can convert to wavelength FSR by considering the relative increment between a mode and the next to be equal in both cases.

$$\frac{\Delta\omega}{\omega} = \frac{\Delta\lambda}{\lambda} \rightarrow \Delta\lambda = \Delta\omega \frac{\lambda^2}{2\pi n c} \quad (2.58)$$

Hence:

$$\boxed{\Delta\lambda_{\text{FSR}} = \frac{\lambda^2}{Ln}} \quad (2.59)$$

The equally spaced lines in frequency do not correspond to equally spaced lines in the wavelength domain. Note than n is made explicit in the equations, hence the vacuum wavelength is the one that matters.

2.2.4 Finesse

The finesse of a resonator is defined as the ratio between the free spectral range and the linewidth, which can be easily calculated from Eqs. (2.41) and (2.55) as

$$\mathcal{F} = \frac{\Delta\theta_{\text{FSR}}}{2\Delta\theta_{\text{HWHM}}} = \pi \frac{\sqrt{\alpha t}}{(1 - \alpha t)} \quad (2.60)$$

For low losses the finesse can be approximated as 2π over the round trip power losses which can be used in all of the practical cases in this thesis. So the coupled finesse and the intrinsic finesse are:

$$\boxed{\mathcal{F} \simeq \frac{2\pi}{1 - \alpha^2 t^2}, \quad \mathcal{F}_0 \simeq \frac{2\pi}{1 - \alpha^2}} \quad (2.61)$$

Finally, the finesse can be defined in terms of measurable parameters by using the results for the FSR found above and the linewidth:

$$\boxed{\mathcal{F} = \frac{2\pi \left(\frac{c}{n\pi d}\right)}{2\gamma} = \frac{c}{\gamma n d}} \quad (2.62)$$

Note how the finesse of the cavity does not depend on the wavelength of the laser.

2.2.5 Q-factor

The quality factor or Q-factor Q of a resonant cavity is defined as 2π the stored energy in the cavity at a certain resonance frequency ν over the losses in one wave

cycle, in analogy to the electronic equivalent of a resonating circuit.

$$Q = 2\pi \frac{E_{\text{stored}}}{P_{\text{loss}}/\nu} \equiv 2\pi\nu\tau \quad (2.63)$$

This definition is not very agile in the case of microresonators; however when Q is greater than unity, it is possible to define it in the easily measurable form: the ratio between the operating frequency ω and the linewidth of the resonance $\Delta\omega_{\text{FWHM}}$,

$$Q = \frac{\omega}{\Delta\omega_{\text{FWHM}}} = \mathcal{F} \cdot \frac{\omega}{\Delta\omega_{\text{FSR}}} \quad (2.64)$$

Or, using the measurable quantities above:

$$\boxed{Q = \frac{\omega}{2\gamma}} \quad (2.65)$$

It is very important to remember that with the small angle approximation we fixed the angle $\theta \sim 0$. This means that we are effectively using the variables θ, Δ as detunings from a resonance. We must, therefore, be careful when introducing back the absolute resonance frequency ω .

$$\boxed{Q = 2\pi m \frac{\sqrt{\alpha t}}{2(1 - \alpha t)} = \left(\frac{\pi d n}{c}\right) \omega \frac{\sqrt{\alpha t}}{2(1 - \alpha t)}} \quad (2.66)$$

The mode order m cannot be measured, however it can be estimated as the closest integer multiple of the vacuum wavelength to the effective cavity length:

$$m = \frac{L}{\lambda} = \frac{\pi d n}{\lambda} \quad (2.67)$$

Note that, since the Q-factor depends on γ , the same property between the intrinsic Q-factor and the critical coupling can be drawn:

$$Q_0 = 2Q_{\text{crit}} \quad (2.68)$$

2.3 Normalised theory

So far we developed a dimensionless version of the theory of coupling to a resonator. This is useful since it provides a simple approach to the maths and it is more digestible by software. However, when comparing the simulation results to

experiments, we need to relate the theory to measurable quantities. We did that in the previous section but we lost some of the agility we had in the initial model. To satisfy both conditions it would be ideal to express the equation with their dimensions but normalise them with characteristic units so that the mathematical treatment and the programming remain agile. That is exactly what I am going to do in this section. Also, we are aiming to keep the theory independent from the coupling characteristics and the resonator characteristics so that one model suits all the implementations. Finally, it would be nice to keep the expressions as short and compact as possible.

2.3.1 Electric field, power and intensity

In the derivation of the equation so far I assumed the power being the

$$P = |E|^2 \quad \text{and} \quad P = I \cdot A_{\text{eff}} \quad (2.69)$$

These two equations are important since the photodiodes used in the experiment measure the power P and, as described later, the Kerr effect depends on the intensity I of the field. This proportionality factor in Eq. (2.69) simplifies the theory developed so far but results in uncommon units for the electric field; however, for this application, the electric field is never measured and the only important characteristic is just the proportionality between the intensity I and power P ; and the modulus square of the field $|E|^2$.

For the sake of completeness however let us remember than the Poynting vector is defined as [76]:

$$\vec{S} = \vec{E} \times \vec{H} \quad (2.70)$$

This leads to an intensity for a wave propagating in a medium of

$$I = \frac{v_{\text{phase}} \epsilon_0 \epsilon_r \mu_r}{2} |E|^2. \quad (2.71)$$

In this thesis the meaning of intensity is the one used in general physics: the optical energy flowing per unit of time and unit of area, and measure it in SI units of $[\text{W}/\text{m}^2]$. In both cases the power is related to the intensity through the effective mode area A_{eff}

2.3.2 Characteristic frequency

Let us recall the ring resonator mode in the lorentzian approximation described by Eqs. (2.36) to (2.39) and express it in terms of measurable parameters. Let us start with the circulating power Eq. (2.39) and express the powers with a more meaningful notation of circulating power $P_{t2} \rightarrow P_{\text{circ}}$ and input power $P_{i1} \rightarrow P_{\text{in}}$:

$$P_{\text{circ}} = \frac{P_{\text{in}}(1 - t^2)}{(1 - \alpha t)^2 + \alpha t \theta^2} \quad (2.72)$$

Initially we will focus on expressing the frequency. A natural way of expressing the detuning is to use the angular frequency difference between the laser and the cavity resonance Δ . Since θ is dimensionless we have to divide this by another angular frequency. There are several linewidths in the previous section to pick from, but since I would like to have all the coupling characteristic included in the normalisation and not explicitly appearing in the equations, I will use the coupled linewidth γ . Let us recall their expressions.

$$\Delta = \frac{c}{\pi dn} \theta \quad \gamma = \left(\frac{c}{\pi dn} \right) \frac{1 - \alpha t}{\sqrt{\alpha t}} \quad (2.73)$$

and substitute them into Eq. (2.72).

$$P_{\text{circ}} = \frac{P_{\text{in}}(1 - t^2)}{(1 - \alpha t)^2 \left(1 + \left(\frac{\Delta}{\gamma} \right)^2 \right)} \quad (2.74)$$

There are still a few α and t left but the frequency component of the equation is now normalised. We now know that we can use a dimensionless detuning in the theory and convert it to real values by expressing it in units of the HWHM linewidth of the resonator.

2.3.3 Coupled Power

The remaining factors have to be adsorbed in the definitions of power. First, we have to consider that the circulating power depends on the coupling of the resonator as flagged by the presence of t in the equation. By substituting Eq. (2.51) for the coupling efficiency,

$$\eta = \frac{(1 - \alpha^2)(1 - t^2)}{(1 - \alpha t)} \quad (2.75)$$

we can absorb this dependence in a measurable ratio of powers

$$P_{\text{circ}} = \frac{\eta P_{\text{in}}}{1 + \left(\frac{\Delta}{\gamma}\right)^2} \frac{1}{(1 - \alpha^2)} \quad (2.76)$$

In high-Q microresonators, the intracavity power is orders of magnitude higher than the power propagating in the fibre; also there is now way to access that power directly but only via external means such as the transmission of the tapered fibre. To keep the intracavity power and the input power at the same order of magnitude we can divide by the enhancement factor of the cavity. Since the detuning and the coupling efficiency are already expressed in the equations, we define the power enhancement \mathcal{E} as the ratio between the input power (cf. Eq. (2.32)) and the circulating power (cf. Eq. (2.35)) under both the resonance condition $\theta = 0$ and the critical coupling ($\alpha = t$) condition:

$$\mathcal{E} = \frac{P_{t2}}{P_{i1}} = \frac{1 - \alpha^2}{\frac{(1 - \alpha^2)^2}{1}} = \frac{1}{1 - \alpha^2} = \frac{\mathcal{F}}{2\pi} \quad (2.77)$$

Where in the last equality I used Eq. (2.61). We can now substitute this in Eq. (2.76) and obtain

$$\frac{2\pi}{\mathcal{F}_0} P_{\text{circ}} = \frac{\eta P_{\text{in}}}{1 + \left(\frac{\Delta}{\gamma}\right)^2} \quad (2.78)$$

Allow me to define the left side of the equation as coupled power. The reason why this quantity deserves a name is that it is easy to measure. Energy conservation tells us that this is just the power missing from the transmission that went into the resonator:

$$P_{\text{coup}} = P_{t,1} - P_{i,1}. \quad (2.79)$$

It can be measured by monitoring the input power and the transmission of the taper with photodiodes. Also, measuring the coupled power at resonance gives a direct measurements of the coupling efficiency as the ration between coupled power and

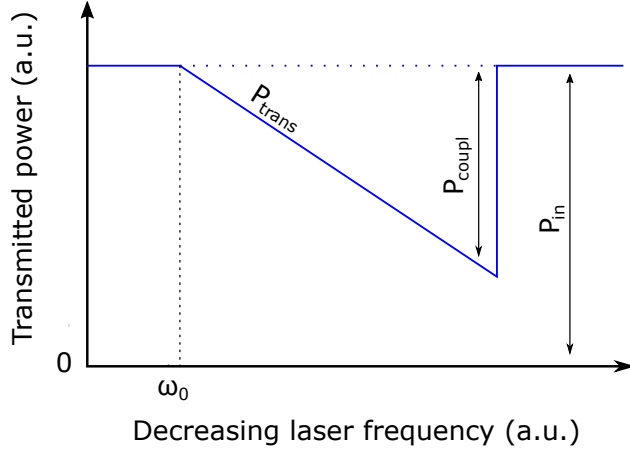


Figure 2.4: *Definition of the coupled power. In blue, a schematized transmission spectrum of a microresonator resonance when scanning the laser towards lower frequency. The cold resonance is at ω_0 but it is deformed by the thermal and Kerr effect. The input power P_{in} is equal to the transmitted power P_{trans} outside the resonance. The coupled power P_{coup} is measured as the power missing from the out of resonance transmission.*

input power in resonance:

$$\eta = \left. \frac{P_{\text{coup}}}{P_{\text{in},1}} \right|_{\theta=0} \quad (2.80)$$

Note that in Fig. 2.4 the condition of $\theta = 0$ happens right before jumping out of resonance and not at ω_0 .

So far, there is no need for a normalisation power because the system is linear. In other words the circulating power is always proportional to the input power as can be seen in Eq. (2.78). Hence no natural unit of power emerges from the equations. In the next chapter we will introduce the Kerr effect as a power dependent detuning hence we will need a normalisation power.

2.4 Thermal effects

I just mentioned that the thermal effect deform the resonance, let us analyse how. When the light couples into the resonator, a part of it is absorbed by the glass and impurities, resulting in a temperature increase. The temperature change is typically slower than the energy build-up time of the cavity and characterised by different time constants due to the different heat capacity and conductivity of the setup. At the shortest timescale, there is the mode volume of the resonator that is responding at the μs timescale. The whole rod resonator takes longer to respond, in the order of the second timescale. Finally, heat is transmitted to the holding pillar and to the

air in the enclosed box around the resonator with a thermalisation time of a few minutes.

2.4.1 Thermoelasticity and thermorefractivity

Temperature affects the resonance frequency in two ways: thermoelastic and thermorefractive effects [77, 78]. A consequence of the change in temperature is the thermal expansion of the glass also known as thermoelastic effect. This increases the diameter of the resonator and hence reduce the resonance frequency.

$$\omega_{\text{res}} = m \frac{c}{nr} \quad (2.81)$$

A less known effect is thermorefractivity, which is a change in the refractive index of the resonator with the temperature. The material used in this thesis (SiO_2) has both the thermal contributions and the Kerr effect pointing in the same direction: and increase in power or temperature reduce the resonance frequency. However, some materials show a reduction of refractive index with increasing temperature, this opposite sign and the different timescale between the Kerr and thermal effects can lead to instability and oscillations [79]. A popular material in the field of microresonators that shows this behaviour is CaF_2 .

To have an idea of the effect, a fused silica resonator with radius $r = 0.5$ mm operating in the C-band has a mode number $m \simeq 2000$. The coefficients for fused silica are: $\alpha_l = 5.5 \times 10^{-7} \text{ K}^{-1}$ for the thermoelastic and $\alpha_n = 1.0 \times 10^{-5} \text{ K}^{-1}$ for the thermorefractive. Hence, a change of temperature of 1°C correspond to a relative change in frequency of

$$\frac{\Delta\nu}{\nu} = \alpha_l \Delta T + \alpha_n \Delta T = 1.055 \times 10^{-5} \quad (2.82)$$

this may not seem much, but microresonators have very high Q-factors, of the order of 2×10^8 corresponding to a linewidth of 2 MHz. The shift above corresponds to a shift over 2 GHz: 1000 times the linewidth!

2.4.2 Passive thermal locking

Thermal effects are often much more significant than the Kerr effect in terms of amplitude, but the effect on the locking works in the same direction, shifting the

resonance to lower frequencies as the coupled power, hence the temperature increases. It is possible to lock to a resonance only on the blue detuned side and this is the situation where the microresonators are typically operated.

It is important to note that, when the resonator is used to produce a frequency comb, the spatial distribution of light is not the same in every part of the resonator. Indeed, a frequency comb is typically constituted by a soliton [31] i.e. a pulse of light circulating into the cavity, thus the interplay between the global thermal effects and the local Kerr effect complicates, however, several active locking techniques have been developed to bring the resonator in the soliton state and keep it there indefinitely [45, 80]. In this thesis, I assume that the circulating light has a continuous wave profile (more on this in Chapter 5).

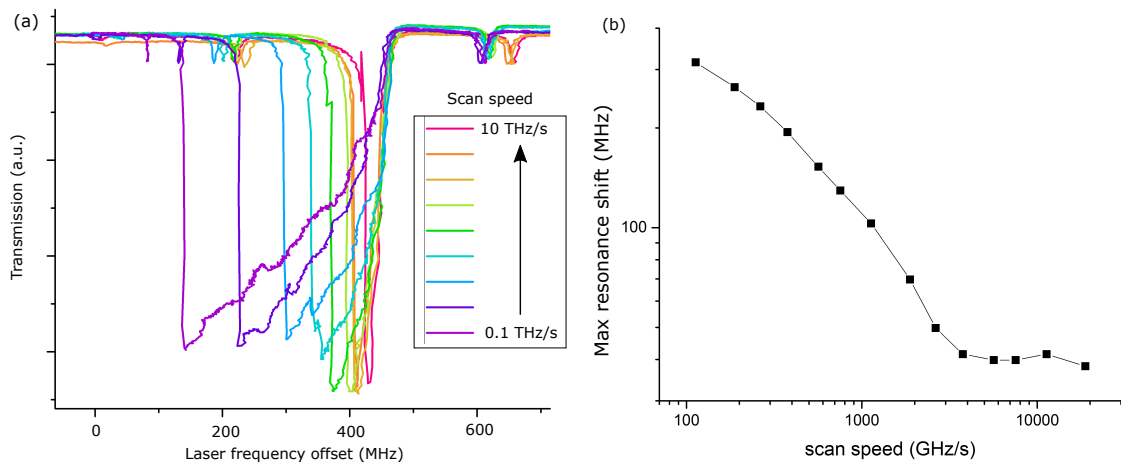


Figure 2.5: *Thermal effects. (a) the transmitted power through the taper as a function of the laser frequency of a high-Q resonance. The different traces have been acquired at different scanning speed and aligned at the cold cavity resonance. (b) the thermal triangle amplitude, measured as the difference between the resonance and the point of jumping out, as a function of the laser scan speed.*

To evaluate the capture range of the thermal locking, it is possible to measure the tilt of the Lorentzian and its extension in frequency at different laser scanning speeds Fig. 2.5³ (this topic is discussed later in Section 3.1 in the context of the Kerr effect). A theoretical model can be built by measuring or fitting the thermal capacity and conductivity of the various parts of the resonator [81] however the relevant information for this thesis are the lock range and the speed. To measure it the resonator is pumped in a single direction while scanning the laser frequency at different speeds. The tilted resonance width is measured for each different speed.

³These graphs originate from preliminary measurement. They are intended as a qualitative demonstration of the thermal effect in microresonators more than as a quantitative measurement.

Despite the low Q-factor (2×10^7) of the resonator compared to the other ones used in this thesis and the relatively low power of 30 mW, the resonance extends over 100 MHz for scanning speeds up to 1000 GHz/s. In higher Q-resonators, this can stretch up to a few GHz locking range. The response and locking range is even faster in smaller structures with less thermal inertia such as microtoroids and microdisks described in Section 2.6. It is important to point out that there are techniques to cancel the thermal effects either by engineering the resonator material [82, 83] or by using an auxiliary laser in order to stabilise the total circulating power [23].

2.4.3 Neglecting the thermal effect

In the rest of the thesis, I will neglect the thermal effect by including it in the laser detuning. This is valid because the thermal effect depends only on the total power in the resonator but not on the direction of propagation. If the laser scan is slow enough the resonator can be assumed to be in a thermalised steady state, hence the thermal effect would just result in the detuning Δ being proportional to the laser frequency offset.

This assumption however is not perfect and introduces a few problems. First, there are multiple time constants for the thermal relaxation of the resonator, so the magnitude of the thermal effect will depend on the scanning speed, the input power, the coupling to the resonator, and the thermal characteristics of the resonator itself. The attempts at fitting the proportionality constant between Δ and the laser frequency are accompanied by a huge error hence most of the plots where the laser is scanned just use the laser frequency as the axis. Also, as shown in the following Chapter, when the bubble splits at high power, the total power in the resonator change. This will cause a change of the proportionality constant between Δ and the laser frequency changes, deforming the profile of the curves in comparison to the theory. Eventually, for even higher input power, the sudden change in circulating power makes the thermal locking fail, so in these cases additional active locking systems are needed. It is important to conclude by saying that the thermal effect does not contribute to effect under study, i.e. to the resonance frequency splitting. Thermal effects do not mask the Kerr effect, despite contributing to the resonance frequency shift at least 100 times more.

2.5 Why Microresonators?

Before discussing the fabrication techniques, let us elaborate on the reasons behind the use of microresonators briefly introduced in Chapter 1. From a physical point of view, it is important to have a closed loop waveguide to achieve interference between subsequent round trips and consequently resonance. The structure cannot be a linear cavity, such as Fabry-Perot interferometers because for the physics analysed in this thesis, we need to differentiate between the two propagation directions clockwise (CW) and counter-clockwise (CCW). This is not possible in a high-Q-factor Fabry-Perot cavity because the field inside is a stationary wave, no matter if the light input comes from one end or the other. It is still possible to identify other effects such as polarisation.

Fibre loop structures, instead, support travelling waves where it is possible to differentiate the propagation direction even if the two directions are degenerate in the resonator, i.e. they show the same resonance frequency (polarisation effects can be observed on top of this [84, 85]) it is still possible to observe them independently just by detecting the power leaving the resonator in each direction. However, to obtain sufficient intensity in a fibre loop, synchronous pulsed pumping is required given the large mode volume.

In the case of whispering gallery mode resonators, the different circulation directions are still degenerate but opposite polarisation modes are resolved because they see different confinement at the surface interface of the bends. Therefore, they show different resonant frequencies because their effective path length is different. In other words, the resonator acts as a polariser at a specific frequency.

2.5.1 The quest for high-intensity

So why did I choose the title “microresonator” instead of “ring resonator”? The reason is that this work focuses on nonlinear phenomena that depend on the light intensity. In general, the intensity of a propagating electromagnetic field can be described as the ratio between the propagating power and the cross-sectional area:

$$I = \frac{P}{A_{\text{eff}}} \quad (2.83)$$

Specifically, the effects I investigate are related to $\chi^{(3)}$ that is a third order nonlinearity. Hence one can expect that really high intensities are needed to observe its effect and that is indeed true. To achieve the highest intensity possible, I have to optimise all the parameters in Eq. (2.83).

Increasing the launched power in the resonator is, of course, the first obvious and, if you allow me, inelegant way of increasing the intensity. Let us try to figure out some indicative values. Usually, narrow linewidth diode lasers can emit less than 100 mW, with some sacrifice on linewidth and stability they can go up to a few hundreds of mW. It is possible to amplify these laser sources without significantly affecting the linewidth and stability characteristics. In our lab, we have erbium doped fibre amplifiers (EDFA) up to 5 W output power; unfortunately, most of the commonly used optical components are rated up to 100 mW even if they handle 300 mW with no problem and often survive long enough for a couple of measurements at 500 mW but that is the limit⁴.

The connections between fibre and fibre are another weak point of the setup. These are the point in the optical setup more vulnerable to power damage since light is still confined in a cross-sectional area of the size of the fibre mode but it goes through several interfaces that may have damages, scratches or dirt. Any of these defects may cause absorption of light and consequently the release of heat in a very confined region that may melt the glass locally and increase the effect of the defect. The resulting chain effect may just ruin the connectors, weld them together, or, in the worst case, start a burning point that travels along the fibre and stops at the nearest expensive piece of equipment⁵. In the first two cases, it is usually possible to recover the connector by polishing it with increasingly fine lapping paper until a flat and shiny surface is recovered. One of the possible solutions to avoid this is to splice the components of the optical setup together instead of connecting them. Splicing consists in aligning the cleaved ends of two fibres and melting the contact point with an electric arc in order to weld them together and create a single fibre. Splicing produces almost lossless connections that are not subject to absorption, hence are more reliable at high power. The drawback is that the only way to disconnect two components is to cut the optical fibre limiting the re-usability of the components itself and the flexibility of the setup for quick adjustments and

⁴Don't ask me how I know this.

⁵Don't ask me how I know this!

tests.

A huge contribution to the quest for power comes from the use of resonant structures. This allows recycling (hence increasing) the power launched in the resonator up to a million times depending on the finesse of the resonator. Also, this power recycling does not create power-related damage because the absorption in the resonator is very low. In the case of this thesis, there is another benefit in having high finesse and consequently high Q-factor. When measuring resonance frequency differences or shifts, the smaller the linewidth of the resonance the easier it is to detect these shifts as a change in circulating power.

Finally, to increase the intensity one would like to concentrate the light in the smallest mode area. The word “micro” in microresonator refers to the mode cross-sectional diameter, which is of the order of a few microns in size. Again the limitation comes from the physics: light of a certain wavelength cannot generally be confined in a dimension much shorter than its wavelength unless using plasmonic effects or photonic crystals. As an example, the most common single mode fibre confine light with a wavelength of $1.55\ \mu\text{m}$ with a core diameter of $8.2\ \mu\text{m}$. In this case, the actual mode is extending outside the core with a mode field diameter⁶ of $10.4\ \mu\text{m}$. This is due to the relatively small refractive index contrast between the core ($n \simeq 1.442$) and the cladding ($n \simeq 1.440$). Guiding the light with a stronger refractive index contrast allows it to be confined even more. Examples of this are rod resonators, where the refractive index contrast is the one between air and the rod material, or waveguide resonators where the low refractive index material can be air or cladding made of different materials. The effective cross-sectional area varies with the platforms. In rod resonators I calculate with Comsol Multiphysics A_{eff} in the range between $400\ \mu\text{m}^2$ and $10\ 000\ \mu\text{m}^2$ depending on the geometry of the resonator. In microtoroids the area is of the order of $50\ \mu\text{m}^2$ and in microdisks can be as low as $10\ \mu\text{m}^2$. In waveguide resonators the mode area mostly corresponds with the area of the waveguide, generally of the order of $1\ \mu\text{m}^2$.

In the following section I analyse some of the most common platforms used to realise microresonators.

⁶Data provided in the Corning Inc. datasheet for their SMF-28 Ultra Optical Fiber

2.6 Platforms and microfabrication

In this section, I will describe the two most used platforms in our research group. The platform used in the experiments presented in this thesis are SiO_2 microrod resonators but I contributed significantly to develop the process to fabricate SiO_2 microdisks and microtoroids in the cleanroom.

All the techniques mentioned below use refractive index contrast to confine the light in a circular path. This phenomenon can be described in the simple picture of ray optics by using the Snell law for refraction:

$$\frac{n_A}{n_B} \sin \theta_A = \sin \theta_B \quad (2.84)$$

where A, B are the dielectric materials on either side of an interface and θ_A, θ_B are the incidence angles to the normal vector. If the light is propagating towards the interface between a higher refractive index material (A) and a lower one (B) at an angle that is very oblique the left side of the equation may be greater than 1, hence there is no possible refraction angle and the light is all reflected. This angle is defined as critical angle:

$$\theta_{\text{crit}} = \arcsin \frac{n_A}{n_B} \quad (2.85)$$

and the phenomena is called total internal reflection. This is can be commonly experienced in a swimming pool from underwater when, looking directly upwards, is possible to see the ceiling; while looking sideways, the water surface reflects the pool floor. If a tropical sea is available the reflected objects could be even more amazing than a tiled floor (see Fig. 2.6).



Figure 2.6: *A sea turtle skimming the sea surface and, above, the total internal reflection from the water-to air interface.*

2.6.1 Modes inside the resonator

The mental picture of a ray of light bouncing inside a circle is misleading because it transmits the idea that all the light is entirely confined in the ring and that it gets closer and away from the surface at different points.

In the case of microresonators, the dimensions of the devices are not much larger than the wavelength of light used therefore it is more appropriate to describe the effect by solving the Maxwell equations at the interface [86]. The result of such calculations, performed with COMSOL multiphysics reveal that the guided optical modes are confined close to the surface of the optical ring resonator. Some of the solutions are shown in Fig. 2.7 where the fundamental mode has the shape of a circle “squished” on the outside edge of the glass by “centrifugal force”. The higher order

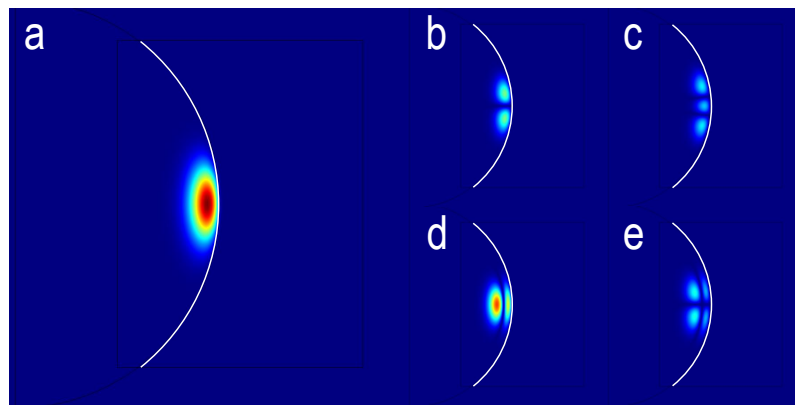


Figure 2.7: *Intensity of the optical modes inside a round resonator calculated with COMSOL Multiphysics. Pictures show a radial section of a resonator with 1 mm rod diameter and 50 μm radius of curvature at a wavelength of 1550 nm. Panel (a) shows the fundamental mode, the four panels (b-e) show some of the higher order modes.*

modes present multiple lobes both vertically and in the depth direction. There is always a zero of intensity between the lobes and the direction of the electric field is swapped between each lobe and the neighbouring ones. Experimentally, it is possible to identify the vertical order of a mode by moving the tapered fibre up and down and counting the number of maxima and zeros of the coupling as the fibre passes across each lobe. There is no simple way of identifying the depth order of the mode. However, some modes show high coupling even with a thick tapered fibre or the fibre kept away from the resonator: these are likely to be zero order in the depth direction. Lower order modes are not always to be preferred since their stronger evanescent field they interact more with the surface where most of the absorbing and scattering imperfections are, hence they may show lower Q-factor than higher

orders modes. The ideal situation is a mode with enough evanescent field to achieve critical coupling but not too much to spoil the Q-factor.

2.7 Glass rods

The experiments described in Chapters 3, 4 and 5 of this thesis are all based on glass rod resonators [87]. These resonators consist of a bulging ring around the side of a cylindrical bar of dielectric material as depicted in Fig. 2.8. The cylinder itself is enough to confine light in the radial direction but confinement is needed also in the axial direction, this confinement is provided by the convex shape of the resonator.

The fabrication of rod resonators is a subtractive manufacturing process, starting with a cylindrical rod of material that is turned to the desired shape. Instead of a mechanical tool, I use a laser to ablate the surface of the rod since this allows a fast machining of a very smooth surface since the same laser can both ablate or anneal the surface, depending on the power.

The choice of fused silica, or amorphous SiO_2 , as the resonator material is dictated also by its broad transparency spectrum, hence to machine the resonator, a laser emitting a frequency outside this broad spectrum is needed. Good absorption can be achieved in the vacuum ultraviolet (VUV) region (wavelength below 200 nm) but, as the name suggests, in that region the air absorption is relatively high so the machining should happen in vacuum. Also, there are no high power sources available at that wavelength, and VUV is an ionising radiation, which is not ideal from a health and safety point of view.

On the other hand, glass also has high absorption above 6 μm and high power CO_2 lasers emitting at 10 μm are relatively inexpensive. Also, most of the materials that are transparent in the visible spectrum, are opaque to the laser wavelength, allowing the building of an enclosure for the machining setup that allows the operator to see the ongoing process but keeps the setup eye-safe.

Our machining setup starts with a CO_2 laser emitting up to 100 W of optical power at the wavelength of 10.5 μm . The laser light is guided through a metal-enclosed, 2 m long path to allow the laser mode to expand to 10 mm in diameter and improve the M^2 of the beam. Along this path, a green alignment laser pointer is added coaxially to the CO_2 beam via a wavelength selective mirror. A pair of galvo mirrors steer the beam to trace the desired profile on the glass rod and a ZnSe

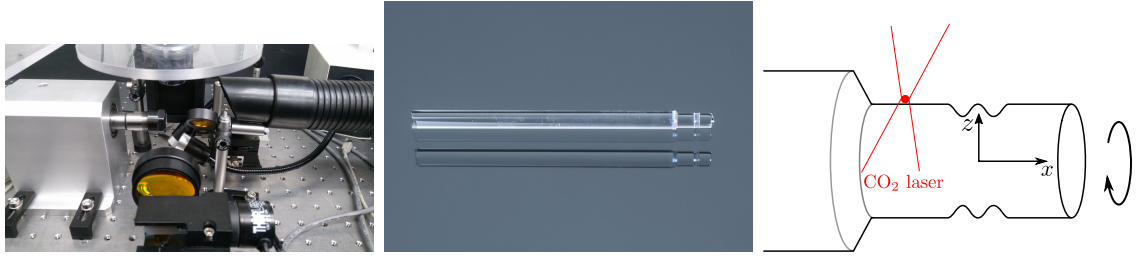


Figure 2.8: *Fabrication of glass rod microresonators. On the left, a photograph of the CO_2 machining setup. One of the galvo mirrors and the focusing lens are visible in the foreground, the spindle is on the left and the air extractor is on the right. On the background the beam-block is visible and part of the enclosure and imaging camera are on the top. Middle, a machined glass rod resonator. Right, a sketch clarifying the geometry of the system. The three panels have the same perspective.*

lens with a focal length of 10 cm focuses the beam on a spot size of about $20\ \mu\text{m}$. A microscope camera observes the resonator from the top to monitor the process and adjust the parameters.

The machining process is divided into two main steps. The first step prepares the surface of the rod to be machined. A glass cylinder with a diameter slightly larger than the desired final diameter is mounted in the spindle such that the end of the rod is about 2 mm after the focal spot of the laser with the galvo mirrors in the neutral position. The rod is then spun and the laser moves back and forth along the axial direction while slowly reducing the z component. This step is necessary because the spindle has some run-out both axial and radial, meaning that the axis of rotation of the spindle is not aligned and has a small offset with the axis of the chuck and the rod. Keep in mind that I am fabricating structures with an accuracy of the order of a micron, so a small run-out at that level is always present even in the best quality spindles. By removing some material from the rod before machining the resonator itself, the axis of the glass rod is realigned to the axis of rotation. This first part is the most time consuming because there is a limit to the speed at which the rod can be milled down. The goal during the whole machining is to keep the thermal stress to a minimum. Hence, the circumference where the laser is acting should be at an almost constant temperature, therefore a rotation speed of 2000 rpm or greater is required and the scanning in the x direction is limited to about $0.5\ \text{mm/s}$. Also depositing too much energy in a section of glass may crack it because of the thermal shock or the thermal expansion in different parts of the rod, but another subtle effect takes place. A change in the glass structure is observed

where too much power is applied, not just on the surface but even deeper in the rod. This last effect limits the machining speed in the z direction to 1 mm every 10 minutes, being even slower for larger resonators because the amount of material to be removed is proportional to the radius. As an indication, I found safe to remove up to $2 \text{ mm}^3/\text{min}$ but having a microscope camera looking at the machining section helps to adjust the parameters based on the brightness and the colour of the thermal radiation emitted by the hot glass in the laser spot.

To improve the Q-factor, it is critical to avoid stress in the glass close to the surface. Hence, the machining speed is slowed even more for the last $200 \mu\text{m}$ of reduction in the z direction and finally the laser is scanned on the x direction without changing the z value for a few minutes. During this last phase, the spot of the laser is likely outside of the surface and just the tail of the Gaussian beam is hitting the surface, melting it instead of ablating giving it time to cool slowly.

Once the surface is ready, it is time to move to the second step and machine the resonator itself. There are two main techniques for that: one is to move the laser in the xz plane following the desired resonator profile, usually a \cos^2 function. This can be used to produce resonators with a large radius of curvature. If a small mode area is required, however, I carve the resonant structure by shining the laser just at two spots for a limited amount of time and letting the tail of the Gaussian beam overlap to create a bulge with a radius of curvature of the order of the diffraction limit of the laser. In my experience the highest Q-factor is achieved with the two-spots technique. The reason probably being that in this technique the volume of glass where the resonant light travels is never exposed to high intensity of the CO_2 laser, reducing the thermal stress and damage to the glass.

All the steps of the machining create a fine glass dust that evaporates from the rod and immediately solidifies; part of this dust gets in contact with the hot surface of the rod and sticks there. This deposition can be clearly seen by the microscope objective as a milky surface scattering the illumination light and helps me to judge the shape of the resonator, but sadly scattering does not go well with high Q-factor. To remove the deposition, machining of the resonator is alternated to a scan of the laser at low power in the x direction that melts the deposition back to the surface, also laminar flow is established in the machining region to move away most of the glass dust produced⁷.

⁷Amorphous glass dust is reported to not cause silicosis but to be on the safe side I connected

With this method, I can reliably produce resonators with a Q-factor of 2×10^8 and Q-factors of 8×10^8 are possible with a few attempts. If a higher Q-factor is required it is possible to enclose the machining region in a dry nitrogen laminar flow that allows Q-factor up to 1.1×10^9 [58] to be reached.

This method is one of the best for research purposes since it allows a microresonator to be fabricated in less than an hour. Furthermore, it is possible to reliably achieve a Q factor over 10^8 in a large range of diameters up to 7 mm (cf. Table 2.1) and it is easy to install the resonator in a tapered fibre optic system. A major drawback of this system is the size of the microresonator. Due to the fabrication and the holding system, it is necessary to keep at least 15 mm of glass rod attached to the microresonator, also I observed that it is difficult to achieve high Q factor for resonators smaller than 400 μm diameter. Also, the mode area is of the order of the curvature radius at the tip of the resonator, hence at least a few hundred of μm^2 .

Another technique for realising microrod resonators is to use a diamond turning machine instead of a CO_2 laser to shape the glass rod [88]. This method makes it possible controlling the shape of the microring resonator on a much finer detail. It is possible to realise a so called photonic belt that is a square protrusion on the surface of the glass rod allowing single mode operation, geometrical control of the dispersion and much smaller mode areas. However this technique requires machining times up to a week for a single resonator.

2.8 Microdisks and Microtoroids

Rod resonators show their limitations when resonators with smaller diameters and a compact design are required, such as integrated devices. In this case on-chip fabrication is the preferred technique, since it allows accessing diameters down to 20 μm while maintaining almost the same Q-factor accessible with rod resonators. These kinds of resonators are realised in a wealth of different materials. Some examples are lithium niobate LiNbO_3 [89], gallium arsenide GaAs [90], silicon Si [91], and silicon nitride Si_3N_4 [92]. But for the scope of this thesis I used fused silica SiO_2 starting from a silicon substrate with a top oxidised layer. The wafer is masked in circular shape and the silicon oxide is etched away everywhere else. Then, the silicon is etched from below the SiO_2 disc with an isotropic etch in order to leave the exhaust of the machining box to a fume extractor with HEPA filtering system.

just a silicon pillar holding the structure. An optional step is to anneal the silica disc with a high power laser to smooth the outer edge to reduce the roughness left by the etching process and therefore increasing the Q factor.

This method however, requires a clean room facility and the production of etching masks that makes every change in the design very time consuming. On the other hand, several microresonators can be produced in a single batch and is it possible to realise relatively small microresonators with really high yield and repeatability.

Coupling to this kind of resonator is usually obtained with tapered fibres but it is also possible to realise a waveguide with the same technique [93].

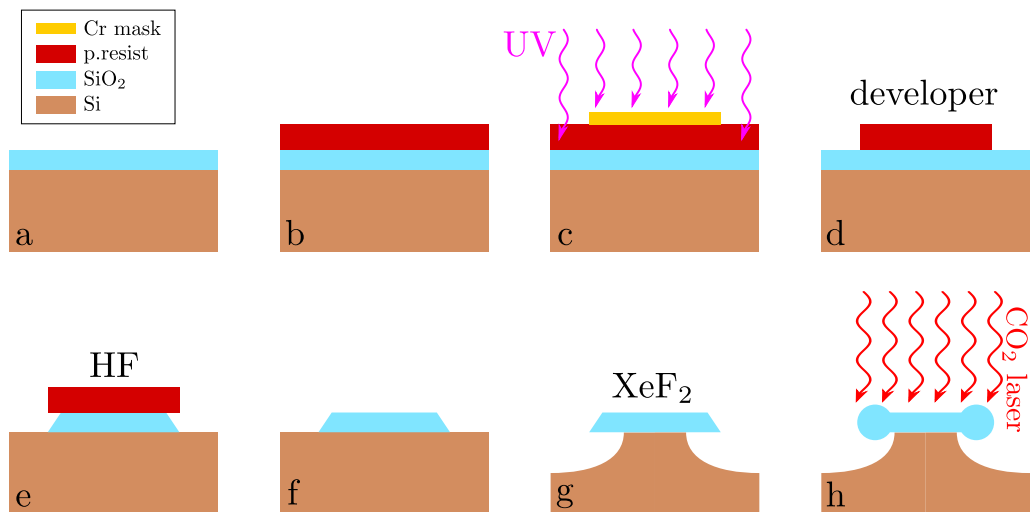


Figure 2.9: Steps of the photolithographic process. a) Thermally oxidised Si wafer. b) Spin coating. c) Exposure. d) Development. e) HF wet etching. f) Photoresist removal. g) XeF_2 dry etching. h) CO_2 laser reflowing.

2.8.1 Photolithography

I fabricate toroids and disks by photolithography and a combination of wet and dry etching following the general technique developed in [94]. The process starts with a silicon wafer with a thermal oxide layer grown on both sides of it. The oxidation is performed by an external company. I use oxide layers of 2 or 6 μm ; Thinner than 2 microns it is difficult to achieve high Q-factors, probably because the optical mode has a significant overlap with the surface and therefore more scattering losses. Thicker layers, instead, require a very long oxidation time that increases the cost of the wafer so thermal oxidation above about 8 μm is not practicable. The oxidation

time for thick layers is well described by the Deal-Grove [95] model,

$$t = \frac{X^2}{B} + \frac{X}{B/A} \quad (2.86)$$

where the coefficients for wet oxidation at 1000 °C are $A = 0.89$ and $B = 0.34$. To give an order of magnitude it takes 15 hours of wet thermal oxidation, i.e. baking the wafers in water vapour at 1000 °C, to obtain a 2 μm oxide layer, while it takes 5 days to obtain 6 μm.

I first cleave a 3 inch round wafer to a square and then I cleave the square in half to get 2 rectangles of about 2.5 cm by 6 cm that are more manageable for the rest of the process. I cleave the wafers by scratching the chip with a diamond scribe to create a weakness in the crystal structure of the silicon and then gently bend the chip. If the bending force is applied along the lattice direction the silicon breaks in a straight line opposing no resistance. If too much force is applied in an even slightly tilted direction the chip breaks in a curve or shatters. Furthermore, the silicon dust generated by the cleaving process may stick electrostatically to the chip and it is very difficult to remove. Once the chip is cleaved I proceed with a standard photolithographic etching process to remove the silica layer everywhere but on circular structures that are going to form our microresonator. First, I spin-coat a photoresist on the wafer surface. A photoresist is a polymer that changes its solubility in a chemical solution called developer if exposed to UV light. I use Microposit S1813 that is a positive photoresist, meaning that the polymer is weakened by the UV light, hence the exposed portion becomes soluble in the developer (Microposit MF-319). The last 2 digits on the name S18**13** indicate the viscosity of the polymer; in particular, our photoresist will form a 1.3 μm thick layer if spun at 4000 RPM.

Once the wafer is coated, I bake it on a hot plate for a minute at 110 °C to solidify the polymer and prevent it from sticking to the photomask. The photomask is a soda lime glass with a chrome pattern deposited on one side containing the feature that I want to etch on the surface. The chrome blocks the UV light from the mask aligner protecting the photoresist underneath. Therefore, after the development, the same pattern of photoresist will remain on the oxide layer. One of the masks I designed is shown in Fig. 2.10. Several sizes of resonators fit in a single mask and each microfabrication batch produces tens of resonators, however the time from the design of the mask to the final resonator is much longer than rod resonators and

can take up to a month.

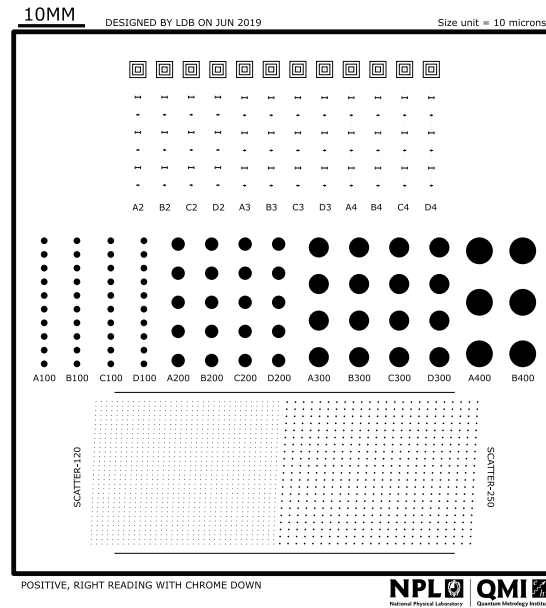


Figure 2.10: *Photomask used in the microdisks and microtoroids fabrication. The black color correspond to the parts covered in Cr. The top row contains disks with diameter of 20, 30 and 40 μm , there are also some alignment features for the reflow CO_2 laser. The mid row contains larger resonators from 1 mm to 4 mm that do not need alignment feature. The bottom row is a pattern of resonators slightly tilted with respect to the lattice structure. Cleaving this pattern likely results in having a disk on the edge of the chip for prism coupling.*

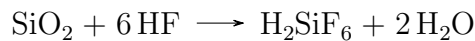
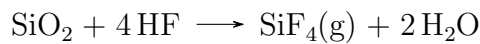
The dose of UV radiation is critical. An over-exposure will result in stray light also weakening the photoresist under the mask resulting in irregular edges on the photoresist that propagate to the final resonator limiting the Q-factor drastically. An under-exposure instead means that not all the thickness of the photoresist has received enough UV light to become soluble so it either does not get removed from the substrate, or very long developing times are required to remove it, causing the problems described later on. It is possible to calculate the correct exposure time by knowing the UV dose required by the photoresist and the irradiance of the mask aligner however it is far more practical to experiment with different exposure times and adjust to obtain the best result. I expose the mask for 20 to 25 seconds.

After the coated wafer has been exposed nothing is visible on the surface until the exposed photoresist has been removed by the developer (MF-319). As for the exposure time, the development time is crucial to obtain high Q-factor. Too short and not all the exposed photoresist is removed leaving halos and marking. Too long

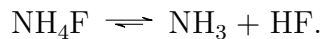
and the developer starts to attack also the unexposed photoresist, especially the perimeter of the circle that may have received some stray UV light during exposure; this is particularly evident when trying to compensate an underexposure with a long development time in order to remove all the photoresist from the empty area: the result is often a jagged disk profiles. This problem can be easily spotted on a microscope and up until this point in the process, it is possible to wash the wafer with acetone and start over since nothing has been done to the oxide layer yet. I usually develop for 40 to 45 s.

2.8.2 HF etching

After development I proceed to the wet etching phase to dissolve the silicon oxide but not the silicon substrate. HF etches SiO_2 with the reaction:



However, pure HF etches SiO_2 too fast and irregularly and also attacks the photoresist. Therefore, I use buffered HF that is a solution of



The chemical equilibrium between the two sides generates HF as it is consumed by the etching process and keeps the concentration at 10 %. This solution etches silica at the speed of about 1 nm/s therefore it takes about 1 hour and 40 minutes to etch a 6 μm oxide layer or 30 minutes to etch a 2 μm oxide layer. To verify that all the oxide has been etched, one can use the fact that SiO_2 is hydrophilic while Si is hydrophobic. If deionised water (DI) does not stick on the surface, the etching is done.

Now the disk resonator is ready, however I need to remove the silicon underneath the outer portion of the disk because silica has a lower refractive index ($n = 1.444$) than silicon ($n = 3.45$) therefore light would leak in the substrate instead of staying in the ring. Also, it would be very difficult to couple light to a structure protruding just 2 μm from a 5000 μm wide chip.

2.8.3 XeF₂ etching

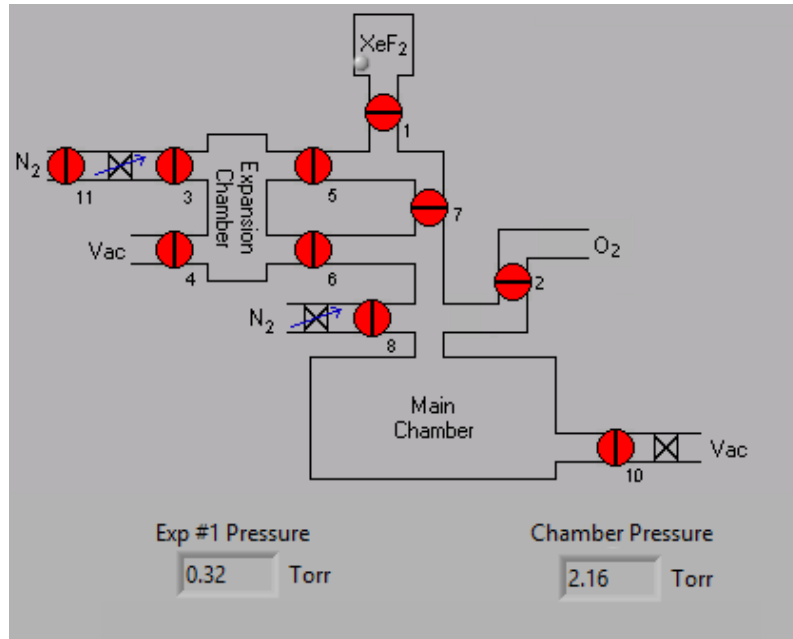


Figure 2.11: Schematic of the XeF₂ etching machine as represented on the control software. The red circles represent electro-actuated valves.

To etch Si but not SiO₂ there are different possible approaches. Wet etching, as the name suggests, employs etchants in the liquid form. A common etchant for silicon is potassium hydroxide (KOH) that is mostly used in electronics. This is suitable for realising disk resonators, since at concentrations below 20% and temperatures below 50 °C it etches Si 1000 times faster than SiO₂. However, KOH etching rate is very dependent on the crystal orientation⁸ resulting in square pillars.

To realise microtoroids I need the pillar to be as round as possible, therefore I need isotropic etching. This can be achieved with dry etching with XeF₂, which is a solid at atmospheric pressure but sublimates at about 4 Torr. It interacts with silicon with the following reaction:



Unlike most dry etching processes that require ion bombardment, this is a spontaneous reaction that takes place on the surface of the Si; therefore the etching is completely isotropic. Also, both the etchant and the by-product are gases therefore there is no precipitation on the resonator surface.

⁸< 100 > and < 110 > planes are etched 400 times faster than the < 111 > plane

I perform XeF_2 etching in cycles. The etching machine can be described as a system of two independent vacuum chambers connected with several valves between themselves and to a source of dry nitrogen, a reservoir of XeF_2 crystals and a vacuum pump as shown in Fig. 2.11. The valves are software controlled to cyclically prepare a mixture of the etchant in the expansion chamber, transfer it to the etching chamber where the sample sits and remove the exhausted etchant.

Before starting the etching cycles, the etching chamber is purged with nitrogen several times to remove all the humidity and oxygen, whereas the expansion chamber is prepared a few times with the concentration used for the etching and then evacuated. For each etching cycle the procedure is the following. First, the expansion chamber is filled with XeF_2 up to the required pressure by opening the valves (1,5) connecting to the XeF_2 Reservoir. Then nitrogen is added (11,3) to reach the set pressure, effectively diluting the etchant. This slows down the process but improves uniformity and reduces roughness. Once the etching mixture is ready the expansion chamber is connected to the etching chamber (6) for about a minute. During this time the XeF_2 reacts with the silicon. The reaction is exothermic hence, at the end of the etching interval, nitrogen is added (8) to increase the pressure and promote conductive cooling of the sample. After a short cooling delay, both chambers are connected to the vacuum pump (4,10) and completely evacuated before a new cycle starts. After the last cycle, the etching chamber is purged again with nitrogen to remove all the by-products of the reaction before exposing the sample to air. A typical etching recipe involves 20 to 200 cycles of 60 s etching with 3 Torr of XeF_2 and 1.5 Torr of N_2 . The cooling process is performed adding 5 Torr of N_2 and waiting for 10 s. Each cycle etches a fixed quantity of silicon hence the number of cycles needed depends on the surface of exposed silicon in the sample.

2.8.4 Reflowing

At the end of the XeF_2 etching, I obtain a wedge-shaped disk on top of a silicon pillar that already exhibits a Q-factor of the order of 1×10^7 up to 2×10^8 . As mentioned in Section 2.1.2, one of the main limitations to the Q-factor in our case is the surface scattering. In these resonators, the optical mode is guided mostly by the bottom surface and the diagonal side of the disk. Depending on the angle of the wedge, the mode interacts more or less with the outer edge connecting the two.

The quality of these surfaces depends mostly on the oxide growth process that is out of our control and the HF part of the fabrication. The XeF_2 is practically inert for SiO_2 [96, 97] so I expect no effect on the Q from this last processing step.

I have loose control on the angle of the wedge by using or not hexamethyldisilazane (HMDS) on the SiO_2 surface before spin-coating with photoresist. HMDS is an adhesion promoter and it affects the speed at which HF attacks the contact plane between photoresist and SiO_2 . Without HMDS, HF penetrates the interface and lift the photoresist, producing a shallower edge and vice versa. I found out that leaving the HF to etch just for the time needed to remove the oxide layer result in a protrusion on the edge of the disk. I believe that this produces surface scattering that lowers the Q factor of the resonator [98]. For shallow wedges, the mode “lives” away from the edge so this problem is lessened. Alternatively, I can get rid of the protrusion by extending the etching time. In this case, I can use a steeper edge.

When an high Q-factor is required, I perform an additional step on microdisks. By using a CO_2 laser it is possible to melt the silica disk to obtain a microtoroid as shown in Fig. 2.12. I first defocus the laser so that the intensity is uniform on

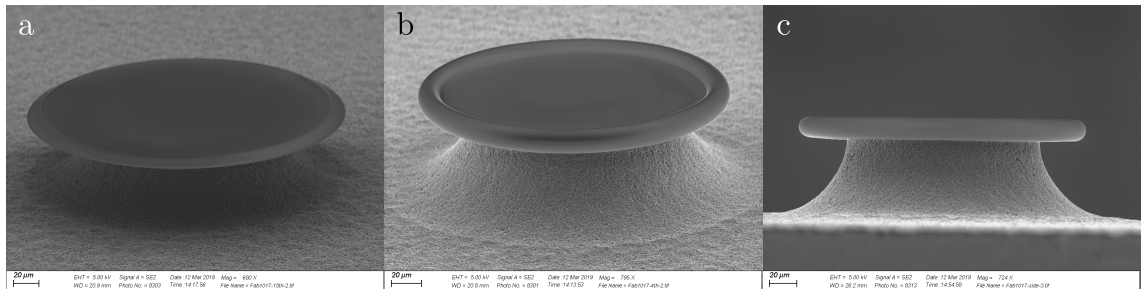


Figure 2.12: *Scanning electron microscope images. a) Microdisc resonator not reflowed with the CO_2 laser. b) Microtoroid resonator after the CO_2 laser reflowing. c) The same resonator as b) seen from the side.*

the surface of the microdisk, then I hit the resonator from above with a short burst from the CO_2 laser. A typical burst is 15 W of power for 0.2 s but this parameters change with the diameter of the resonator and the spot size. Generally a couple of resonators are sacrificed to calibrate the burst.

In this process, physics works for me. The silicon pillar is a good conductor, with thermal conductivity of $130 \text{ Wm}^{-1}\text{C}^{-1}$ similar to most metals, while silica is a thermal insulator with a thermal conductivity of $1.3 \text{ Wm}^{-1}\text{C}^{-1}$. This means that the central part of the thin layer of SiO_2 does not heats up because the silicon pillar conducts heat away. The edge of the disk instead absorb the laser light and cannot

dissipate heat being surrounded by air, so it melts. At this scale, surface tension is much stronger than gravity so the molten glass forms a toroid around the pillar. The process self terminates when the toroids reaches the pillar that cools the silica. Having a round pillar is paramount in this case so only XeF_2 etched resonators can be reflowed while this is not possible for the one fabricated with KOH etching. If the pillar is perfectly round, the minor radius of the toroid is constant along the circumference because there is the same amount of material protruding from the pillar at each point. Also the major radius profile along the circumference now depends on the shape of the pillar. Reflowing disks larger than $500\ \mu\text{m}$ is possible by moving the laser spot along the surface ensuring spatial overlap between the single pulses.

2.9 Alternative microresonator platforms

The two techniques mentioned above are the ones that I implemented and optimised during my PhD. It is worth mentioning a few additional techniques that provide different advantages or allow for different kind of experiments.

Microspheres

Microspheres are the first kind of microresonators used in optics [18]. They are generally realised by melting the end of an optical fibre with a CO_2 laser, and hydrogen flame or an electric arc. And have a shape similar to a lollipop (see Fig. 2.13 (a)) These kind of resonators achieve a Q-factor comparable with microrisks but present a few drawbacks. The diameter of the resonator has to be larger than the original fibre but not too large otherwise gravity starts to overcome the surface tension and deforms the glass. Also, there is no defined plane in a sphere, hence there could be modes travelling on several planes. This does not happens in the other kinds of resonators because light that is not travelling in the symmetry defined plane is not in a closed loop, hence does not resonate.

Microbottles

The generally high finesse of microresonators makes them an exceptional platform for sensing. Having a narrow linewidth, well spaced from the neighbouring ones makes it easy to detect any small loss related broadening or any frequency shift of

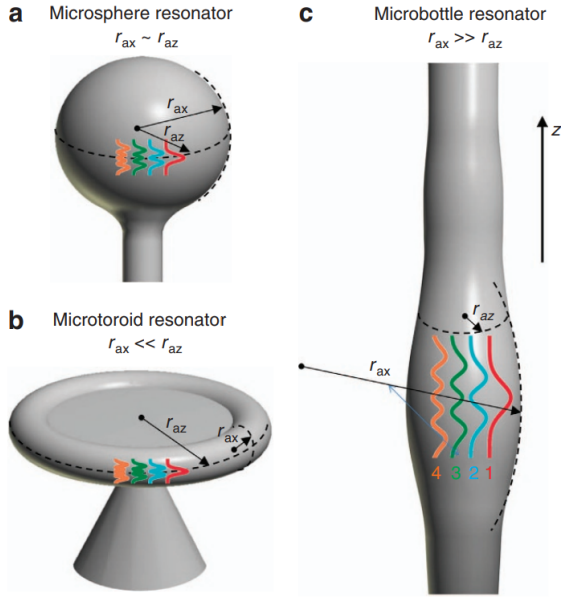


Figure 2.13: Three kind of resonators. (a) Microsphere. (b) Microtoroid. (c) Microbottle. Adapted from [99].

the resonance. Such a frequency shift provides a straightforward method of measuring the temperature of the resonator, hence the surrounding environment[56] as described in Section 2.4. The evanescent field propagating outside the resonator interacts with the refractive index of the surrounding material, whether it is a gas or a liquid [100] or even molecules [101, 102] and solid particles [103]. Both the real part and imaginary part of the refractive index can be measured: The real part changes the effective refractive index seen by the optical mode, shifting its frequency, while the imaginary part increases the absorption losses, broadening the linewidth.

Unfortunately, a flow of liquid or gas at the coupling point is likely to shake the tapered optical fibre used for the light coupling hence producing a disturbance much larger than the effect one attempts to measure. A way around this it to use more stable coupling methods such as prisms. Microbottles provide another clever solution to this problem. They are realised by locally heating a glass tube while increasing the pressure inside [104]. Alternatively a polymer is deposited on a rotating fibre [105]. This creates a bulge similar to a rod resonator (see Fig. 2.13 (c)) even if the radius of curvature is generally larger leading to a larger mode area and the existence of transversal modes. However, the glass can be made so thin that the guided optical mode leaks both outside and inside the bottle so that the outside can be used to couple light into and out of the mode, while the liquid or gas under investigation can be flown inside the glass tube where it interacts with the

evanescent field. Also, the high field intensity can be used to trap particles close to the surface of the bottles

Waveguides

As in the case of microbottles, it is not necessary to have the inside of the resonator to be filled. The resonant optical mode travels close to the outer edge of the ring, hence the resonator can be fabricated just as a ring instead of as a full disk.

This is mostly the case for waveguides where, using lithographic techniques, it is possible to draw closed loops waveguides in almost any geometry including non-circular patterns [106]. Furthermore, it is possible to replace the tapered fibres for coupling with other waveguides fabricated with the same technique, solving also the problem of phase matching. Fig. 2.14 shows a SEM image of a silicon nitride Si_3N_4 resonator laying on SiO_2 with its coupling waveguide fabricated by my colleagues. The lithographic techniques allow to realise ring or racetrack shaped waveguides

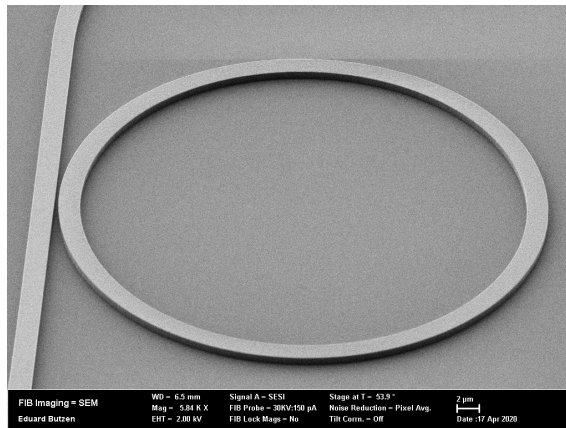


Figure 2.14: A Si_3N_4 waveguide resonator and waveguide on SiO_2 substrate. Courtesy of Shuangyou Zhang.

with radii of curvature of the order of a few μm and widths of the order of the wavelength or smaller, producing small mode volumes and, in principle, reducing the characteristic power to observe nonlinear effects at the mW level [107] or below. Furthermore, it would be possible to integrate the control electronics and even the laser [108] on the same chip.

This method differs from the previous ones because the light is usually confined by the refractive index contrast between the waveguide and the substrate at least on one side of the waveguide. This requires the substrate to be optically transparent at the wavelength of interest, limiting the possible choices. Furthermore, chemical

processes of lithography often leave rough interfaces that scatter light reducing the Q factor [21].

To summarise the common points of this technique, a general advantage is the variety of materials that can be used to realise waveguides and cladding and this is one of the most promising technique to integrate microresonators with electronics circuits (the other one being wire bonding [109]). Waveguides show a much smaller mode area, of the order of λ or less, that helps to observe nonlinear effects as we found above. Squeezing the field, however, makes it interact much more with the interface between the waveguide and the cladding that is generally not as smooth as for the microrods or microtoroids; also the cladding may have some absorption at the wavelength used. This is why waveguides usually show lower Q-factors than the other techniques presented in this section.

2.10 Tapered optical fibres

As mentioned above, optical fibres are one of the devices that allow the guided optical mode to produce evanescent field to couple to the microresonators. This is particularly important when aiming for critical coupling, since if the field overlap is not enough this condition cannot be reached [63, 67, 110].

The basic recipe to realise a tapered fibre is a source of heat and a mean of holding and pulling an optical fibre as highlighted in Figure 2.15. In the work

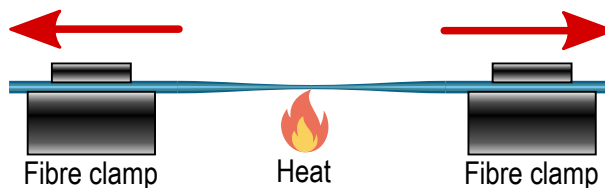


Figure 2.15: *Schematic of the tapering setup. The fibre is clamped on translation stages that are pulled apart while the fibre its heated to the softening point. The source of heat could be either a electric oven or an hydrogen flame.*

presented in this thesis two techniques are used to realise tapered SMF-28 optical fibres: a ceramic heater and a hydrogen flame.

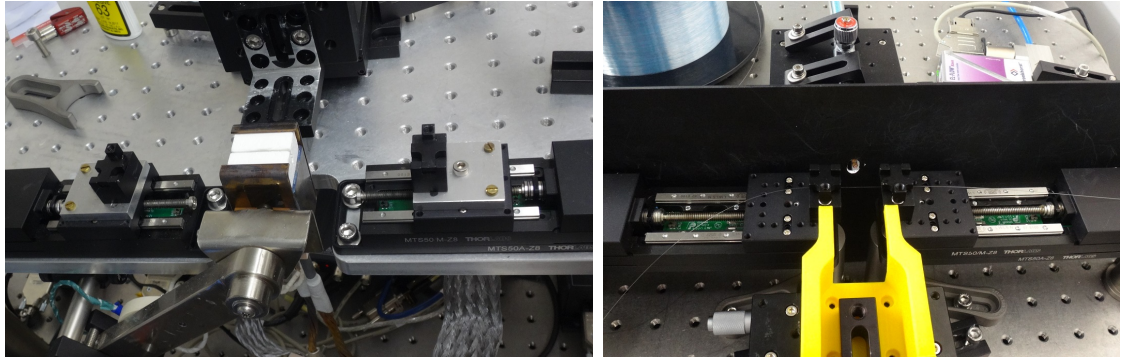


Figure 2.16: *Tapering setups. On the left, the one based on a ceramic heater that is the white cube in the centre of the picture. On the right, the setup based on the H_2 flame. The brass nozzle emitting the flame is visible in the centre of the picture.*

Ceramic heater

A ceramic heater, shown in Figure 2.16 (left), is constituted by a high temperature resistant filament enclosed in a ceramic cube with a side of about 4 cm. A slit cut in the cube makes it possible to lower a section of optical fibre into the heated area and a thermocouple measures the temperature and provides the feedback to the filament current driver. To taper a fibre a section of about 6 cm is stripped off the coating and placed into two v-groove holders. The oven is then heated up to an indicated temperature of 950 °C and the fibre is slowly pulled at a speed of about 1 mm/min up to a length of 60 mm. Then the oven is cooled down slowly and once the temperature is below 600 °C the fibre is tensioned by an additional 0.03 mm. The tensioning stage ensures that all the slack in the fibre is removed before glueing it to the aluminium bracket that supports it. If the fibre is loose it is very difficult to position it accurately in the evanescent field of the resonator mode. The fibre is then glued to a 10 cm wide bracket with epoxy glue or UV curing glue. The region where the glue is applied is part of the tapered part but the diameter at that point is large enough that the mode does not leak into the glue. Two extensions are applied to the bracket to support the remaining part of the stripped fibre and to avoid breaking the taper by handling the rest of the fibre.

Hydrogen Flame

Despite being a very repeatable process, the ceramic heater method presents several drawbacks. The solution to most of them is to replace the heat source with a Hydrogen, flame as shown in Figure 2.16 (right).

The flame is produced by burning H_2 from a tank with the oxygen in the air and is about 3 mm wide and 5 mm tall. To keep it stable and obtain reproducible tapers, the surrounding of the H_2 nozzle are protected from air gusts and the flow of hydrogen is controlled by a mass flow controller. Also, the nozzle is mounted on a precision translation stage to reproducibly adjust the position of the flame relatively to the fibre.

The working principle is identical to the ceramic heater but there are a few advantages. First is it possible to reduce the length of the taper from 10 cm (4 cm is the length of the heater and an additional 6 cm are due to the pulling) down to less than 3 cm. This is because the flame has a dimension of about 4 mm and since the length to taper is less, it is generally enough to pull for 18.7 mm in total. Since the dimension is smaller both the pulling speed (0.7 mm/min) and the tensioning (0.015 mm) are reduced. Having a shorter tapered region allows one using a smaller (36 mm wide) and lighter bracket to hold the fibre directly from the coated part, hence it is possible to realise compact experiments. Also, the positioning of the taper in the resonator evanescent field is greatly improved because the coupling point is much closer to the holding tine, hence the slack due to the elasticity of the fibre is minimised.

Another advantage is the much shorter cooling time of the hydrogen flame, in the order of a few seconds. The ceramic heater and its support remains hot for a long time after tapering and cannot be cooled or heated more than $50\text{ }^\circ\text{C}/\text{min}$. This slow cooling is particularly annoying if multiple tapers have to be manufactured sequentially or if a fibre breaks during fabrications because it takes almost an hour to cool and re-heat the ceramic element.

There are alternative methods to heat the fibre for tapering. Some research groups use an oxi-hydrogen flame [111] that has the advantage of not storing a hydrogen cylinder in the lab or have a hydrogen line in the walls. However, this kind of flame is sensible to small changes in the mixture between O_2 and H_2 . Other methods include oxi-butane flames or CO_2 lasers. Our fibre splicer can produce tapered fibres using the same electric arc used for splicing but with different setting. The tapers produce with this methods are mainly for dispersion control. The electric arc tapers tend to be too abrupt and generally the diameter is above $10\text{ }\mu\text{m}$, hence they are not suitable for evanescent field coupling.

Single mode tapered fibre

To verify that the tapered fibre is again single mode it is enough to check in real time the transmission of the fibre itself. When the core becomes too small to sustain even the fundamental mode, the light is guided by the refractive index contrast between the cladding and the air. Since the original cladding diameter is of the order of $125\ \mu\text{m}$, the fibre is multimode during the first stages of tapering. As the tapering continues the number of modes changes and their relative effective pathlength varies because the geometry is changing. All the different modes interfere with each other during the tapering making the transmitted power fluctuate over time during the tapering. Initially, the fluctuation is small in amplitude and slow because the number of modes is higher and the relative change in diameter is slow. As the tapering progress, the oscillation frequency increases up to a point where the oscillation amplitude increases momentarily because of the reduced number of modes and then suddenly stops. This is the sign that the tapered fibre is single mode again but now the guiding refractive index contrast is the one between the cladding and air. The fibre can be tapered further after this point to further reduce the diameter hence increase the amount of the mode travelling in the air without significant losses in the transmission. Fibres tapered with this method are surprisingly robust to tension but tremendously weak against shear forces to the point that it is possible to break the fibre just going through it with a finger or tool and not noticing the break. Also the fibre is very elastic at this diameter and, even if broken, tends to go back to straight, making it difficult to identify a broken taper.

2.11 Beyond fused silica

The major requirements for the material used to fabricate the microresonator are to be easily machinable into the desired shape, to be transparent in the optical region of interest and to show a high nonlinear refractive index n_2 . As highlighted in Section 2.5 the power required to observe nonlinear effects depends also on the Q factor and the mode volume.

One of the most commonly used material is fused silica (SiO_2 in its amorphous form). It is a particular kind of glass without impurities or other dopants. It is a very popular material in optics but can also be obtained by oxidation of a Si wafer

therefore it can be used in any of the aforementioned fabrication techniques.

MgF₂ has a crystalline structure. Its characteristics are similar to fused silica, with a slight lower nonlinearity, however, it is transparent in the mid-infrared allowing to explore other spectral regions [112, 113].

CaF₂ is another crystal worth mentioning because it shows one of the highest Q factors ever achieved in microresonators [114], however, it has thermoelastic and thermorefractive coefficients of opposite signs making very difficult to lock the resonator to the laser frequency.

Si₃N₄ is one of the most popular materials for the realisation of waveguide-type microresonator given its nonlinear refractive index is ten times higher than fused silica. One of the main obstacles with this material is to obtain a Q factor as high as fused silica, since the etching processes leave the material surface rougher, producing a consistent amount of scattering. Recently, this kind of resonators has closed the gap with the other fabrication methods [92].

Material	SiO ₂	MgF ₂	CaF ₂	Si ₃ N ₄
n	1.44 [115]	1.37 [116]	1.43 [117]	2.00 [118]
$n_2(10^{-16} \text{ cm}^2/\text{W})$	2.7 [37]	0.9	1.9	24
Q	$\sim 5 \cdot 10^8$	$\sim 2 \cdot 10^8$	$3 \cdot 10^{11}$	$1.7 \cdot 10^7$

Table 2.1: List of refractive index, non linear refractive index and achieved Q factor for some of the most common materials used for microresonators.

To conclude this non-exhaustive list of materials⁹ it is worth mentioning lithium niobate (LiNbO₃) [119]. Besides reaching the remarkable Q of 10⁸, it is a non-centrosymmetric material, meaning that it also shows a second order susceptibility $\chi^{(2)}$ and an electro-optic effect, paving the way for the study of several interesting nonlinear phenomena and a new method of resonator tuning with an electric field.

2.12 Conclusions

In this chapter, I presented a linear-coupling mathematical model for one optical tapered fibre with a ring resonator. I then adapted the model to the specific case

⁹This is the first table in this thesis that introduces typical values for Q and n_2 . It must be said that Q varies greatly with the fabrication, even more than an order of magnitude. The same goes for the nonlinear refractive index n_2 that depends on the material, in particular for Si₃N₄ the ratio between the two atoms significantly changes the optical properties.

of high-Q-factor resonators and extracted the expressions for measurable quantities. Finally, I normalised the model to the characteristic dimensions of the system so that it can be used in simulations and analytically to derive general results.

I then analysed the advantages of microresonators for the study of nonlinear optics, specifically their small mode volume and high Q-factor.

I compared the two microresonators platforms used in this thesis with the alternatives and described the fabrication method I use to realise them. Glass-rod resonators are fast to fabricate and can be rapidly prototyped to meet the experimental needs. However, their large size and mode volume, when compared to the alternatives, makes them suitable just for proof of principle devices and not for final products. On the other hand, microtoroids and microdisks are a step towards on-chip integration and present a much smaller mode volume than rod resonators with a similar Q-factor. these platforms are ideal to observe nonlinearity at low power but require a longer design and fabrication time.

Finally, I presented two methods of fabricating tapered fibres: from the initial approach with a ceramic heater, I improved the fabrication time, the compactness of the setup and the coupling strength by changing the heating mechanism to a hydrogen flame.

Chapter 3

Symmetry breaking

As mentioned in the introduction, this thesis was supposed to be on the “Kerr frequency combs generation in microresonators”. I wanted to exploit the Kerr effect to generate pulsed light from a continuous laser or, in the frequency domain, to generate multiple wavelengths from a single one. In particular, my first idea was to generate two frequency combs in the same resonator but in opposite directions. Ideally, using only one resonator would have cancelled most of the differential noise with huge advantages for spectroscopy applications.

What I was about to find out that it is not possible to couple light in two directions simultaneously if the power of the input and its detuning from the resonance frequency falls in a specific range. This discovery was completely tangential to the original project but it led to a series of insights that I will elaborate upon in the following chapters.

But let us start from the beginning and do this in an orderly fashion. In this chapter I describe how the thermal effect and the Kerr nonlinearity affect the resonance shape, or in other words, why all the Lorentzian resonances in this thesis look like triangles and the light propagation in the resonator. Then I will describe the key physical reason of symmetry breaking: the fact that XPM is twice as strong than SPM. Once these fundamental concepts are dealt with, I will implement them in the theory developed in Chapter 2 and re-normalise it to characteristic units. We will then be ready to demonstrate theoretically the spontaneous symmetry breaking and discuss some interesting features.

Since I call myself an experimental physicist, it is finally time to describe the experimental setup used to demonstrate spontaneous symmetry breaking in mi-

croresonators, and test the theoretical model by analysing the results.

3.1 The Kerr effect

The Kerr effect describes the variation of the refractive index of a material as a function of the optical intensity I . In particular, the change in refractive index in the material is linear with the circulating light intensity. The intensity is a difficult quantity to access experimentally. Also, the intensity is not constant in the cross-section plane perpendicular to the propagation direction but we can consider the average intensity in the mode described as the ratio between the circulating power P_{circ} and the effective mode cross-section area A_{eff} , which is conveniently defined as the area necessary to produce the observed Kerr shift. In practice, A_{eff} is similar to the $1/e$ area of the quasi-Gaussian mode propagating in the resonator. It is possible to write the refractive index n as:

$$n = n_0 + n_2 I \quad (3.1)$$

Where n_0 is the linear refractive index at the frequency of interest and n_2 is the nonlinear refractive index. This is the case when considering a single propagation direction in a dielectric. But what happens when there are counter-propagating directions and the dielectric is a closed loop? Let us focus on one part at a time.

3.1.1 XPM is twice as much as SPM

So far we considered light propagating in one direction. However, when light propagates in opposite directions the Kerr effect becomes even more interesting. Indeed, the effect of counter-propagating light on the refractive index is twice as much the light propagating in the direction of interest. This is the case in dielectric media with both directions having the same frequency, polarization and being in the same spatial mode. The part of the Kerr effect arising from the mode of interest on itself is called self phase modulation in contrast the to effect of other light on the mode of interest, which is cross phase modulation. The combination of the two can be expressed as

$$\Delta n_A = n_2 \frac{(P_A + 2P_B)}{A_{\text{eff}}} \quad \Delta n_B = n_2 \frac{(P_B + 2P_A)}{A_{\text{eff}}} \quad (3.2)$$

where A and B are the two directions and A_{eff} is the effective mode area.

Different circulating powers P lead to different refractive indices in the two directions. Figure 3.1 shows the limit case where the power in one direction is much greater than the other. The direction labelled as P_A has significantly more power

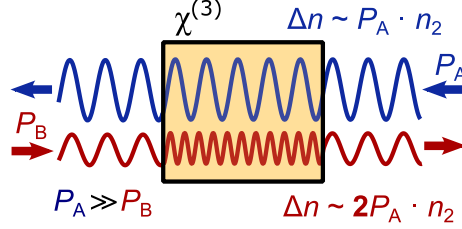


Figure 3.1: Illustration of the Kerr interaction between counter-propagating light in the case of one direction being significantly more powerful than the other. Adapted from [87].

than the other direction. Thus, we can neglect the weak direction and find out that the Kerr shift is twice as much in one direction than the other.

$$\Delta n_A \propto P_A n_2; \quad \Delta n_B \propto 2P_A n_2; \quad (3.3)$$

Now, we already know that a different refractive index leads to a different resonance frequency and a different coupled power for the same input power. This is a significant hint that the Kerr effect may be the explanation for the symmetry breaking that I observed in my first experiment.

Before describing how the Kerr effect can result in different coupled powers even with the same input power in the two directions, let me first linger on a justification for the factor of 2 between SPM and XPM. Most of the publications about the topic (including ours) use the phrase “it is well known” but it would be interesting to justify this statement for once. There are several approaches to show that this factor exists and the one I chose, is to start from equation describing the polarisation of a dielectric material and expand it for the case of two counter-propagating fields in a material with $\chi^{(3)}$ nonlinearity. It is an expansion of 64 polynomial terms $+c.c.$ and there is not much more in it than algebra but at the end, it results in the contribution of the counterpropagating mode being twice the mode itself.

Nonlinear optics refer to the nonlinear response of the optical material, or specifically its polarisation, to the electric field applied. We can write the case of linear optics as:

$$P(t) = \varepsilon_0 \chi E(t), \quad (3.4)$$

where P and E are the polarization of the dielectric material and the electric field, ε_0 is the electric permittivity of vacuum and χ is the susceptibility. For the sake of this demonstration, we will use scalar fields and assume that χ is a scalar.

If the response is nonlinear we can write the polarisation as a Taylor expansion:

$$P(t) = \sum_{n=1}^{\infty} \varepsilon_0 \chi^{(n)} E^n(t) \quad (3.5)$$

$$= \varepsilon_0 \chi^{(1)} E(t) \quad + \varepsilon_0 \chi^{(2)} E^2(t) \quad + \varepsilon_0 \chi^{(3)} E^3(t) \quad + \dots \quad (3.6)$$

$$= P^{(1)}(t) \quad + P^{(2)}(t) \quad + P^{(3)}(t) \quad + \dots \quad (3.7)$$

Here the first column after the equal sign represent the linear response. The second column is the second order nonlinearity, generally responsible for phenomena such as second harmonic generation (SHG) or sum and difference frequency generation (SFG, DFG). In centro-symmetric materials like the ones used in this thesis, it is generally possible to neglect second order processes because, for geometrical reasons, $\chi^{(2)} \simeq 0$. The third column represents the third order nonlinearity, which includes one of the topics of this thesis: the Kerr effect. Let us now calculate the third order term,

$$P^{(3)}(t) = \varepsilon_0 \chi^{(3)} E^3(t), \quad (3.8)$$

in the case of counter-propagating light. The field can be written as two components having the same frequency but opposite wavevector k

$$E(t) = E_A e^{i(\omega t + kx)} + E_B e^{i(\omega t - kx)} + \text{c.c.} \quad (3.9)$$

Note that, in principle, it is possible to generate other frequencies than the original input via processes such as FWM [3, 91], but in this section our goal is only to verify the twofold contribution of the Kerr effect to the change in refractive index. Hence, let us calculate Eq. (3.8) for the field in Eq. (3.9). This results in 64 terms but, in this case, we are interested only in the ones oscillating at the frequency ω , i.e. the ones that describe no frequency change. Let us write these terms,

$$P_{\omega}^{(3)}(t) = \varepsilon_0 \chi^{(3)} [(3E_A E_A^* + 6E_B E_B^*) E_A e^{i(\omega t + kx)} + \quad (3.10)$$

$$(6E_A E_A^* + 3E_B E_B^*) E_B e^{i(\omega t - kx)}] + \text{c.c.} \quad (3.11)$$

Note that the terms in round parenthesis are proportional to the power in each direction and they are multiplying the electric field at the first power. However, the counter-propagating field appears with the factor 6 while the field itself has a factor 3. We can then interpret these terms as an additional nonlinear refractive index n_2 defined as

$$n_2 = \frac{3}{2n_0^2\epsilon_0c}\chi^{(3)}, \quad (3.12)$$

assuming that the intensity is defined as $I = \frac{1}{2}n_0\epsilon_0cE^2$.

This results in an intensity dependent change in refractive index of

$$\Delta n_{A,B} = n_2 I_{A,B} + 2n_2 I_{B,A} \quad (3.13)$$

It is now evident that counter-propagating light induces twice as much refractive index change than co-propagating light at the same frequency. In other words, the XPM is twice as strong than SPM. The same reasoning can be used to demonstrate that co-propagating but at different frequencies experiences the same ratios between XPM and SPM.

$$n = n_0 + n_2 I = n_0 + \frac{3\chi^{(3)}}{8n_0} |E|^2 \quad (3.14)$$

Where n_0 is the linear refractive index at the frequency of interest and n_2 is the nonlinear refractive index that is directly related to the third order susceptibility $\chi^{(3)}$ as shown in Eq. (3.14).

3.1.2 Kerr effect in a ring resonator

In the previous chapter we analysed how the refractive index affects the resonance frequency (see Eqs. (2.5) and (2.54)). Then, in a Kerr nonlinear resonator, the circulating power affects the resonance frequency. This is because an increase in the refractive index slows the light in the resonator or, in other words, increase the effective length of the resonator. The Kerr effect creates a coupling between the circulating power and the resonance frequency. Since the circulating power depends on both the input power and the laser detuning from the cavity resonance, this introduces nonlinearity in the response of the resonator and a feedback effect that will be discussed in the rest of this thesis.

Tuning the frequency of the laser down into a resonance from blue detuned the

light starts to circulate within the resonator, increasing its refractive index since n_2 is typically positive. The increase of refractive index moves the resonance to lower frequencies, away from the laser. The more the laser moves towards low frequencies the more light couples into the resonator, moving the resonance frequency down with the laser. This results in the frequency offset between the laser and the resonance being stable for small fluctuation, thus it provides an effective frequency locking mechanism. This lock behaves as a simple proportional feedback without and integral or derivative component, in other words, there is no preferred point on the side of the resonance and the coupled power will drift over long periods of time as the ambient temperature or the laser frequency drift. When the laser frequency passes over the resonance to the red detuned side, the coupled power decreases, moving the resonance back towards its low-power value, therefore reducing the coupled power even more. This results in the resonator abruptly jumping out of resonance with the laser. It is possible to lock to a resonance only on the blue detuned side and this is the situation where the microresonators are typically operated.

It is worth clarifying the concept of detuning and resonance since these two words are critical to the whole thesis. By resonance frequency ω_{res} I mean the frequency of the laser that would produce the maximum intensity in the cavity at that instant in time, all other parameters being unchanged. The meaning of resonance can be extended to describe the profile of the power coupled in the resonator for every frequency that the laser could have. Since we are dealing with nonlinear effects, the resonance frequency changes continuously under the influence of the thermal and Kerr effects. The only measurable parameter is the amount of power that is coupled into the resonator and the amount that continues straight in the coupling fibre. However, a mental picture of the whole resonance helps to understand the physics of our system.

Following from the definition above, the difference between the unperturbed resonance frequency ω_0 and the laser frequency is defined as detuning Δ . Since the resonance moves around, another useful quantity to be defined is the effective laser detuning Δ_{eff} , which represents the frequency difference between the laser frequency and the effective resonance frequency. It is given by the laser detuning from the low power limit resonance frequency plus the Kerr frequency shift¹, as illustrated in

¹Eventually the thermal shift can be added to the model as a time and power-dependent detuning

Fig. 3.2.

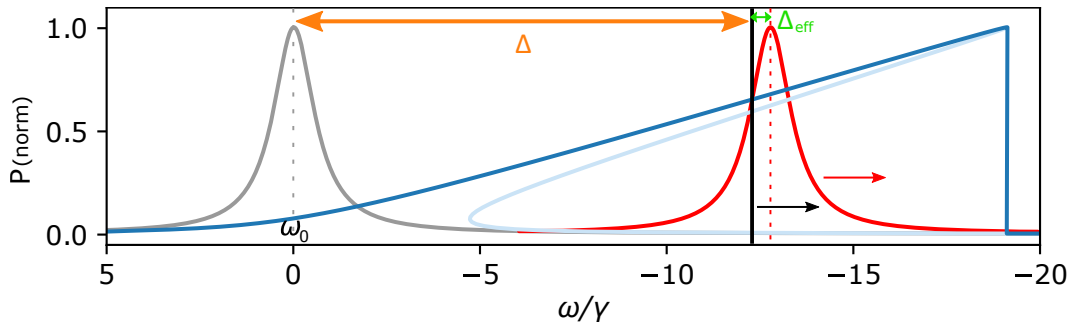


Figure 3.2: *Definition of the detuning. A plot of the normalised coupled power as the laser (black) is scanned across the resonance towards lower frequencies. The 0 for the x axis is arbitrarily set to the cold cavity resonance frequency (in grey), i.e. the resonance as it appears when the power is too low to observe any nonlinearity. At higher power, the resonance is tilted by the thermal and Kerr effect (blue). The detuning is represented as an orange arrow. The effective resonance (red) moves with the laser (black). The effective detuning, i.e. the difference between the laser frequency and the effective resonance is indicated in green. The frequency axis is reversed to match the experimental measurements shown later.*

Note that changing the laser frequency by the effective detuning does not result in getting the laser in resonance. It is important to remember that any variation in the laser frequency corresponds to a change in the coupled power, which influence the Kerr shift, thus the effective detuning.

In this notation, a positive effective detuning corresponds to the laser oscillating at a higher frequency than the resonance frequency, and it is thus being blue detuned. Conversely, a negative effective detuning means that the laser is on the red side of the resonance. Note how, in Fig. 3.2, Δ is negative by several times the half linewidth γ , corresponding to the laser being red detuned from the ‘cold’ resonance. However, the Kerr effect is shifting the resonance and the effective detuning Δ_{eff} is positive, in other words, the laser is on the blue side of the effective resonance. This is the typical regime in which we operate since the Kerr and thermal effects provide negative feedback to the detuning resulting in a stable state [81]. The thermal effect does not play a role in the symmetry breaking because the temperature of the material only depends on the total power in the resonator and does not differentiate between the directions of propagation.

This interaction between coupled power and resonance frequency results in a characteristic resonance shape of a tilted Lorentzian represented in light blue in

Fig. 3.2, however once the laser pass over to the red side of the resonance the resonance quickly returns to its cold value resulting in the blue shape in Fig. 3.2.

3.1.3 Power dependency of the refractive index

It is time to derive a quantitative value for the Kerr shift described so far. We can use Eq. (3.1) to write the effect of an infinitesimal increment of the circulating power on the refractive index in the case of SPM,

$$\partial n = n_2 \frac{\partial P_{\text{circ}}}{A_{\text{eff}}} \quad (3.15)$$

If we recall the condition for resonance from Eqs. (2.5) and (2.54) describing the resonance frequency we can express it in terms of angular frequency as:

$$\omega_{\text{res}} = m \frac{c}{rn} \quad m \in \mathbb{N} \quad (3.16)$$

And then we get the relation between resonance frequency and circulating power:

$$\frac{\partial \omega_{\text{res}}}{\partial P} = \frac{\partial \omega_{\text{res}}}{\partial n} \frac{\partial n}{\partial P} = -\frac{\omega}{n} \times \frac{n_2}{A_{\text{eff}}} \quad (3.17)$$

For XPM, of course, we just need to multiply this power depended resonance shift by 2.

$$\frac{\partial \omega_{\text{res}}}{\partial P} = -2 \frac{\omega}{n} \times \frac{n_2}{A_{\text{eff}}} \quad (3.18)$$

Cross phase modulation is not limited to the case of counter-propagating light. Having a different frequency propagating in either direction still induces XPM.

3.1.4 Characteristic power for the Kerr Effect

Let us now introduce the Kerr effect as a shift in resonance frequency in the linear Eq. (2.78) we found in the linear case:

$$\frac{2\pi}{\mathcal{F}_0} P_{\text{circ}} = \frac{\eta P_{\text{in}}}{1 + \left(\frac{\Delta}{\gamma} \right)^2} \quad (3.19)$$

We already have a quantity describing the difference between the laser and the resonance frequency, the detuning between the laser and the resonance frequency, which is defined in its normalised form as $\delta = \Delta/\gamma$. So $\delta = 1$ corresponds to being a HWHM away from the resonance.

We already saw that the Kerr effect produces a shift linearly proportional to the circulating intensity so we can add it as an additional detuning component. Since we measure power and not intensity, I will express the Kerr detuning in the form,

$$\frac{2\pi}{\mathcal{F}_0} P_{\text{circ},A,B} = \frac{\eta P_{\text{in},A,B}}{1 + \left(\frac{\Delta}{\gamma} + \frac{P_{A,B}}{P_0} + 2 \frac{P_{B,A}}{P_0} \right)^2} \quad (3.20)$$

where $P_{A,B}$ is the power coupled in each direction and P_0 is the characteristic power that we use to normalise.

It would be wise to define P_0 such that a normalised power $p = P/P_0$ of one would produce the same shift as a detuning of one, $\delta = 1$. So the question is: Which is the input power that produces a frequency shift of γ ? Or in mathematical terms:

$$P_{0,\text{circ}} \left| \frac{\partial \omega}{\partial P} \right| = \gamma, \quad (3.21)$$

$$P_{0,\text{circ}} = \gamma \frac{n_0 A_{\text{eff}}}{\omega n_2} \quad (3.22)$$

where I used the circulating power because it is the one that drives the Kerr effect (see Eq. (3.17)). However the rest of the theory is expressed in units of the external power or coupled power so I will divide by the cavity enhancement factor defined in Equation (2.77).

$$P_0 = \frac{2\pi}{\mathcal{F}_0} \gamma \frac{n_0 A_{\text{eff}}}{\omega n_2} \quad (3.23)$$

We can use the formula for the Q-factor, $Q = \omega/2\gamma$, to obtain:

$$\boxed{P_0 = \frac{\pi n_0 A_{\text{eff}}}{Q \mathcal{F}_0 n_2}} \quad (3.24)$$

In the presence of multiple resonant modes it may not be easy to identify the same mode one FSR away hence it may be difficult to measure the finesse. We can

express the finesse in terms of Eqs. (2.56), (2.57) and (2.64)

$$\mathcal{F}_0 = Q_0 \frac{2\pi}{\left(\frac{\pi n_0 d}{c}\right) \omega}$$

Hence:

$$P_0 = \frac{\pi n_0 A_{\text{eff}} \pi d n_0 \omega}{Q \mathcal{F}_0 n_2 2\pi c}. \quad (3.25)$$

If we identify the mode volume as $V_{\text{eff}} = A_{\text{eff}} \pi d$, and use the relation $\lambda = 2\pi c/\omega$ we find

$$P_0 = \frac{\pi n_0^2 V_{\text{eff}}}{\lambda n_2 Q Q_0} \quad (3.26)$$

P_0 is one of the main figure of merit of a microresonator. It represents the characteristic input power needed to observe nonlinear effects and it allows comparing different platforms. As an example Si_3N_4 resonators generally have a Q two orders of magnitude lower than fused silica rod resonators, however they have a much smaller mode volume and higher nonlinearity. Calculating P_0 allows to decide which platform is better to observe nonlinear effects at low power and also demonstrate that microresonators are an excellent platform to observe nonlinear effects compared to other resonant structures. Free space cavities usually have mode volumes that are far larger than the ones achievable in microresonators because the mode area is far larger. Similarly, fibre-loop cavities have a much longer circumference hence P_0 is higher than in microresonators.

Of all the parameters appearing in P_0 , I can measure directly in the experiment the Q-factors and the wavelength of the laser. The refractive index n_0 and the nonlinear refractive index n_2 are known from the literature But I cannot measure A_{eff} accurately, the only way is a Comsol Multiphysics simulation but even this approach is limited by the limited knowledge of the precise geometry of the resonator. These large errors in the calculation leave two possible ways open: leaving P_0 as a free parameter in the fittings or estimate it indirectly as described in Section 3.4.1. The frequency detuning is normalised naturally by the HWHM linewidth since it is the same parameter that characterises a Lorentzian. In particular, we choose the coupled linewidth since this allows absorbing the coupling parameter in the normalisation and develop the theory without dealing with it continuously. Let me remember the

definition for the normalised detuning

$$\delta = \frac{\Delta}{\gamma}. \quad (3.27)$$

The circulating power is normalised according to Eqs. (3.24) and (3.26) as follows

$$p = \frac{2\pi}{\mathcal{F}} \frac{P_{\text{circ}}}{P_0}, \quad (3.28)$$

Finally, the normalised input power is defined as:

$$\tilde{p} = \frac{\eta \tilde{P}}{P_0} \quad (3.29)$$

With these ingredients, I can finally write the equations for the Kerr symmetry breaking in a normalised form

$$p_{A,B} = \frac{\tilde{p}_{A,B}}{1 + (\delta + p_{A,B} + 2p_{B,A})}, \quad (3.30)$$

where A, B represent the two possible directions of circulation of light.

This definition has the advantage of bringing the normalised circulating power to values that can be directly compared with the normalised input power. Indeed, with this normalisation, p never exceed \tilde{p} , and the two are equal just for resonant critical coupling. This condition helps to better visualise how efficiently the power is transferred into the cavity. When reporting the values calculated with this normalisation to physical units, it is important to remember that the circulating power needs to be multiplied by the cavity build-up factor $\mathcal{F}/2\pi$ that in a practical case could be of the order of 10^6 .

Now you may ask: wait a minute! Isn't the thermal effect another source of nonlinearity? It is indeed. The main difference between the Kerr and thermal effect is that the latter does not differentiate between the directions of propagation. Hence, the thermal effect plays no role in splitting the resonance frequency between the two directions. The only effect is to extend the frequency scale and deform the shape of the resonance. We corrected for this by rescaling the frequency axis accordingly in Fig. 3.15 (b).

3.2 Symmetry breaking

I will now explain how the coupled equations that we just found can describe symmetry breaking. When equal amounts of light from both directions couple into the resonator, there is a standing wave as the result of two counter-propagating traveling waves. The symmetry breaking phenomenon is described in 3.3. When sending equal light power in both directions, the resulting field in the microresonator is a standing wave pattern created by the interference of between the two counter-propagating waves. As the laser is tuned towards the resonance, or the input power

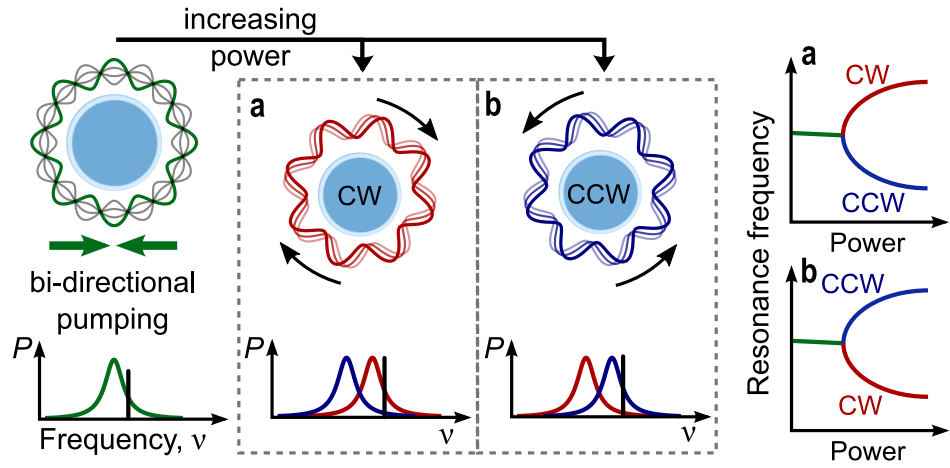


Figure 3.3: *Illustration of the symmetry breaking. At low power, both directions couple equally into the resonator resulting in a standing wave in the resonator. Increasing the input power splits the resonance frequency so that only one random direction couples into the resonator. Adapted from [87].*

is increased, the power in the resonator increases. For high enough coupled power, suddenly the field inside the resonator becomes a travelling wave in one direction. This is because the symmetry of the system breaks and one direction couples more light into the resonator than the other. The less coupled direction still shows a reduction in transmission. This can be explained with a resonance frequency split. But where does this frequency split comes from?

3.2.1 Qualitative description

Before digging in the mathematical explanation of why this happens let me describe the symmetry breaking in a more physical way. In case of a completely symmetric situation with laser light propagating in both direction with identical characteristics such as power, polarization, and frequency, light will couple identically into the

resonator in both directions and create a standing wave. Due to the thermal effect in fused silica, there is a stable condition where the laser is blue detuned from the cavity resonance. However, this perfect symmetry is not possible in the real world. There is going to be a slight difference in polarization, power, or any other characteristic that will imbalance the coupled power of the two laser beams as shown in Figure 3.4 (a,b). If the CW direction temporarily couples a bit more power in the resonator while the coupled power in the CCW direction stays the same, the resonance frequency is red-shifted by $\Delta n_{\text{CW}} \propto \Delta P_{\text{CW}}$ while the CCW resonance $\Delta n_{\text{CCW}} \propto 2\Delta P_{\text{CW}}$. This is the beginning of a runaway effect because now the CCW detuning increases and the CCW power decreases (Figure 3.4 (c)). Hence, the CCW push on the CW resonance also reduces, increasing the CW coupling and circulating power (Figure 3.4 (d)). This runaway effect continues making a significant difference appear between the circulating powers in the two directions despite the pump powers being equal.

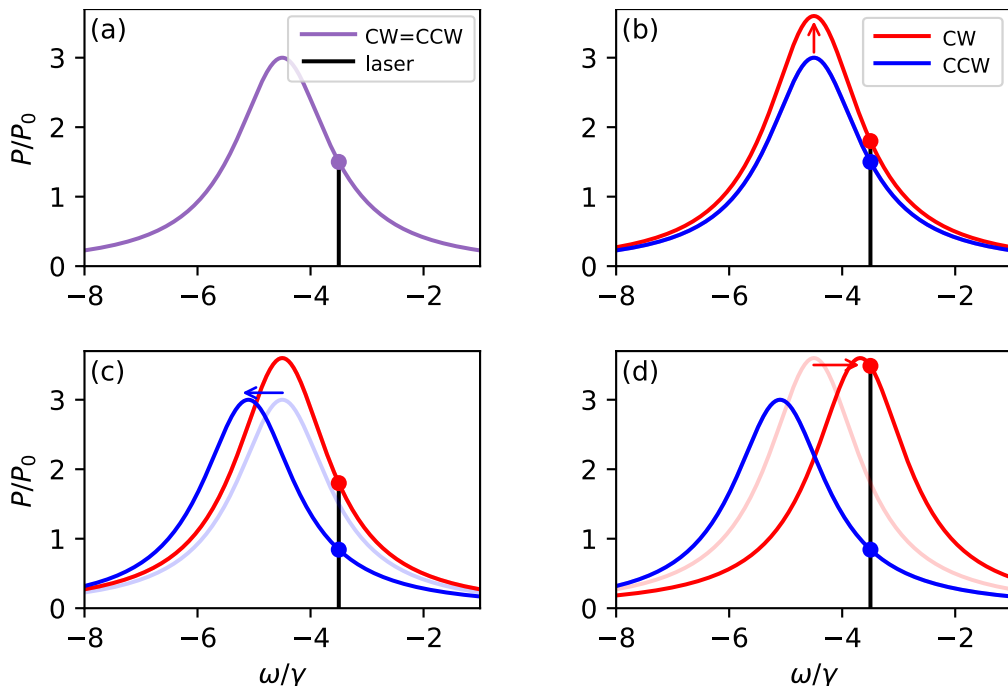


Figure 3.4: Step by step description of the symmetry breaking. The laser frequency is represented in black. Coupled powers in each direction are represented by the red and blue dots while the resonance is shown in the same colour. (a) The initial symmetric state with light from both direction equally coupled into the resonator on the high-frequency side of the resonance. Small perturbations increase the light coupled in the red direction (b), this causes a greater shift away from the resonance in the blue direction (c) resulting in less power coupled. Hence, the red direction is now less shifted by the XPM and moves closer to the resonance (d).

The coupled powers can change following a variation in the input powers, the frequency of the inputs or a difference in the Kerr shift. I will use this representation in various part of the thesis because I find it helpful to describe what is happening in the resonator. However, it is important to highlight that this is just a representation. The Lorentzian resonance is not a physical entity, only the intersection point between the laser frequency and the Lorentzian response, representing the coupled power is a physical quantity. However, drawing the instantaneous lineshape helps to better visualise the detuning. Also, the drawn lineshape is not accessible by scanning the inputs since coupling additional light in the resonator would shift the resonances due to the Kerr effect. However it is possible to verify that this lineshape exists by using a independent weak probe [120]. The height of the Lorentzian should be normalised to 1 since it represents the response of the resonator to the input power nevertheless I prefer to scale the height of the Lorentzian such that it represents the maximum power that could be coupled in the resonator.

3.2.2 Theory

Let us extract this behaviour from the coupled equations (Eq. (3.30)):

$$p_{1,2} = \frac{\tilde{p}_{1,2}}{1 + (\delta_{1,2} + p_{1,2} + 2p_{2,1})^2} \quad (3.31)$$

The goal is to find all the pairs of coupled powers (p_1, p_2) that solve the equation given the free parameters that we can control in the experiment, namely the input powers $\tilde{p}_{1,2}$ and the laser detunings $\delta_{1,2}$ in the 2 directions. To unravel the 2 equations we can solve for p_2 in the first equation and find:

$$p_{2\pm} = \frac{-\delta_1 - p_1 \pm \sqrt{\frac{\tilde{p}_1}{p_1} - 1}}{2} \quad (3.32)$$

Note that this expression is actually composed of two equations with either sign of the square root. Substituting this in the equation for p_2 I find:

$$\frac{p_{2\pm}}{\tilde{p}_2} [1 + (\delta_2 + p_{2\pm} + 2p_1)^2] = 1 \quad (3.33)$$

From here I can define a solving function:

$$s_{\pm}(\delta_{1,2}, \tilde{p}_{1,2}, p_{1,2}) = s_{\delta_{1,2}, \tilde{p}_{1,2}}(p_1) = \frac{p_{2\pm}}{\tilde{p}_2} [1 + (\delta_2 + p_{2\pm} + 2p_1)^2] - 1 \quad (3.34)$$

The input power \tilde{p} and detuning δ in the two directions are fixed parameters and the circulating powers are related by Eq. (3.32). So all the zeros of the solving function correspond to a pair of circulating powers that solve the problem.

A more formal and analytical treatment of this equation can be found in [121]. For the purpose of this thesis, I will describe a numerical approach to the steady-state solution of the symmetry-breaking problem. Note that equal input power and detuning are required in the first place to have a symmetry to be broken. This will be the case for this chapter. But the equation discussed in this section does not require symmetry to be valid and can be applied to any combination of asymmetric input powers and detunings. Let us test the predictions from this equation. To find the zero-crossings, the s function is evaluated for a sufficiently fine list of values in the interval of allowed circulating powers $p_1 = (0, p_{1,in}]$, excluding the value of 0 to avoid poles. A first guess of the zero-crossing point is provided by the change of sign of s . This guess is then used as the starting point for a root finder algorithm `scipy.optimize.fsolve`². For each p_1 that solves Eq. (3.34) the corresponding p_2 is calculated from Eq. (3.32).

In Fig. 3.5 all the 3 solutions arise from the positive branch of Eq. (3.34). The middle one is a symmetric solution with $p_1 = p_2$ while the other two correspond to broken symmetry. Here, when p_1 is in the upper branch, p_2 is in the lower and vice versa. Looking at the resonance, it can be described as a tilted Lorentzian with a bubble-shaped solution on top. In Fig. 3.6 there are 5 solutions, 3 from s_- and 2 from s_+ . Only the highest of the s_- solutions and the lowest of the s_+ are symmetry broken. Note how the upper part of the bubble presents a concave region and now corresponds to a symmetry broken solution from the negative branch s_- . In Fig. 3.7 we analyse the region where the maximum number of 9 solutions is present. The symmetry broken bubble is now folding over at the chosen detuning. This results in 3 solutions in the upper branch and 3 in the lower branch. Each p_1 corresponds pairwise with a p_2 in the other branch.

²SciPy (pronounced ‘‘Sigh Pie’’) is a Python-based ecosystem of open-source software for mathematics, science, and engineering. It is usually installed with most python distributions and available at scipy.org

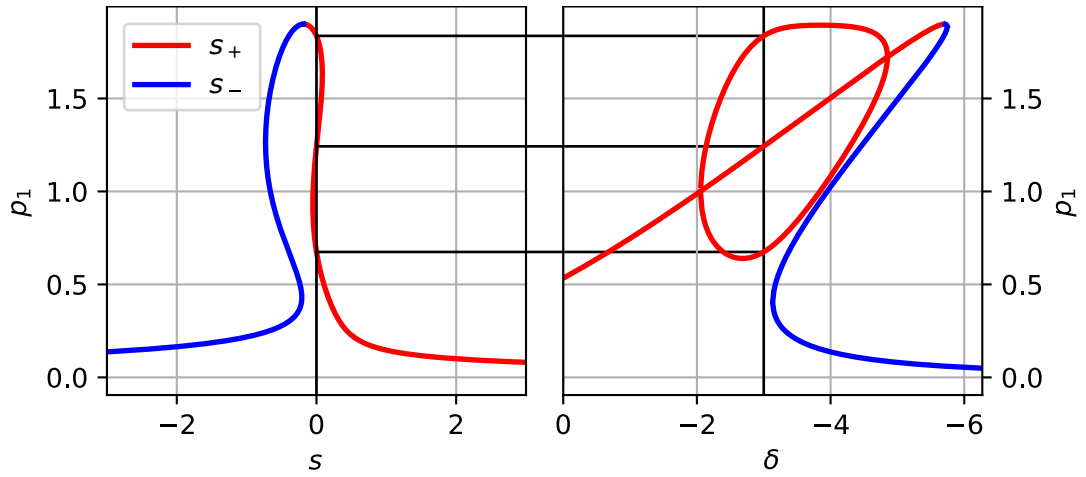


Figure 3.5: On the left, plot of the solving function s for input power $\tilde{p} = 1.9$ and detuning of $\delta = -3$. On the right, the bubble with the detuning of interest highlighted.

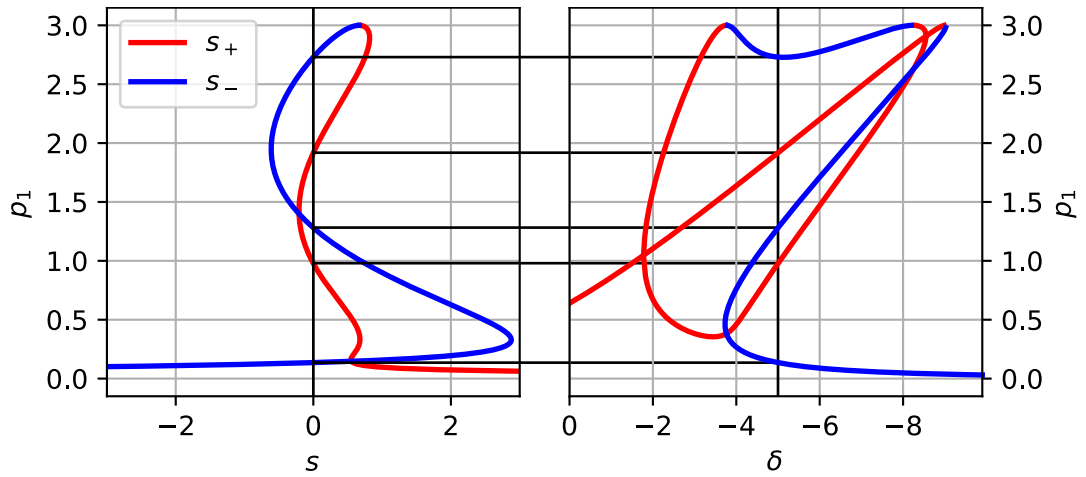


Figure 3.6: Same as in Fig. 3.5 for $\tilde{p} = 3$ and $\delta = -5$.

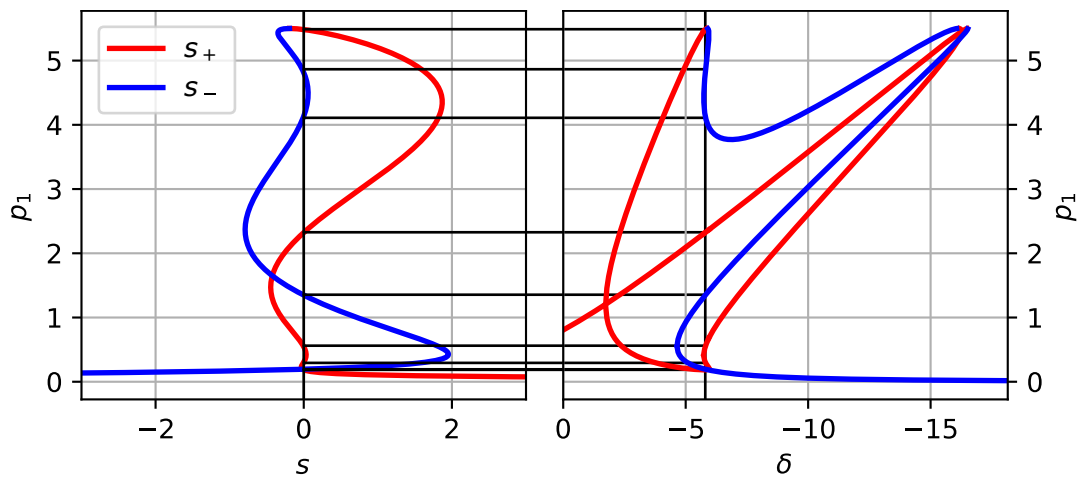


Figure 3.7: Same as in Fig. 3.5 for $\tilde{p} = 5.5$ and $\delta = -5.8$. (The 2 solutions for low p_1 are overlapped. One arise from the negative branch and one from the positive one)

Figure 3.8 shows the solutions of Eq. (3.31) for symmetrical pumping and several values of the input powers \tilde{p} . Let us take a look at the possible type of resonance profiles that can arise for different input power.

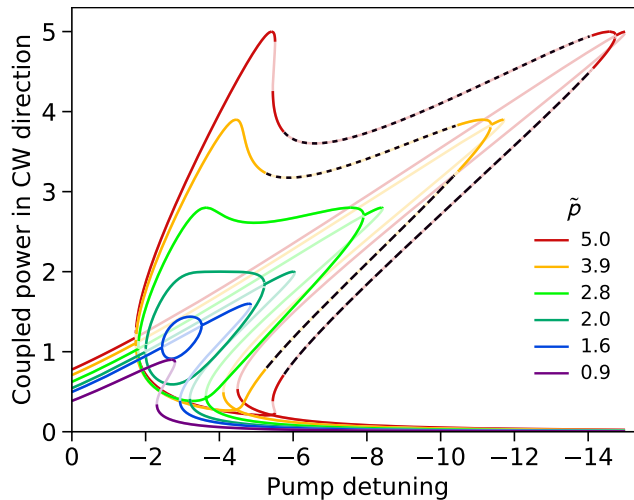


Figure 3.8: Solutions of equation Eq. (3.31) for different input power \tilde{p} . Coloured lines represent stable solutions, faint lines represent unstable solutions, and dashed lines represent oscillatory solutions.

First, it is evident the appearance of a “bubble” in the coupled power profile, by finely adjusting the parameters I observe that the threshold input powers to observe this effect is $\tilde{p}_{\text{th}} \simeq 1.54$. For powers below the threshold ($\tilde{p} = 0.9$) the only effect of nonlinearity is a tilting of the resonance. Just above the threshold ($\tilde{p} = 1.6$) the characteristic bubble-shaped solution appears. The upper and lower branches are stable solutions and corresponding to different coupled powers [121]. In other words, if p_1 is in the upper branch, p_2 is in the lower branch. The symmetric solution in between is now unstable. The solution for $\tilde{p} = 2$ is the limiting solution for which the bubble is convex. It is characterised by the flat-top shape where the circulating power p is equal to the input power \tilde{p} in the coupled direction. This is discussed in detail below. Past this point the solution is concave ($\tilde{p} = 2.8$) and there are values of the detuning for which one of the resonances is red shifted from the laser and the other is blue shifted. A further increase in powers lead to instability appearing on both branches ($\tilde{p} = 3.9$) where a growing oscillatory solution is expected (see [122] for more details). Experimentally, this situation usually results in jumping out of resonance. The high nonlinearity of the system and the thermal effect prevent us from observing diverging oscillations. However, by carefully tuning the experimental parameters and according to numerical simulations it is possible to observe oscillations in this region of the parameter space. A detailed explanation

of this regime falls outside the scope of this thesis but a detailed analysis of the phenomenon can be found in [121]. At even higher power ($\tilde{p} = 5$) the bubble folds over, resulting in two unstable but non-oscillatory regions on each symmetry broken branch. No other qualitative changes are observed at higher input power.

3.2.3 Special points

There are a few properties that can be identified from the model.

The switch from a negative to positive solution always happens at maximum coupling where $p_1 = \tilde{p}_1$. This follows from the structure of Eq. (3.32), since the square root is defined as real valued and the two solutions connect where the argument is 0. The case of maximum coupling at symmetric pumping deserves a closer look.

$$\tilde{p}_1 = \tilde{p}_2 = p_1 = \tilde{p}, \quad \delta_1 = \delta_2 = \delta \quad (3.35)$$

The solving equation and the expression for p_2 become respectively:

$$\frac{-\delta - \tilde{p}}{2\tilde{p}} \left[1 + \left(\delta + \frac{-\delta - \tilde{p}}{2} + 2\tilde{p} \right)^2 \right] = 1. \quad (3.36)$$

$$p_2 = \frac{-\delta - \tilde{p}}{2} \quad (3.37)$$

This gives a relation between the detuning of the input power at which one of the directions is fully coupled into the resonator as shown in Fig. 3.9. The first one is simply

$$\delta = -3\tilde{p} \quad (\tilde{p} > 0) \quad (3.38)$$

It represents the solution with the most negative detuning at which the resonance jumps out. This is not a symmetry-broken solution because the power in the other direction is also fully coupled (this can be verified by using Eq. (3.37) and it is shown in blue in Fig. 3.9). The other 2 solutions are:

$$\delta = \sqrt{\tilde{p}^2 - 4} - 2\tilde{p}; \quad p_2 = \frac{\sqrt{\tilde{p}^2 - 4} + \tilde{p}}{2} \quad (\tilde{p} > 2) \quad (3.39)$$

$$\delta = -\sqrt{\tilde{p}^2 - 4} - 2\tilde{p} \quad p_2 = \frac{-\sqrt{\tilde{p}^2 - 4} + \tilde{p}}{2} \quad (\tilde{p} > 2) \quad (3.40)$$

They appear for input power above $\tilde{p} = 2$ and represent symmetry broken solutions. Equation (3.40) in the limit of very high input power tends to the first solution (green in Fig. 3.9). This reinforces the intuition that at higher power the bubble closes just before jumping out of resonance. Equation (3.39) appears at the smallest detuning of the three solutions and corresponds to the lowest value of the power coupled in the other direction (orange in Fig. 3.9). In particular, for increasing input power in either direction, p_2 still tends to 0 as:

$$p_2 \simeq \frac{1}{\tilde{p}} + \frac{1}{\tilde{p}^3} + \frac{2}{\tilde{p}^5} + \frac{5}{\tilde{p}^7} + O\left(\frac{1}{\tilde{p}^9}\right) \xrightarrow{\tilde{p} \rightarrow \infty} 0 \quad (3.41)$$

hence, in the limit of high input power, the two solutions are one the reciprocal of the other in normalised power units, i.e. The coupled power is $p_1 = \tilde{p}$ and $p_2 = 1/\tilde{p}$.

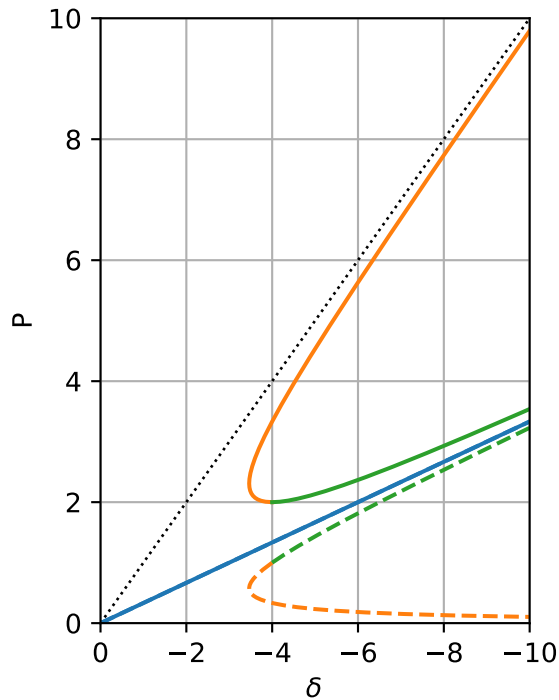


Figure 3.9: *Circulating power in the resonator when one direction is fully coupled. In blue, the solution corresponding to the tip of the tilted Lorentzian, Eq. (3.38), the circulating power is the same in both directions. The other two solutions appear for $\tilde{p} \geq 2$. In the graph the fully coupled direction is plotted with a line while the power in the other direction is plotted dashed. Orange is Eq. (3.39), green is Eq. (3.40)*

Let us now analyse how the negative branch solution implies that one direction has to be red detuned from the resonance.

It is possible to arrange Eq. (3.32) to highlight the effective detuning:

$$\delta_{1,2,\text{eff}} = \delta_{1,2} + p_{1,2} + 2p_{2,1} = \pm \sqrt{\frac{\tilde{p}}{p_{1,2}} - 1} \quad (3.42)$$

Since the square root is positive, it is clear how the solutions corresponding to the $-$ sign have a negative effective detuning for one of the directions. Equation (3.42) also reinforces the fact that full coupling ($p_1 = \tilde{p}$) corresponds to effective detuning equal 0.

The minimum input power in each direction to obtain symmetry breaking is:

$$\tilde{p}_{\text{th}} = \frac{8}{3\sqrt{3}} \simeq 1.54, \quad (3.43)$$

and the minimum detuning to obtain symmetry breaking is:

$$\delta = -\sqrt{3} \simeq -1.73, \quad (3.44)$$

as demonstrated in [121]. The threshold power is the same for modulation instability (MI) in microresonators [13, 29] in the case of no dispersion. However, some dispersion is always present hence the symmetry breaking effect kicks in before observing MI.

3.3 Methods

The fabrication of tapered fibres and resonator is described in Chapter 2. In this section, I will describe the mechanical part of the setup that allows coupling light into the microresonator and the optical setup before the resonator.

The major requirement for our setups is the capability of positioning the tapered fibre in the vicinity of the resonator so that there is overlap between the two evanescent fields. Since the typical evanescent field extension is the same order of magnitude than the wavelength, I need a position accuracy of a few nanometres. This is achieved with the combination of a 3D piezoelectric translation stage mounted on top of a 3D precision translation stage for extended travel range that can be seen inside the acrylic box in Fig. 3.10. I use different combinations of this system.

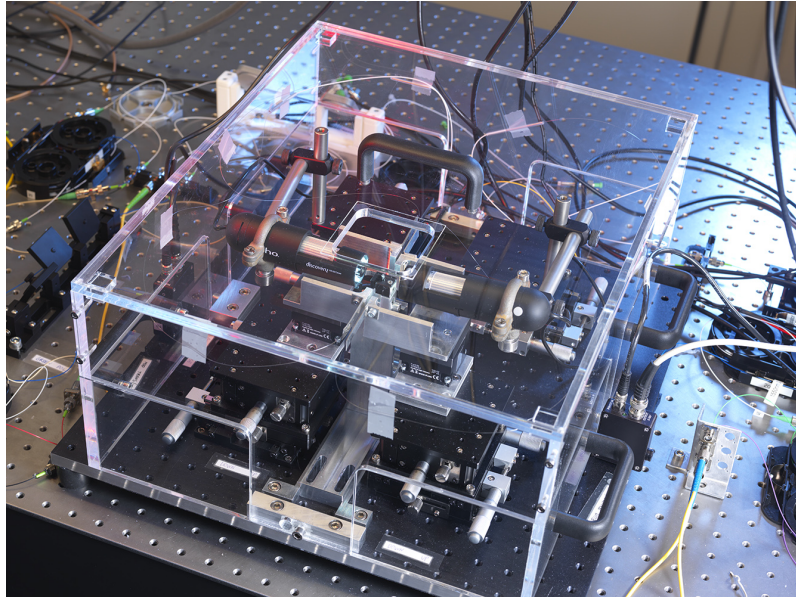


Figure 3.10: *Picture of the experimental setup used in Chapters 4 and 5 of this thesis. The microresonator, tapered optical fibres, translation stages and alignment cameras are protected from dust and air-flow by an acrylic enclosure. The black optical breadboard is separated from the pneumatically-suspended optical table by sorbothane feet.*

A PI Nanocube (120 μm travel range with 1 nm accuracy) mounted on top of a 3 axis micrometric stage (25 $\text{mm}_x \times 25 \text{mm}_y \times 15 \text{mm}_z$ travel range) is the most accurate system I use that simultaneously allows for ease of access when replacing the fibre or the resonator. An alternative system is the Thorlabs NanoMax stage MAX312D/M, which combine 20 μm travel range with 20 nm accuracy on the piezo, 4 mm travel range on the micrometric stages. The accuracy is still sufficient for the coupling, however, the limited travel range is sometimes a problem. To solve this, I use an additional XY translation stage on top of the NanoMax to extend the range. The more compact dimensions allow for the reduction of the height of the resonator support, improving vibration isolation. The toroid and disk resonators are laid on a mild adhesive on top of a fixed aluminium pillar, while the rod resonators are secured to a v-groove holder. Generally, all the translation stages move the taper support, but in a few setups the tapered fibre is fixed and the resonator is mounted on translation stages with no drawbacks. The design of the setup allows replacing just a tapered fibre or the resonator without damaging the other. A set of microscope cameras is needed for positioning the taper in the near field region of the resonator mode instead of breaking it by pushing it against the resonator pillar or the silicon chip as shown in Fig. 3.11. In the case of rod resonators, a side camera is enough for accurate positioning since the reduced focal length can be used

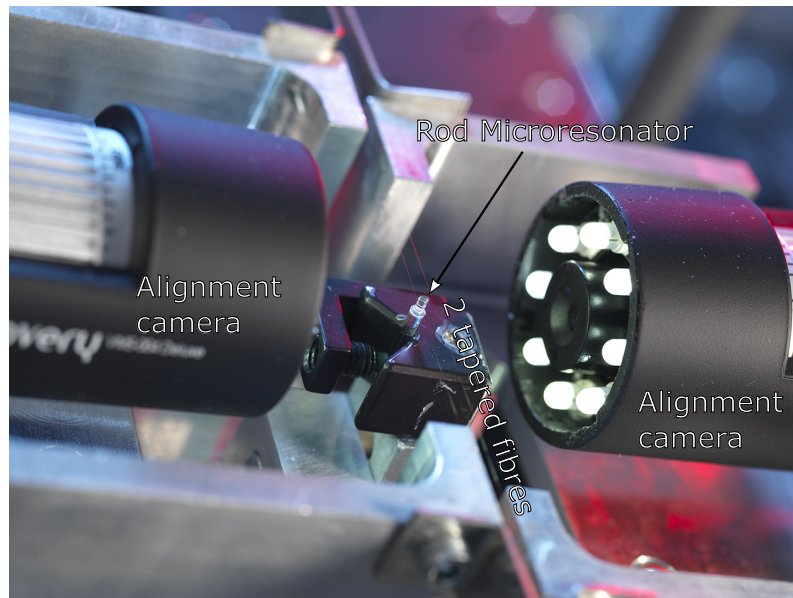


Figure 3.11: *Detail of the coupling region. Two USB microscope cameras are used to align the fibres to the resonator on each side and to illuminate the area. Two aluminium brackets hold the tapered fibres (highlighted in red by the background illumination) in the evanescent field of the rod microresonator that can be seen in the middle.*

to judge distance. For on-chip toroid resonators, both a side and top camera are needed given the smaller size and the different geometry.

The whole assembly is enclosed in an acrylic box with removable windows to protect the resonator from dust and airflow. The box is fixed on the bottom on a portable optical breadboard with the holes closed by tape, again to prevent air and dust flowing into the box. The breadboard itself is supported by sorbothane feet on a pneumatic optical table to isolate the experiment from vibrations coming from the building or other researchers working on the same optical table.

Figure 3.12 shows a scheme of optical setup used to measure the symmetry breaking. Laser light is provided by a continuously tunable external cavity diode laser (ECDL) model CTL by Toptica. The laser can be continuously tuned in a wavelength range of 10 nm around 1550 nm. Since I am studying a power-dependent phenomenon, the maximum output power of 50 mW would be limiting for this experiment. Therefore, the light is amplified with an erbium-doped fibre amplifier (EDFA) by IPG with a maximum output power of 1.5 W.

The light is then equally split into 2 branches with a 50:50 directional coupler. A manually controlled attenuator on each branch allows me to accurately balance the power in the two directions.

To couple light in opposite directions in the tapered fibre and simultaneously

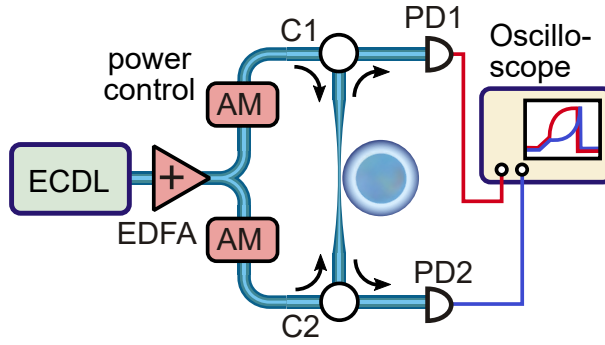


Figure 3.12: Scheme of the optical setup used to measure the symmetry breaking. The laser light is amplified and equally split in two branches. An attenuator on each branch allows to precisely balance the power in the two directions. A pair of circulators allow to send light in counter-propagating directions into the tapered fibre coupled to the resonator and observe the transmission in each direction. Adapted from [87].

observe the transmission I use circulators. Two photodiodes monitor the transmission in each direction (ThorLABS InGaAs amplified detector PDA05CF2 or the equivalent PDA10CF-EC. Bandwidth: 150 MHz. Response: 1 A/W).

3.4 Results and discussion

As mentioned at the beginning of this chapter we were attempting to generate counter-propagating frequency combs in a microresonator. Instead we observed the results in Fig. 3.13. The plot shows the transmission of the tapered fibre while scanning the laser frequency across the resonance from higher to lower frequency. This kind of scan allows me to search for suitable optical modes to generate frequency combs or to observe non-reciprocal light propagation. During the scan, I adjust the polarisation of light in both directions and the coupling position of the taper trying to optimise each resonance. I specifically look for a thermal triangle that is significantly extended in frequency and resonances that can reach zero transmission, i.e. critical coupling. The transmission in Fig. 3.13 is normalised to its value out of resonance for both directions. The laser frequency is scanned by supplying a triangular waveform voltage to the piezo input of the laser controller. The conversion factor between frequency and voltage is calculated by measuring the frequency with an optical spectrum analyser (OSA) at two different voltages and assuming a linear relation. Alternatively, a more accurate way to calibrate is to connect an EOM to the input to generate sidebands at a known frequency. The value of 0 frequency offset is assigned

to the beginning of the resonance.

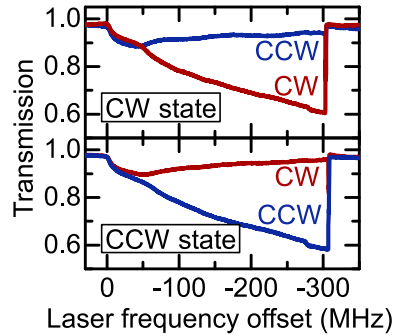


Figure 3.13: *One of the first observed instances of symmetry breaking. The transmitted power through the tapered fibre in both directions is plotted as a function of the laser frequency for two consecutive scans. Adapted from [87].*

Clearly, one of the two directions is coupling in the resonator, therefore the transmission reduces, while the other almost doesn't couple in. The light in both directions comes from the same laser, so the detuning is the same in both direction and the power is roughly the same. However, the amount of power coupled into the resonator in both directions is significantly different. Furthermore, the direction that couples into the resonator is apparently random when the power in the two directions is equal.

The observed effect is called spontaneous symmetry breaking. It describes a system where the equations of motion show a particular symmetry but the state of the system violates that symmetry. In this case, the symmetry is the chirality. In other words the system is exactly the same for both circulation directions: light entering the tapered fibre in either direction has the same polarization, power and frequency. However, in a specific range of detuning and powers, the light circulates in the resonator just in one direction.

This behaviour is present in many fields of physics, from superconductivity to ferromagnetism, including also the Higgs mechanism [46]. One of the most intuitive and popular representations is the so-called “Mexican hat” potential shown in Section 3.4. It can be imagined as a rigid well holding a ball subject to gravity oriented towards the bottom of the page. The potential is symmetric in each case, however, in panel (a) the system will stay in the position $x = 0$, the ground state of the system. In the next panel (b) the state $x = 0$ is still the ground state but it is now ill-defined being an indifferent equilibrium. In panel (c), $x = 0$ is a point of

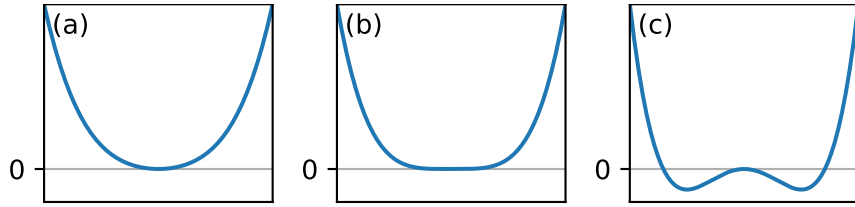


Figure 3.14: *An example of a tunable potential that leads to spontaneous symmetry breaking. (a) the potential has a single minimum at the point of symmetry with positive second derivative. The ground state is the bottom of the well. (b) There still a single minimum but the second derivative is 0. This is the limit situation before symmetry breaking. (c) The potential is still symmetric and the point of symmetry is a stationary point. However, there are now two possible ground states, each of them does not follow the same symmetry as the potential.*

unstable equilibrium. What is more important is that there are lower energy states at $x > 0$ or $x < 0$. Under a minimum perturbation, the system will choose one of them and, despite the fact that the potential is symmetric around $x = 0$, the ground state is not. Since the gravitational potential of an object is proportional to the height of that object it is very useful for creating a simple mental picture. However, the potential in Section 3.4 can represent any kind of potential that exhibits symmetry-breaking behaviour.

To be fair, in a mathematical world the ball will stay in the centre of the potential indefinitely, but in the real world, there is always noise that will perturb the system out of unstable equilibrium. In the specific case of this thesis, we can imagine the x axis in Section 3.4 as the power imbalance between the two circulating directions. The evolution through panels (a) to (c) correspond to the increase of input power of detuning.

A first step to verify the theory we developed is to test how the symmetry breaking and the amplification of the power imbalance behave with power. The experimental data in Fig. 3.15 (a) show how the coupled power in each direction is roughly the same at low power. As the power increases, the difference between p in the two directions is amplified. This enhancement is greater at intermediate detunings and tends to reduce as the detuning approaches the point of jumping out of resonance. The data in Fig. 3.15 are measured (a) and calculated (b) with a power imbalance of 10%, i.e. the input power is 10% higher in the CW direction to prevent random switching and simplify the data analysis.

The scaling of the frequency axis and the fit of experimental data deserve a

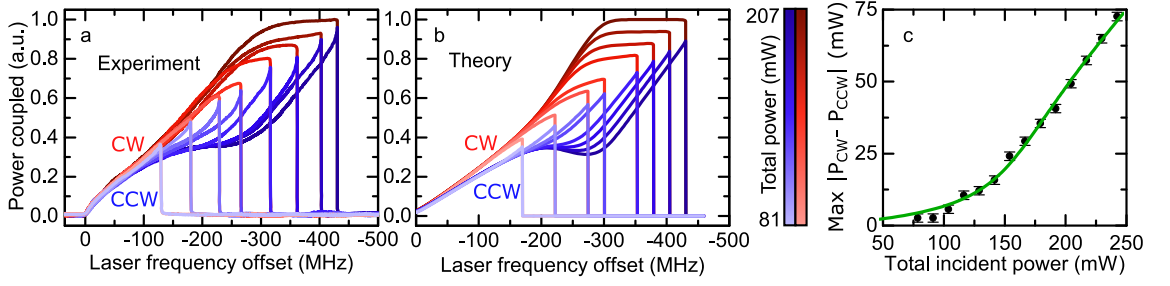


Figure 3.15: (a) *Experiment* and (b) *simulation* of the coupled power in the resonator as a function of the laser frequency. The colour red and blue correspond to the direction of light and the brightness of the trace indicate the input power. In both (a) and (b) the input power is 10% higher in the CW direction to prevent random switching. (c) The maximum difference between the power coupled in the two directions. The black dots are calculated from the measurements in (a) and the green line is the theoretical prediction. Adapted from [87].

detailed description. The first step is to measure the characteristic power P_0 and the resonance half-linewidth γ as described in Section 3.4.1. This defines the scale of the vertical axis, however the horizontal axis requires an additional step. As mentioned before, the thermal effect is not included in the theory but it can be implemented as a detuning dependent on the total power as follows.

$$p_{1,2} = \frac{\tilde{p}_{1,2}}{1 + (\delta_{1,2} + (1 + T)p_{1,2} + (2 + T)p_{2,1})^2}. \quad (3.45)$$

The parameter T does not distinguish the direction of propagation and is used as a free parameter in the fit. In practice the presence of T only has the effect of rescaling the horizontal axis.

Input powers balance

The method for balancing the input power in the two directions requires a few words. What matters for the symmetry breaking direction is the input power at the coupling point, however, this cannot be measured directly. The condition of equal power in both directions at the coupling point can be inferred by ensuring that the resonator randomly picks the circulating direction. However, the coupled power can be influenced by other factors such as the polarisation. The resonator acts like a polariser and each mode has one of the two orthogonal linear polarisations. The polarisation of the input light can be aligned to the mode by using a polarisation controller and checking both that the transmission dip is maximised in the resonance of interest and, simultaneously, all the resonances with perpendicular

polarisation are cancelled. Once this operation is performed I can assume that the input power is the same. I then record the photodiodes voltage out of resonance in both directions, corrected for the offset voltage measured with no laser input. This voltage corresponds to equal input power in both directions. This holds true for several minutes. The main drift is caused by polarization drift that has multiple sources. Moving the fibres change their curvature radius and the temperature affects the length. Both these effects modify the birefringence of the fibre, hence the polarisation state reaching the microresonator. To minimise this effect we work in a thermally controlled lab and we tape all the optical fibres to the table to prevent them from moving. Changes in the EDFA power also affect the polarization, hence the EDFA is always set at the maximum power of interest and the power is controlled with variable attenuators. The calibration of the photodiodes is verified before and after every measurement to prevent systematic errors.

The method described above also corrects for the different losses that may be present on each side of the tapered fibre with respect to the resonator. These losses cannot be measured from the taper connectors. Also, the two photodiodes may have slightly different sensitivity and the losses in the optical circuit that leads to the photodiodes may be different. But since we are normalising the measured voltage to the value for which we observe equally probable switching all these factors are accounted for.

Once the photodiodes are calibrated, it is possible to induce a specific imbalance in the input power as in the case of Fig. 3.15.

3.4.1 Measuring the resonator parameters

The simulations in Fig. 3.15 (b) are calculated for the same parameters of the experiment.

Power imbalance

The power imbalance is measured from the transmitted power of the tapered fibre out of resonance. The photodiodes are first calibrated by scaling the output voltage measuring to a power meter (Thorlabs PM20CH) reading for the same optical power.

Half linewidth and Q-factor

The half linewidth of the resonance γ can be measured at very low power, where the thermal and Kerr effect are negligible, by scanning the laser through the resonance; this also allows calculating the Q from Eq. (2.64) since the laser driver indicates the wavelength. The intrinsic Q-factor Q_0 cannot be measured directly because it requires the condition of no coupling between the taper and the resonator. There are however two techniques that provide very accurate estimates both through the measure of the linewidth 2γ . First, it is possible to measure Q for critical coupling and double that value since $\gamma_{\text{crit}} = 2\gamma_0$ (see Eq. (2.46)). Alternatively, the taper can be moved away from the resonator to reduce the coupling efficiency η at or below 5 %, depending on the noise of the photodiode. For such a low coupling $Q \simeq Q_0$.

Characteristic power

The last free parameter in the theory is the characteristic power P_0 . This could be calculated knowing the characteristics of the material but some of the quantities involved have a very large error. The biggest source of error is the mode area; it cannot be measured directly and can only be estimated from the geometry of the resonator through a Comsol Multiphysics simulation. One of the approaches is to use P_0 as a free parameter and fit it by measuring the variation of the maximum power imbalance with the input power (cf. Fig. 3.15 (c)).

There are, however, a few techniques that allow estimating P_0 . The most immediate method is to slowly increase the input power until the symmetry breaking is observed. The power where this happens corresponds to $1.54 P_0$. The drawback of this method is that, if there is a power imbalance between the two directions this may be amplified in the vicinity of the symmetry breaking condition and be misinterpreted as symmetry breaking. Checking that the resonator picks a random state each time helps to avoid the confusion.

We saw in Fig. 3.8 that the shape of the bubble changes with the input power. In particular the difference in the shape is very pronounced between $\tilde{p} = 1.5$ and $\tilde{p} = 3$. It is possible to compare the observed shape with the theoretical one to determine the ballpark of \tilde{p} . Note however that, especially at higher power, the thermal effect distorts the bubble.

At high input power the most reliable method to determine \tilde{p} is to use the

property that we found above: when one direction is fully coupled, e.g. $p_1 = \tilde{p}$, the other direction has a coupling of $p_2 = 1/\tilde{p}$. Hence it is possible to estimate the input power from the ratio between the two:

$$\tilde{p} = \sqrt{\frac{p_1}{p_2}}. \quad (3.46)$$

In the same time-frame as this experiment, another group observed the same effect in a microresonator with strong backscattering. In their case the system was not symmetric at the beginning because they were pumping the resonator in just one direction. However, the scattering inside the resonator transfers power from the stronger direction to the weaker until the counter-propagating powers are balanced [123].

Chapter 4

Microresonator-based implementation of isolators and circulators

In the previous chapter, I discussed how the light in the resonator randomly picks a circulating direction when the intensity or the detuning reaches the symmetry breaking threshold value. The first application that comes to mind for a device allowing unidirectional light circulation is to make an optical isolator as illustrated in Fig. 4.1.

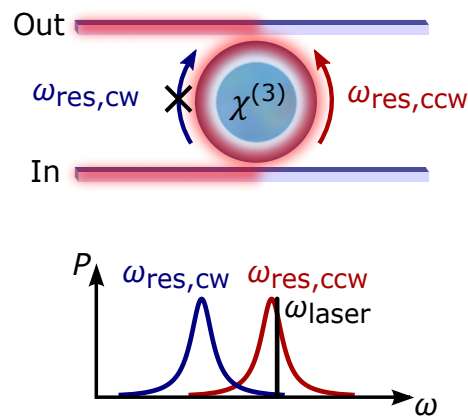


Figure 4.1: Scheme of the idea behind the isolator: once the symmetry is broken, light of a given frequency can circulate just in one direction in the resonator. It would be out of resonance in the other direction. Adapted from [51].

However, a random choice in the direction of propagation is not the best selling characteristic for an isolator. Fortunately, the resonator shows this randomness only when pumped symmetrically in both directions. If the inputs are imbalanced, the

direction that couples into the resonator is always the one with the highest input power. Once the resonator is set in one direction, it shows a certain amount of hysteresis, i.e. it resists the changes in circulating direction. I will discuss the hysteresis in the next chapter. In the case of an isolator, the input laser is likely to be the strongest input. However, to ensure that the direction of working will not change during operation, the light reflected back into the resonator has to never exceed the power at the input. This is always the case for linear and passive optical circuits but could not hold true if the optics after the isolator comprise amplifiers or something that causes a wavelength shift.

Once reassured that the propagating direction coupling into the resonator is the one with the highest input power, to make an isolator, we would like to take advantage of the non-reciprocity by accessing the light from the forward direction (defined by the input laser) but preventing light in the opposite direction from reaching the laser itself. This cannot be achieved with a single tapered fibre because the end of the fibre opposite to the input laser behaves in exactly the opposite way: any input at the same frequency of the laser cannot couple to the resonator because it sees a Kerr shifted resonance. At the same time, most of the light from the laser goes into the resonator and not to the other end of the taper. To realise an isolator we need a way of extracting the light from the resonator and the easiest way to do so is to introduce an additional taper that couples light out from the other side of the resonator as shown in Fig. 4.1.

Before analysing in detail how to realise a microresonator-based isolator let us discuss the current technology for isolation, a clear definition of isolation and the alternatives that exist for miniaturisation.

4.0.1 The Faraday isolator

Nowadays the main way of realising optical isolators is to exploit the Faraday effect [124, Chapter 6], which consist of a phase shift between the two circular polarisation components of light propagating through a medium in presence of a magnetic field. In case of linearly polarised light, this corresponds to a rotation of the polarisation axis in the direction defined by the magnetic field. In the simple case of propagation

in the same direction of the magnetic field B the rotation θ can be expressed as:

$$\theta = \nu BL \tag{4.1}$$

where ν is the Verdet constant of the material that is not really a constant but depends on the wavelength of the light, while L is the length of the medium in the magnetic field. An isolator based on this effect consists of a Faraday rotator designed to produce a rotation of 45° for the wavelength of interest sandwiched between 2 polarisers oriented 45° away from each other. This way any light in the forward direction that passes through the input polarizer will also go through the output one because the polarisers orientations are matched. While any light travelling in the return direction will be first filtered by the output polariser into linear polarisation, and then rotated by 45° such that it reaches the input polariser with perpendicular polarisation, thus it is completely blocked.

Commercial free space polarisers typically work in a range of a few percent change in λ around the design wavelength with input loss of 1 dB or less and isolation of about 30 dB. Unfortunately, they also weight up to 1 kg and they are surrounded by a strong magnetic field¹. Optical isolators exist also in fibre-coupled form factor. They come as metal rods with the size of a pen cap² with slightly lower performances of about 2 dB insertion loss and 25 dB isolation.

Getting to smaller dimensions is problematic because of the nature of the effect used: magnets generally produce a magnetic field that is proportional to their volume. Looking back at Eq. (4.1) it is clear how the polarisation rotation decreases as the fourth power of the size: the volume of the magnet decreases as L^3 and the interaction length as L .

4.0.2 What is an isolator?

The Faraday isolator is commonly accepted to be an isolator. But different technologies for non-reciprocal light propagation have different requirements and behave differently so, before introducing the various alternatives, it is worth dwelling on the definition of what is an isolator.

Wave propagation is assumed to be reciprocal [125] and that is generally true.

¹I had the screwdriver or tweezers ripped off my fingers while trying to do precision work near them a few times.

²about 8 mm \varnothing \times 40 mm if you are a reader from the future and have never seen a pen.

If light propagates in one direction in a system it can propagate backwards. There are plenty of practical examples around us. A lens concentrates the parallel sunlight on a tiny ant and, in the opposite direction, collimates the light of a tiny LED into a parallel beam. However, there are cases where this is not true and these are generally called isolators.

Are Venetian blinds an isolator? In brief, they prevent the sunlight from entering a room, but a light in the room ceiling will shine on the pavement outside. The answer is no, the Venetian blind only limits the angle at which light can pass through it. A test that an isolator should pass is time reversal, which in the case of light corresponds to inverting the direction of propagation. A person laying down on the front porch can still see the light bulb inside and any any light pointed at the sun from inside will not leave the room. In the case of the Faraday isolator, light cannot travel backwards through it and the same is true for the microresonator-based isolator presented in this chapter.

The definition of “isolator” is very debated in the field of optics and there have been attempts to summarise it. The origin of this debate is that for some applications not all the requirements of a proper isolator need to be fulfilled for the specific case (as in the example of the Venetian blind illustrated earlier). Unfortunately, this has stretched the isolator blanket a bit too much, producing (in-)famous retractions and corrections such in the cases discussed below. To avoid to see my research invalidated in such way, I rely on a very clear definition of isolator by Jalas et al. [126]. In particular, they state that an isolator has to have at least 2 ports that can sustain one or more optical modes. The scattering matrix of the isolator needs to be non-symmetric, which involves breaking the Lorentz reciprocity. There has to be at least a linear combination of modes that is transmitted from port 1 to port 2. Also, **any** combination of modes has to be blocked from port 2 to port 1.

This second part is critical because it is relatively easy to create an interface in a multimode waveguide that couples a single mode in the forward direction into a combination of modes, and that can prevent a single mode in the backwards direction from continuing [127]. However, under time reversal, i.e. if the same combination of modes, with the same amplitude and phase relation, travels backwards it will couple back into the original mode.

As another example, the device presented in [128] uses the thermal shift introduced in Chapter 2 to tune two resonators used as filters in resonance with each

other. Light in the forward direction redshifts the resonance frequency of the input resonator and matches it with the output one. Light from the output would shift the output resonator away from the input one. Unfortunately, when the device is open in the forward direction it also allows light to travel backwards making a very poor isolator in real-life conditions as proven by [129].

4.0.3 Miniaturising isolators

Lorentz reciprocity can be broken by several effects, mainly magnetic field and non-linearity. All these effects are neglected in the derivation of Lorentz reciprocity from the Maxwell equations, hence if one of them is introduced the theorem does not hold any more [126].

Integrating the Faraday effect

At a closer look, the situation is not so dramatic for miniaturised Faraday isolators. To begin with, moving from free space propagation to waveguides confines the light in a much thinner region hence the magnetic field source can be moved closer to the light [130, 131]. A common solution is also to increase the path length of light in the magnetic field by folding the optical path or using a resonator [132, 133, 134]. Also, electromagnets become a viable source of magnetic field given the very confined region [135, 134]. The drawback of these solutions is that integrating magnetic materials requires complex fabrication processes. Alternatively, in the case of electromagnets, the integration is easily achieved with common fabrication methods but the resulting device requires electrical power to work.

Nonlinearity

The magnetic field is not the only way to break the Lorentz nonreciprocity. The derivation of the theorem is based on a linear response to the field so any kind of directional nonlinearity can be exploited to realise an isolator. There are plenty of methods to achieve nonlinearity, what follows is a non-exhaustive list of methods that proved to be successful in the field of isolation. Second-harmonic generation (SHG) [136] is a second-order nonlinearity while the Kerr nonlinearity is a third order one. Optomechanical coupling is often nonlinear and several paths to non-reciprocal light propagation have been demonstrated [137, 138, 139, 140, 141]. A similar

approach can be found in [142, 143], but parity-time-symmetry is broken with the use of gain and multiple resonators again forfeit the advantages of a passive device and requiring a complex tuning of coupling between waveguides and resonators. To mention a few other sources of nonlinear response, it is worth citing the introduction of photonic bands [144, 145] or the use of stimulated Brillouin scattering [146, 147].

The microresonator approach

The proposed Kerr-induced nonreciprocity is a form of nonlinearity. In this specific case, it is the resonance frequency difference between the two circulating directions that depend on the circulating power in each direction. The following sections of this chapter describe the theoretical model of a resonator coupled to two waveguides and a simulation of the expected response of the microresonator-based isolator. Particular focus will be on the optimisation of the isolation and the transmission of the device. Then I report on the experimental setup used to test this idea and discuss the results both for an isolator configuration and circulator configuration. Finally, the integration aspects of this technology are considered and compared to the alternatives highlighted above.

4.1 Coupling two fibres to a microresonator

To describe the coupling to the resonator in the case of two tapered fibres we need to generalise the model described in Section 2.1.

This configuration is often called “add-drop” referring to the second taper that is used to add a wave to the resonator or extract (drop) it from the resonator in a single direction [66, 148, 149, 150]. I will use a different nomenclature since in this case, the resonator receives inputs in both directions. The bottom fibre in Fig. 4.2 is the input taper since, without loss of generality, we can decide that the input to the isolator is going to be port 1. The tapered fibre on the opposite side of the resonator is consequently the output taper. Similarly to Chapters 2 and 3, the coupling is treated linearly. The nonlinearity is added to the model as a resonance frequency shift governed by the Kerr effect.

In Fig. 4.2 I am making the same assumption of $t, k \in \mathbb{R}$. Also, I use the subscript A for the coupling point with the input fibre and B for the coupling point with the output fibre. The four ends of the fibres are called ports and they are numbered

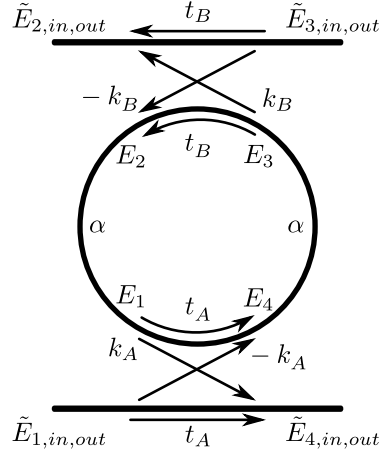


Figure 4.2: Schematic of the coupling region and the parameters used to describe the coupling of a resonator to a tapered fibre. In this chapter the input port will be the one in the bottom left of the figure.

as shown in Fig. 4.2. Port 1 is used as the input and port 2 is the output of the isolator, hence we expect optical power travelling in both directions through these ports. Ports 3 and 4 are not used in the isolator configuration so optical power will only leave the setup through these ports.

In this chapter, I use α^2 as the round trip transmission instead of α as used in Section 2.1. This allows a cleaner derivation with fewer square roots appearing. Let us first focus on the transmission in the forward direction (CCW in Fig. 4.2). The input is just at port 1 and no other light enters the setup at the moment. The field circulating inside the resonator in the steady-state can be described as the field that survives inside the resonator after a round trip, with its accumulated phase, plus the field that is added through the coupling point A.

$$E_4 = E_4 \cdot \alpha^2 t_A t_B e^{j\theta} - k_A \longrightarrow E_4 = \frac{-k_A}{1 - \alpha^2 t_A t_B e^{j\theta}} \quad (4.2)$$

$$E_3 = \frac{-k_A \alpha e^{j\phi}}{1 - \alpha^2 t_A t_B e^{j\theta}} \quad (4.3)$$

$$E_2 = \frac{-k_A \alpha t_B e^{j\phi}}{1 - \alpha^2 t_A t_B e^{j\theta}} \quad (4.4)$$

$$E_1 = \frac{-k_A \alpha^2 t_B e^{j\theta}}{1 - \alpha^2 t_A t_B e^{j\theta}} \quad (4.5)$$

All the fields are normalised to the input field $\tilde{E}_1 = 1$. The field that leaves the resonator at port 2 can be described following all the losses and phase accumulation that the intracavity field E_4 encounters before exiting the resonator:

$$\tilde{E}_2 = E_4 \cdot \alpha k_B e^{j\phi} = \frac{-k_A k_B e^{j\phi}}{1 - \alpha^2 t_A t_B e^{j\theta}} \quad (4.6)$$

Where ϕ is the phase accumulated from the coupling point A to B . This quantity is crucial if other electric fields with frequencies similar to the input one are reaching port 2 in the same direction but in this specific case, it is not really important. We can get rid of it by calculating the transmitted power from port 1 to 2. Also, let us remember the small angle approximation $\cos \theta = 1 - \theta^2/2$, as introduced in Section 2.1.1 and the following approximation:

$$|1 - B \cdot e^{j\theta}|^2 = 1 + B^2 - 2B \cos \theta \simeq 1 + B^2 - 2B(1 - \frac{\theta^2}{2}) = (1 - B)^2 + B\theta^2, \quad B \in \mathbb{R} \quad (4.7)$$

$$\tilde{P}_2 = |\tilde{E}_2|^2 = \frac{\alpha^2 k_A^2 k_B^2}{(1 - \alpha^2 t_A t_B)^2 + \alpha^2 t_A t_B \theta^2} \quad (4.8)$$

As expected it is easy to see that the transmission T is maximised for $\theta = 0$ which is the resonance condition. In this case the transmitted power can be written as:

$$\tilde{P}_{2,\text{res}} = \frac{\alpha^2 k_A^2 k_B^2}{(1 - \alpha^2 t_A t_B)^2} = T \quad (4.9)$$

We can express the transmission by substituting the definitions of κ_A , κ_B , γ_0 from Eqs. (2.45) and (2.47) as:

$$T = \frac{4\kappa_A \kappa_B}{(\gamma_0 + \kappa_A + \kappa_B)^2} \quad (4.10)$$

Remember that in this chapter the resonator transmission for the electric field in one round trip is α^2 so Eq. (2.46) now yields:

$$\gamma_0 = \left(\frac{c}{\pi d n} \right) \frac{1 - \alpha^2}{\alpha} \quad (4.11)$$

Let us keep the assumption of resonance in the forward direction for the rest of this analysis. This is justified by the fact that we want to operate the resonator in a condition of high transmission. The thermal locking will maintain this condition and compensate for small resonance shifts.

As previously done in Chapter 2, I will define the coupling efficiency for both coupling point. But in this case I will make a distinction between coupling light into the resonator and out of it. This allows me to split the transmission into two quantities, namely the in-coupling η_{in} and out-coupling efficiency η_{out} . The in-coupling efficiency is defined in analogy with Eq. (2.51) as the fraction of the input power that does not continue straight through the input taper but is instead coupled into the resonator at resonance:

$$\eta_{\text{in,A}} = \frac{P_{1,\text{in}} - P_{2,\text{out}}}{P_{1,\text{in}}} \quad (4.12)$$

We can write this as $1 - |\tilde{E}_4|^2$, since we normalised $\tilde{E}_{1,\text{in}} = 1$, obtaining:

$$\eta_{\text{in,A}} = \frac{k_A^2 (1 - \alpha^4 t_B^2)}{(1 - \alpha^2 t_A t_B)^2} \quad (4.13)$$

We can express this in the linewidth notation again in the analogy with Chapter 2 by substituting the intrinsic linewidth of the resonator with the combined linewidth of the resonator and the output taper

$$\eta_{\text{in,A}} = \frac{4\kappa_A(\gamma_0 + \kappa_B)}{(\gamma_0 + \kappa_A + \kappa_B)^2} \quad (4.14)$$

These two expressions are not exactly the same but they converge in the limit of high Q resonators ($\alpha, t \rightarrow 1$) as shown in Fig. 4.3.

We define the out-coupling efficiency such that $T = \eta_{\text{in,A}}\eta_{\text{out,B}} = \eta_{\text{in,B}}\eta_{\text{out,A}}$. In other words, the out-coupling efficiency is the fraction of power coupled into the resonator that leaves the resonator on the other side.

$$\eta_{\text{out}} = \frac{|\tilde{E}_2|^2}{1 - |\tilde{E}_4|^2}, \quad (4.15)$$

where the normalisation $\tilde{E}_{1,\text{in}} = 1$ is still in place, $|\tilde{E}_2|^2$ is described in Eq. (4.9) and we just need to square \tilde{E}_4 defined in Eq. (4.27). Wrangling the maths a bit, all the contributions from the coupling point A cancel out and we find:

$$\eta_{\text{out}} = \frac{k_B^2 \alpha^2}{1 - \alpha^4 t_B^2} \quad (4.16)$$

Or, in the linewidth notation:

$$\eta_{\text{out}} = \frac{\kappa_B}{\gamma_0 + \kappa_B} \quad (4.17)$$

Again, the two definitions converge in the limit $\alpha, t \rightarrow 1$, however the transmission T consisting of the product of the two coupling efficiencies is exactly the same in both cases for every value of the parameters. Figure 4.3 shows a comparison between the exact picture and the approximation of the measurable parameters.

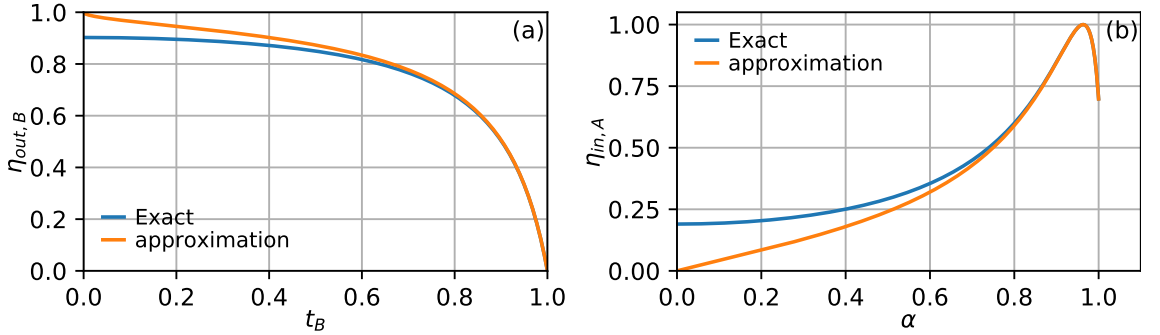


Figure 4.3: (a) Plot of $\eta_{\text{out},B}$ as a function of t_B for the value of $\alpha = 0.95$. (b) Plot of $\eta_{\text{in},A}$ as a function of α for $t_A = 0.9$ and $t_A = 0.97$. The exact value from the alpha model is plotted in blue, the approximated model is in orange. Note that the two models diverge just when one of t_A, t_B, α are significantly less than 1.

Note how the two models diverge only when the parameters significantly differ from 1, but let us remember that for the resonators used in this thesis α is of the order of 0.9999 or $(1 - 10^{-4})$ and t_A, t_B are of similar magnitude. Indeed, to highlight the differences, the graphs are plotted for an unrealistically low Q-factor resonator in (a) or unrealistically strong coupling (b). Note that in panel (b) the incoupling efficiency reaches 1 when the condition of critical coupling (Eq. (4.28)) is achieved and is less than 1 otherwise.

Introducing reflected light

So far our isolator model has had an easy life: no light is coming back from port 2 in the attempt to damage or just perturb the fragile laser connected to port 1. Let us now introduce a reflection at port 2 to test the isolation of the device. We will work under the assumption that the reflected light has an intensity always lower than or equal to the output. This is an important difference compared to the other kinds of isolators as discussed later.

To describe the light propagation in the backwards direction we will use the coupling efficiency picture because it is easier to relate to the experimental measures. Let me recall Eq. (3.30) describing the Kerr induced symmetry breaking but this time I am keeping the coupling efficiency explicit since I am going to use it in the model. The light circulating in the resonator can be expressed as:

$$p_{CCW} = \frac{\eta_A^{\text{in}} \tilde{p}_{CCW}}{1 + (\delta + p_{CCW} + 2p_{CW})^2} \quad (4.18)$$

$$p_{CW} = \frac{\eta_B^{\text{in}} \tilde{p}_{CW}}{1 + (\delta + p_{CW} + 2p_{CCW})^2} \quad (4.19)$$

Where η_A^{in} is defined in Eq. (4.14), δ is the laser detuning from the resonance Δ normalised as usual by the half linewidth γ , p_{CCW} and p_{CW} are the coupled powers in each direction normalised as

$$p = \frac{2\pi}{\mathcal{F}} \frac{P_{\text{circ}}}{P_0}, \quad (4.20)$$

and the input powers into port 1 and 2 respectively are now normalised just by the characteristic power,

$$\tilde{p} = \frac{\tilde{P}}{P_0}, \quad (4.21)$$

. while the appropriate η_{in} for each direction is explicitly written in the equation.

We can assume that the cavity is locked in resonance in the forward direction by the thermal effect ($\delta = -p_{CCW} - 2p_{CW}$) hence the equations above become:

$$p_{CCW} = \eta_A^{\text{in}} \tilde{p}_{CCW} \quad (4.22)$$

$$p_{CW} = \frac{\eta_B^{\text{in}} \tilde{p}_{CW}}{1 + (p_{CCW} - p_{CW})^2} \quad (4.23)$$

So far we assumed ideal optical fibres. However, to use this model to fit experimental data, we need to account for the losses of the tapered fibres and the amount of reflections at port 2. We define the power transmission of each tapered fibre as $T_{A,B}^2$, i.e. we will assume that each half of the fibre has a transmission $T_{A,B}$. Introducing this in Eqs. (4.22) and (4.23):

$$p_{CCW}^{\text{out}} = \eta_B^{\text{out}} T_B p_{CCW} = T_A T_B \eta_A^{\text{in}} \eta_B^{\text{out}} p_{CCW}^{\text{in}} \quad (4.24)$$

Defining the reflections in the same linear polarisation at the output port as R , the power circulating in the CW direction is:

$$p_{\text{CW}} = p_{\text{CCW}}^{\text{out}} R T_B \frac{\eta_B^{\text{in}}}{1 + (p_{\text{CCW}} - p_{\text{CW}})^2} \quad (4.25)$$

This a cubic equation in p_{CW} that has an analytical solution, however the explicit expression easily fills half a page, so we will keep it implicit. The power reaching back to port 1 is:

$$p_{\text{CCW}}^{\text{back}} = \eta_A^{\text{out}} T_A \times p_{\text{CW}} \quad (4.26)$$

4.2 Isolator

We now have all the elements to describe the isolator. Before moving to the experiment let me discuss what are the coupling parameters to extract the best performances from this device and why there is a trade-off between isolation and insertion losses.

4.2.1 Optimising the parameters

Let us now focus on optimising the isolator characteristics, specifically the transmission in the forward direction and the extinction, or isolation, in the backwards direction. First, we will focus on maximising the transmission through the resonator. We already discussed tuning the laser to the resonant condition, a further step is to ensure critical coupling at the input. To calculate this condition we require no power to be transmitted to port 4. The field at port 4 is the field transmitted through the taper plus the field leaking from the resonator (that has the opposite phase at resonance, represented by the minus sign that naturally arises from the model):

$$\tilde{E}_{\text{out}} = t_A + E_1 k_A = t_A + E_4 \alpha^2 t_B k_A = t_A - \frac{-k_A^2 \alpha^2 t_B}{1 - \alpha^2 t_A t_B} = \frac{t_A - \alpha^2 t_B}{1 - \alpha^2 t_A t_B} \quad (4.27)$$

So the condition for critical coupling at the input of the resonator is:

$$t_A = \alpha^2 t_B \quad (4.28)$$

This is analogous to the condition found for a single taper: the coupling losses should match the losses in the rest of the resonator. From the point of view A, it makes no difference if the losses come from the intrinsic losses or from an additional coupling point. Let us rewrite the transmitted power under this condition.

$$\tilde{P}_{2,\text{res,crit}} = \frac{\alpha^2 k_B^2}{1 - \alpha^4 t_B^2} = \frac{\alpha^2 (1 - t_B^2)}{1 - \alpha^4 t_B^2} = \frac{\alpha^2 k_B^2}{1 - \alpha^4 (1 - k_B^2)} \quad (4.29)$$

From the plot of this equation in Fig. 4.4 we can see that for $k_B = 0$, obviously no power is coupled out of the resonator. The maximum transmission is achieved for $k_B = 1$ which corresponds to coupling everything out the resonator and it is limited by the power transmission of half resonator α^2 . Unfortunately this second condition is also unreasonable: given the condition of critical coupling at the input, choosing $k_B = 1$ also implies $k_A = 1$. This represents more a fibre bent back than something deserving the name of resonator. This is especially true for a nonlinear isolator that requires a high intensity to work at its best. Let's consider the intracavity power. For $\alpha, t_A, t_B \sim 1$ the power is roughly the same in any point of the resonator. If the round trip losses or coupling losses are significant the power will be different in the various point. We can arbitrarily take the already calculated E_1 that corresponds to the point of lowest power in the CCW direction since the circulating field experienced all the losses and has yet to reach the coupling point where more power is added.

$$P_{1,\text{res}} = \frac{\alpha^4 k_A^2 t_B^2}{(1 - \alpha^2 t_B t_A)^2} \quad (4.30)$$

For critical coupling at the input this becomes:

$$P_{1,\text{res,crit}} = \frac{\alpha^4 t_B^2}{1 - \alpha^4 t_B^2} \quad (4.31)$$

As we suspected this value miserably falls to 0 for the ideal transmission case. Instead, it shoots up to a maximum of:

$$\max(P_{1,\text{res,crit}}) = P_{1,\text{res,crit}} \Big|_{k_B=0} = \frac{\alpha^4}{1 - \alpha^4} \quad (4.32)$$

but this value corresponds to removing the second taper, so again not very useful.

Figure Fig. 4.4 shows the intracavity power and the transmitted power as a function of the coupling k_B . The two extremes are unrealistic for a practical device,

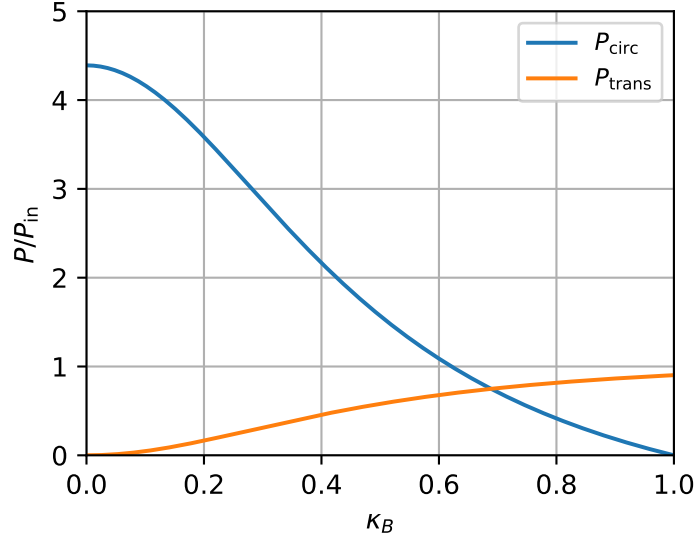


Figure 4.4: Plot of the circulating power P_1 in blue and the transmitted power $\tilde{P}_{2,\text{out}}$ in orange, for the conditions of resonance and critical coupling at the input $\kappa_A = \gamma_0 + \kappa_B$ and for resonator losses of $\alpha = 0.95$.

but there is space for compromise especially for $\alpha \sim 1$ i.e. high Q-factor resonators. The other key parameter is the isolation. In our configuration we can define it as the amount of power emitted by the laser that reaches back into the laser itself:

$$I = \frac{P_{\text{back}}}{P_{\text{in,ccw}}} \quad (4.33)$$

The isolation I can be calculated by using Eq. (4.26) for the power returning back into the isolator. A mathematical analysis of this parameter would require solving Eq. (4.26), however, we can provide some physical considerations on how to maximise isolation. The transmission through the resonator $T = \eta_A^{\text{in}} \eta_B^{\text{out}}$ appears twice in the equations, together with the fibre losses and the reflections at the output: all these parameters contribute to reducing the power going back to the laser but also reducing the power reaching the output. Hence we would like this to stay as low as possible for a real-life application. The important contribution is the power circulating in each direction in the denominator of Eq. (4.25). This describes the Kerr resonance splitting between the two directions that is the foundation of this approach. To increase isolation we would like to maximise the circulating power in the forward direction P_{CCW} and minimise the one in the backwards direction P_{CW} .

The tunable parameters are the incoupling efficiency, that can be measured through the photodiode at the end of the first fibre; the outcoupling efficiency, that can be measured from T at the transmission photodiode, and η_A^{in} .

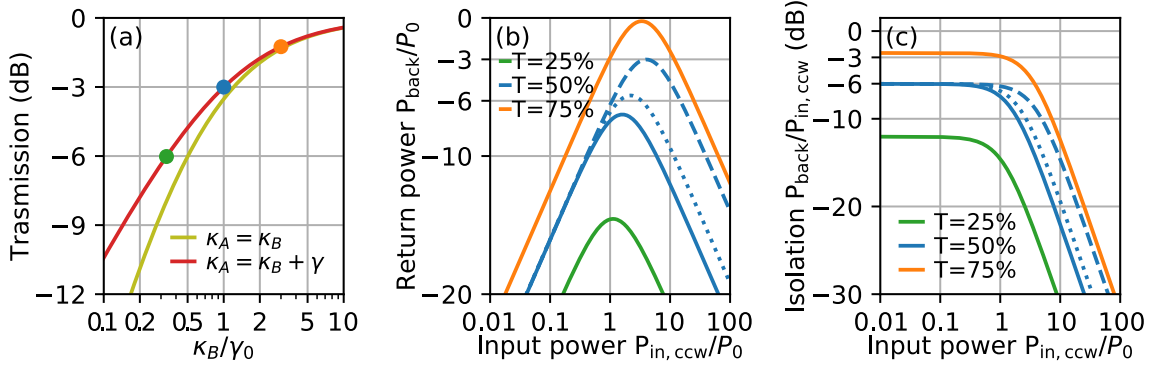


Figure 4.5: (a) Simulation of the transmission through the isolator in the condition of equal coupling (yellow) and critical coupling at the input (red) (higher is better). All the coupling strengths are normalised to $\gamma_0 = 1$. (b-c) Return power to the input and isolation as a function of the input power for different transmissions (lower is better). The continuous curves are obtained for $T = 25\% \rightarrow \kappa_A = \frac{4}{3}, \kappa_B = \frac{1}{3}$; $T = 50\% \rightarrow \kappa_A = 2, \kappa_B = 1$; $T = 75\% \rightarrow \kappa_A = 4, \kappa_B = 3$. The dotted line represents $T = 50\%$ with equal coupling ($\kappa_A = \kappa_B = 1.21$). The dashed line represents $T = 50\%$ with critical coupling at the output ($\kappa_B = 2, \kappa_A = 1$).

In Fig. 4.5 (a) we analyse the transmission as a function of the coupling constants. The coupling linewidth κ_A and κ_B , are expressed in units of γ_0 . Also, instead of considering the two variables κ_A and κ_B independently we impose two different conditions between them and vary independently only κ_B . The case of equal coupling on both sides is plotted in yellow and the case of critical coupling on the input side is plotted in red. As discussed above, we can see that for low coupling the transmission is really low. The two curves differ in this region because in the yellow curve both κ become small, while in the red curve κ_A never goes below γ_0 . As discussed before the best transmission is achieved for κ_A and κ_B of the order of the intrinsic linewidth or greater. However, high coupling reduces the loaded Q-factor and the circulating power hence the isolation.

Figure 4.5 (b) shows the power returning to the laser as a function of the input power for 3 values of transmission highlighted in panel (a). The input power is normalised to the value of P_0 for the resonator with no coupling³ and perfect fibres and mirrors are assumed. It is interesting to note how different values of the two coupling constants make it possible to achieve the same transmission but produce different values of isolation. All the blue curves correspond to a transmission of 50% but they are obtained with different combinations of coupling. The continuous lines

³The expression of P_0 depends on the loaded Q , therefore it changes with changing coupling

correspond to critical coupling at the input:

$$\kappa_A = \gamma_0 + \kappa_B, \quad \kappa_B = \gamma_0 \quad (4.34)$$

where all the power is transferred into the resonator in the desired direction while the output is under-coupled. This means out-coupling less light to the output, but at the same time maintaining more power circulating in the resonator that splits the resonances more and produces better isolation.

The dashed line is for critical coupling at the output:

$$\kappa_A = \gamma_0, \quad \kappa_B = \gamma_0 + \kappa_A \quad (4.35)$$

An under-coupling of the resonator on the input side means that less of the forward direction light, the one responsible for splitting the resonances is coupled into the resonator. The isolation kicks in at higher power and consequently, the maximum power reaching the input is higher.

The dotted line represents the case of equal coupling on both sides:

$$\kappa_A = \kappa_B = 1.21 \gamma_0 \quad (4.36)$$

This configuration is not as good as critical coupling at the input.

The same data are presented in panel (c) that shows the isolation. It is clearer how at low power, well below P_0 , the only isolation is provided by the losses through the resonator. For powers above P_0 instead the Kerr non-reciprocity kicks in and the isolation improves with the input power.

Panels (b,c) also show that the threshold power at which the isolator starts working is higher for higher transmission. This arises from the equations and can be intuitively explained in two ways. The increased coupling lowers the loaded Q-factor the increase the characteristic power to observe symmetry breaking effects (cf. Eqs. (3.24) and (3.26)). Alternatively, the linewidth of the resonator is larger, thus a larger Kerr shift is needed to remove the overlap between the two and larger Kerr shift requires more circulating power. Again the trade-off situation between isolation and transmission is highlighted.

Figure 4.5 and Eqs. (4.29) and (4.33) also give a general rule that, for equal transmission, is better to have more coupling at the input and less coupling at the

output to achieve better isolation. The actual optimal value for isolation for each transmission value is not exactly critical coupling at the input. However, numerical calculations show that only a marginal gain in isolation can be obtained, and this small improvement requires a control of the coupling parameters that is beyond the experimental accuracy. Hence, the condition in Eq. (4.34) represents a simple approximation that is still valid.

4.2.2 Methods

The experimental demonstration of non-reciprocal light propagation was realised one year later than the symmetry breaking. Initially, I was able to fabricate microresonators reaching Q-factors of the order of 10^8 just for diameter larger than 2 or 3 mm. In the meantime, the fabrication of silica-rods resonators has improved: at the time of this experiment I had increased the Q-factor 2 fold and extended the diameter range in which that Q-factor is achieved, down to 0.5 mm. However, for this experiment the diameter is limited by the need to couple two tapered fibres simultaneously hence a 1 mm diameter resonator is used with an intrinsic Q-factor of 1.5×10^8 .

The optical setup is shown in Fig. 4.6. The input laser was an amplified ECDL

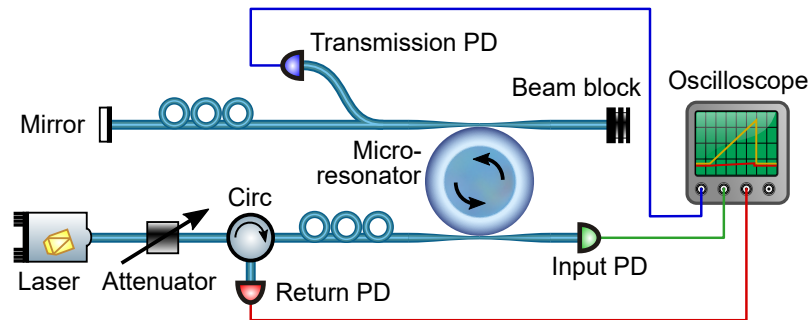


Figure 4.6: *Optical setup for the isolator experiment. Adapted from [51].*

emitting at 1550 nm. An attenuator allowed testing the isolator at different input powers avoiding changes in the current of the laser amplifier, that may cause a slow polarisation drift of the amplifier itself. The light that would go back into the laser was redirected to a photodiode labelled as “return” by an optical circulator to measure the return power P^{back} . The input photodiode at the other end of the input taper was used to measure the incoupling efficiency η_{in} and to tune the laser near the resonance frequency where the passive thermal locking stabilised the resonator.

At the output of the other tapered fibre, a directional coupler sampled 1% of the light to be measured by the transmission photodiode while most of the power was back-reflected by a fibre mirror. The two polarization controllers in the setup were used to maximise the transmission and the return through the resonator.

This configuration is designed to test the worst-case scenario for an isolator. First, there is an almost complete reflection on the output branch of our isolator; the exact reflection value cannot be measured directly without adding the additional losses of a circulator but it can be estimated around 95% in power, since the directional coupler taps 1% two times and the optical losses of the other components sum up to a few percent. Also, the polarisation of the reflected light matches the one of the resonator since the output polarizer is adjusted to maximise the power on the return photodiode.

Photodiode calibration and error

Most of the results of this experiment are ratios between powers measured by different photodiodes, hence their calibration becomes important. The photodiodes are assumed to have a linear response, i.e. they output a voltage proportional to the power they are illuminated with, however, the constant of proportionality is different for each photodiode.

I calibrated the photodiodes by setting the amplifier to different currents, measuring the voltages on the photodiodes and then disconnecting the fibre from the photodiode and measuring the power with a power meter (Thorlabs PM20CH). The photodiodes used in the experiment are free space photodiodes with an FC-APC adapter. The sensitive area is very small, less than 1 mm^2 to maintain a high bandwidth, hence every time the fibre is disconnected and reconnected to the photodiode the sensitivity (V/W) is slightly different. Also, the photodiodes are working in a high dynamic range and the electrical noise affects the measurement, in particular at low power. The error on the measures is estimated as $10\% + 0.1\text{ mW}^4$ and it is propagated linearly.

⁴The photodiodes are connected to the setup via 20 dB attenuators. Since the output of a photodiodes is 1 V per 100 μW , hence a 10 mV noise corresponds to 0.1 mW.

Fitting the data

The experimental data are fitted with the theory developed in Section 4.1. It is useful to rearrange the expression for the characteristic power P_0 (cf. Eqs. (3.24) and (3.26)) such that all the variables that cannot be measured accurately are isolated in a parameter C .

$$P_0 = \frac{\pi^2 n_0^2 d A_{\text{eff}}}{n_2 \lambda Q_L Q_0} = \frac{C}{\lambda Q_L Q_0} \quad \text{where} \quad C = \frac{\pi^2 n_0^2 d A_{\text{eff}}}{n_2} \quad (4.37)$$

By doing so I can use C as a fitting parameter for our model using an estimate as starting point.

The other parameters used in the fit are the coupling and intrinsic linewidth (κ_A , κ_B and γ_0), and the transmission of the two tapered fibres (T_A and T_B). γ_0 and the intrinsic Q-factor are measured by removing both tapered fibres from the resonator and then placing just one taper in a very undercoupled condition so that $Q \simeq Q_0$ and $\gamma \simeq \gamma_0$. κ_A is derived from the measure of $\eta_{\text{in,A}}$ using the input photodiode, while κ_B is calculated from the transmission. The transmission of the tapered fibres is measured with a power meter independently. Apart from C that is not constrained, all the other parameters are left free to change in a small range around the measured value.

All the three parameters shown in Fig. 4.7 (a,b) are fitted simultaneously, Meaning that the fit parameters are the same for all the 3 curves and the fitting algorithm attempts to minimise the sum of the three χ^2 .

4.2.3 Results and discussion

Figure 4.7(a) is measured by setting different power inputs to the isolator, scanning the laser frequency across the resonance and sampling the voltage of all the photodiodes at the moment of resonance. The working condition of the isolator would be different, with the resonator locked to the laser thanks to the thermal effect. This measurement technique removes the uncertainty due to the fluctuation of the locking point.

The return power for varying input powers is plotted in Fig. 4.7(a). It is clear how, at low power, the return power increases linearly, but as the power approaches 10 mW the line starts to bend down. Above 25 mW the light returning to the laser

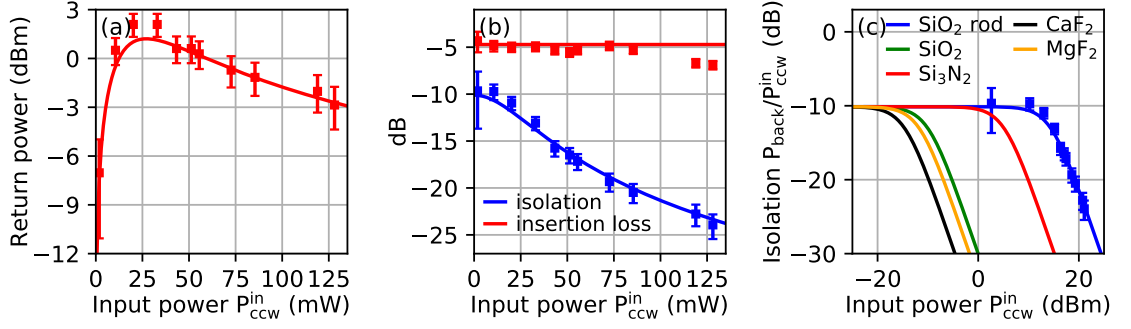


Figure 4.7: Characterisation of the isolator. The data-points and error-bars are from the experimental measurements while the line is the theoretical fit. (a) Power measured at the return photodiode as a function of the input power. Note how for increasing input power, the return power actually decreases. (b) Isolation improves with the input power while insertion loss is roughly constant. (c) The isolation fitted with our model and the extension to different materials with the parameters found in the literature. Adapted from [51].

decreases as the input power increases.

Two parameters generally characterise isolators: insertion losses L and isolation I . The insertion losses are what we so far called transmission T , defined as:

$$T = \frac{P_{out}}{P_{in}} \quad (4.38)$$

Where in this case P_{out} is the output power at port 2 and P_{in} is the input power at port 1. T is always a negative number, usually expressed in dB. Since the - sign is implicit, it is often dropped and this number is called insertion losses.

The other key parameter is the isolation that I defined as:

$$I = \frac{P_{back}}{P_{in}} \quad (4.39)$$

where P_{back} is the power going back into port 1 after being reflected by the mirror. These two quantities are shown in Fig. 4.7(b) together with a theoretical fit that works on both the dataset using P_0 and the coupling efficiencies as fitting parameters.

The fit in Fig. 4.7 provides the following results. The transmission of the tapered fibres are $T_A^2 = 90\%$ and $T_B^2 = 95\%$. The reflectivity of the mirror is $R = 95\%$. The intrinsic linewidth of the resonator is $2\gamma_0 = 4\text{ MHz}$ corresponding to $Q_0 = 1.5 \times 10^8$. The incoupling efficiency $\eta_{in} = 0.363$ and the transmission is $T = 0.346$. Unfortunately, the similarity between incoupling and transmission was not spotted

at the time of measurements but only when the setup was not available anymore for further measurements. The fact that almost all the power that enters the resonator leaves it on the other side is an indicator of strong overcoupling at the output. Indeed the calculated value for the outcoupling linewidth is $\kappa_B = 85 \text{ MHz} = 21\gamma_0$ with an incoupling linewidth of just $\kappa_A = 10 \text{ MHz} = 2.5\gamma_0$. This results in the output coupling reducing the effective Q factor to $Q_L = 6 \times 10^6$ corresponding to a characteristic power of $P_0 = 5.35 \text{ mW}$. Since the input is not critically coupled, part of the light continues in the input fibre instead of coupling into the resonator and it is wasted. Hence, the insertion losses are a non-exciting 5 dB.

Despite this measurement not representing the best performance possible for the rod resonator used, the achieved isolation was in excess of 24 dB at 125 mW input power. This value is comparable with the commercially available isolators based on the faraday effect. As an example the Thorlabs isolator IO-H-1550 is rated for an isolation of 29 dB.

4.2.4 Simulations for other materials

The isolation performances do not depend only on choice of coupling but also from the resonator material and platform. To demonstrate how the isolator would perform in different materials I used the same parameter from the fit above, including the poor choice of coupling parameters but changed the characteristics of the resonator as per Table 4.1. These data are extracted from recent literature on each platform. I used a default mode area $A_{\text{eff}} = 4 \mu\text{m}^2$ since it is a parameter rarely specified in the literature, and a diameter of $100 \mu\text{m}$ to even out the comparison. The results of

Table 4.1: *Parameters used to calculate how different materials and platforms would perform as isolators*

Material	A_{eff}	n [151]	n_2	Q_0
SiO ₂ rod	$10 \mu\text{m}^2$	1.444 [115]	$2.7 \times 10^{-16} \text{ cm}^2/\text{W}$ [37]	1.5×10^8
SiO ₂	$4 \mu\text{m}^2$	1.444 [115]	$2.7 \times 10^{-16} \text{ cm}^2/\text{W}$ [37]	5×10^8
Si ₃ N ₄ [92]	$4 \mu\text{m}^2$	2.463 [152]	$2.4 \times 10^{-15} \text{ cm}^2/\text{W}$	5×10^7 [92]
CaF ₂ [153]	$4 \mu\text{m}^2$	1.426 [117]	$1.9 \times 10^{-16} \text{ cm}^2/\text{W}$	1×10^9 [72]
MgF ₂ [31]	$4 \mu\text{m}^2$	1.37 [116]	$9 \times 10^{-17} \text{ cm}^2/\text{W}$	1×10^9 [112]

these simulations are plotted in Fig. 4.7(c) together with the data points measured in my proof of principle experiment. Note that the x scale is now logarithmic since the fluorides, having such a high Q-factor, show threshold powers of the order of

10 μ W. This is to be expected since the isolation threshold is proportional to P_0 so it scales as Q_0^{-2} . However, it is not only the Q factor that improves the isolation. as an example Si_3N_4 resonators still see a ten-fold improvement in the isolation threshold compared to the silica rod despite their lower Q . This is because they have a smaller mode area and a higher nonlinear refractive index n_2 . The isolation for power below the threshold power and the transmission for any power do not depend on the resonator characteristic but only on the coupling.

4.3 Circulator

In the configuration used so far, the light reflected at port 2 is mainly continuing straight through the tapered fibre to port 3 where is absorbed by a beam dump. This light can still transport useful information depending on what it is connected to port 2. So, instead of operating the microresonator as a simple isolator, I can measure the output from port 3 to access the reflection from port 2, making the device behave like a circulator.

For the device to work, the microresonator has to be polarized in one direction so the condition requested for the isolator is still valid: the input power at port 1 has to be higher than the input at port 2 at all times.

4.3.1 Methods

Figure 4.8 (a) shows a simplified scheme of the setup used to test this application. The setup is similar to the one used for the isolator with two main alterations. First, the amplified ECDL laser is now split by a 7 db directional coupler into two branches. The higher power branch is connected to port 1 representing the input laser, the lower power branch is instead connected to port 2 instead of the fibre mirror. Second, the beam dump at port 3 has been replaced with an additional photodiode (with appropriate attenuation to avoid saturation) to measure the transmission between ports $2 \rightarrow 3$.

4.3.2 Results and discussion

Figure 4.8 (a) shows the response of the circulator as a function of the laser frequency. The origin of the frequency axis is set to the cold cavity resonance where there is no

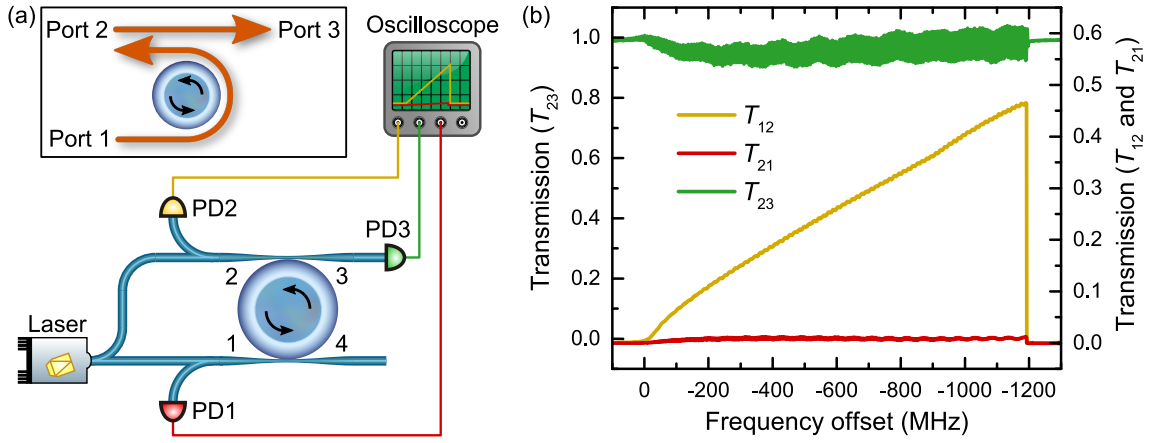


Figure 4.8: (a) Scheme and simplified setup of the circulator configuration. (b) Measurement of transmission through different ports of the circulator as a function of the frequency of the laser. The ideal working point for the circulator is at the resonance point on the right of the graph corresponding to a detuning of -1.2 GHz from the cold resonance. Adapted from [51].

thermal or Kerr shift. In this case, the measurement is performed at a single value of input power to show the response of the device to different input frequencies. Each of the measurements in Fig. 4.7 in the isolator section corresponds to the values of transmission and isolation at the peak of the yellow trace.

The yellow trace represents the transmission in the forward direction between ports $1 \rightarrow 2$ calculated as the ratio between the output power at port 2 and the input power at port 1. In this experiment, the coupling is optimised for critical coupling at the input and 50% transmission as in the blue trace in Fig. 4.5. The transmission increases as the laser gets closer to resonance up to about the desired value in resonance, reaching -3.3 dB.

The red trace represents the transmission in the backwards direction between ports $2 \rightarrow 1$ calculated as the ratio between the output power at port 1 and the input power at port 2. After an initial increase, when small light intensity is coupled to the resonator due to the detuning, the transmission remains flat and instead decreases when the laser approaches resonance reaching an isolation of over 19 dB.

The green trace represents the forward transmission of the output tapered fibre $2 \rightarrow 3$ that is almost constant at 1. At a closer look, there is a reduction in T_{23} when the laser is not yet resonant and the circulating light is not splitting the two resonances enough to prevent light from coupling backwards into the resonator; but as soon as the forward circulating power increases, no light can couple into the resonator from port 2 and T_{23} goes back to unitary values.

The noise on T_{23} appears to be somehow proportional to T_{12} . I interpret it as the interference between the light input at port 2 and the backscattering of the transmitted light either at the coupling point or at some fibre connection in the port 2 branches. These two waves propagate in the same direction and have the same frequency but they travel through different paths with different lengths, hence their relative phase changes with the frequency scan. The resulting interference goes from constructive to destructive several times during the scan and the amplitude of this pattern can be used to measure an unwanted transmission from port 1 to port 3 of -33 dB.

Throughout the chapter, we assumed that the resonator is held in resonance by the thermal locking. Figure 4.8 (b) shows that even if the laser is slightly blue detuned from the resonance, the performances are not affected in a significant way. In a small region to the left of the resonance T_{23} and T_{21} are roughly constant; only T_{12} decreases linearly.

One could be tempted to make a further extension to the number of ports. In principle any input into port 3 at the laser frequency will couple into the resonator because it is in the CCW direction and reach port 4, such as any input from port 4 will be off-resonance and continue through the tapered fibre to port 1. In theory, the device could be used as a four-port circulator. This is indeed possible, but the performances of the device will not be as good as for 3 ports for several reasons. It is far more difficult to guarantee isolation through a taper than through the resonator. In order to remove all the light from the taper, the resonator has to be perfectly resonant with that light frequency and there needs to be critical coupling. We already discussed how it is impossible to critically couple on both sides of the resonator unless both sides are strongly overcoupled. But overcoupling will reduce the circulating light intensity, hence the Kerr splitting, hence the isolation through the resonator. Finally, there will be interference between light coming from different paths that may be undesirable.

4.4 Conclusions

In this chapter, I described that it is possible to use the Kerr effect in a ring resonator to enforce non-reciprocal light propagation and realise an isolator or circulator. At low power, the device just works as a resonant attenuator since the transmission T

is symmetrical under direction reversal $A \leftrightarrow B$ but as the power increases, the Kerr nonlinearity kicks in and the device turns non-reciprocal.

The power at which this happens is of the order of 10 mW in the proof of principle experiment reported but this can be lowered by several orders of magnitude by utilising integrated resonators and different materials. The main limitation is the requirement that the input light has to be always at a higher power than the return light at the power on. During operation it is enough that the coupled power in the forward direction stays higher than in the backwards direction. This is usually the case in the applications requiring an isolator. As an example the microring isolator could replace the electrically controlled microring filters in [154].

In terms of integration, the device does not present particular challenges since it is composed simply by two waveguides coupled to a ring resonator. The main challenge is obtaining high Q-factor resonators and the control of the coupling strength between the resonator and the waveguides. Otherwise, this approach has none of the disadvantages of active devices that are important to consider for integration. The energy consumption is often not their main drawback because the power requirements are, in most cases, negligible compared to the rest of the system where the nonreciprocity is used. However, distributing energy to the device increases the fabrication complexity in case of electricity or requires additional light sources in case of optical energy. Thermal dissipation is an additional problem, especially when the temperature may produce unwanted effects such as changes in resonance frequencies. In the case of thermal locking instead, the temperature change is part of a negative feedback loop that extends the operating range of the device in the presence of laser frequency drift.

A final advantage over most of the competing technologies, including the Faraday isolator, is that the device presented here works at any wavelength in the transparency range of the material used to fabricate it; in the case of fused silica this range spans from 300 nm to 2 μm . The laser just needs to be operated in the vicinity of a resonance to exploit thermal locking.

Chapter 5

All-optical memory and switching dynamics

5.1 Introduction

In the previous chapter, we discussed how the Kerr effect allows light to travel in the microresonator just in one direction and how this can be used to realise an isolator. In the context of the isolator, we required a condition: the input laser has to be the highest power reaching the resonator¹. But what happens when the input power change while the resonator is in the symmetry broken region? In the isolator and circulator, I avoided a detailed study of this phenomenon since it is not necessary as long as we are dealing with passive linear devices. But let us now focus our attention to the case when the input power coming from the two opposite directions swings significantly.

I show in this chapter that by changing the inputs it is possible to switch the circulating direction of light in the resonator. If the laser is scanned across the resonance, with the same laser frequency in both directions, the dominating power at the point of symmetry breaking (let us call this direction A) is the one that will be coupled into the resonator. If the laser detuning is held in the symmetry broken region and the power in the initially weaker direction (called B) is increased to be equal to the other one nothing will change. But what happens when B overcomes A ?

¹In practice this condition is required only at the power on of the laser, then the precise requirement is that the circulating power in the forward direction has to be higher than in the backwards direction.

Initially, nothing will change because the higher input B sees just the tail of the resonance that has been Kerr-shifted by A , hence the circulating power for B will stay smaller than A for a while. Eventually though, the power arriving in the B direction will start pushing A out of resonance until the cascade effect described in Chapter 3 takes place and B becomes the dominating direction in the resonator and A is out of resonance because of the Kerr effect. At this point, the roles are swapped. If A is brought back to equal or slightly higher than B , it will not couple into the resonator. Only if A overcomes B by a sufficient amount, the circulating direction will switch again.

This particular behaviour is called hysteresis, i.e. the tendency of the system to remain in one of the two symmetry broken states. Hysteresis is an important property for a digital device since it is one of the ways of achieving noise resilience. Fluctuations of input powers or detuning cannot make the resonator switch the circulation direction, only considerable input imbalances can change the state of the system.

In this chapter, I introduce a dynamic model for the Kerr effect suitable for describing the switching process. I also discuss how to numerically integrate the model in order to generate simulations. I then describe the setup used to measure these dynamics and compare the results with the simulations. Finally, I discuss possible applications of this bistable behaviour to several digital devices with some examples of implementation.

5.2 Theory

The coupled equations presented in Eq. (3.30) describe the steady-state. How is it possible to extend the theory to describe the dynamics of the system? We need an equation that has the same steady-state as Eq. (3.31). But how to formulate it?

Some of the research on microresonators explores the generation of frequency combs or the generation of different wavelengths from the pump via four-wave mixing (FWM), another phenomenon related to the third-order nonlinearity $\chi^{(3)}$. In the context of this thesis, I actively avoid FWM by keeping the power not much higher than P_{th} and using resonators with the unfavourable geometrical dispersion such that FWM is suppressed for intermediate power. If some hints of FWM appear in the measurement, I check the transmission spectrum of the resonator with an optical

spectrum analyser (OSA) to verify if that is the case. FWM can be described, in a quantum approach, as the annihilation of two photons to generate two other photons at a different wavelength from the original ones. To obey energy conservation the mean frequency must be conserved and, because of momentum conservation, also the wavevector must be conserved, hence the dispersion has to be appropriate. In other words, the modes of the resonator have to be spaced correctly to be resonant with the new frequencies generated.

In the time domain this effect can be described by a driven damped nonlinear Schrödinger equation (NLSE), the Lugiato-Lefever equation (LLE) [32]:

$$\dot{e} = \tilde{e} - [1 + i\delta] e + i|e|^2 e + i\partial_\tau^2 e \quad (5.1)$$

Where \dot{e} represents the temporal derivative of the circulating field, \tilde{e} is the input field, the factor of 1 represent the normalised losses, δ is the detuning between the input and the cavity resonance. $|e|^2$ is the detuning induced by the Kerr effect and the last part $i\partial_\tau^2 e$ is often called the fast time component, i.e. represents the dynamics happening within a round trip. This last component is sometimes represented as a spatial derivative instead of a time derivative since the two dimensions are related by the speed of light in the medium.

This is a nonlinear equation, and it is complex-valued since the fields are represented in the complex notation. Without loss of generality we can take $\tilde{e} \in \mathbb{R}$ and the detuning δ is a real number.

The LLE has no analytical solution apart for specific assumptions or sets of solutions. One of these sets describes the steady-states solutions where $\dot{e} = 0$. We can separate two sub-sets: the patterns, where the solution is still dependent on the fast time τ and describes a field pattern inside the resonator that circulates around but is constant over time. The generation of frequency combs in microresonators and the study of solitons are part of this set of solutions [155, 156, 157, 158].

In this thesis, I focus only on the case when the dynamics happen much slower than the round trip time, in other words, the dynamics that take place over several round trips where only infinitesimal variation of the field takes place during a roundtrip time. Another subset of solutions called homogeneous steady-state (HSSs) where also $\partial_\tau e = 0$. This is the regime we discussed in the previous chapters.

Let us now focus on what happens when the fast time is still negligible ($\partial_\tau e = 0$)

but there are still dynamics happening in the slow time ($\dot{e} \neq 0$). We also need to consider that light also circulates in a second direction. We can implement this by adding the subscripts 1,2 with the notation that one equation is for the first subscript and another one holds for the second subscript instead of writing explicitly two coupled equations.

At this point in the thesis, you should be convinced that the contribution of the cross-phase modulation between the two directions is twice as much as the self phase modulation of the single direction. So we can add this to the equation as another term ($2|e_{2,1}|^2$). To sum up, we can write:

$$\boxed{\dot{e}_{1,2} = \tilde{e}_{1,2} - [1 + i(|e_{1,2}|^2 + 2|e_{2,1}|^2 + \delta)] e_{1,2}} \quad (5.2)$$

Note that setting the time derivative to zero and multiplying by the c.c. this equation, we find the Eq. (3.31) for the symmetry breaking.

It is also possible to build this equation from a different perspective, starting with the case of a simple resonator that can store energy where the driving electric field is resonant:

$$\dot{e}_{1,2} = \tilde{e}_{1,2} - e_{1,2} \quad (5.3)$$

In this case, it is clear than the circulating power is constant if the field entering the cavity \tilde{e} is equal to the one leaking out of the cavity $e_{1,2}$ (note that in this equation the losses are 1 for how e and δ are normalised). This is the simple case of a resonator with a finite cavity lifetime adapting to the changes in the input. If we add the detuning this corresponds to a de-phasing of the field in the resonator with respect of the input that gives us the Lorentzian line-shape in the steady-state case.

$$\dot{e}_{1,2} = \tilde{e}_{1,2} - e_{1,2} + i\delta e_{1,2} \quad (5.4)$$

By introducing the Kerr effect as a power dependent detuning, we reconstruct Eq. (5.2).

5.3 Time-step simulation

In the end, only the comparison with experimental data can prove the correctness of the model. But first, we need a way of integrating Eq. (5.2) to obtain the field as a function of time. I will not attempt to solve this equation, as in the case of Chapter 3, despite the fact that the behaviour can be extracted analytically in specific cases [159, 121, 122]. Instead, in this chapter, I will rely on finite element simulations.

A basic approach would be to just calculate the increment k as the time derivative at any step multiplied by the time-step h and calculate the next step as the previous one plus the increment.

$$e(t+h) = e(t) + k; \quad k = h \dot{e}(t) \quad (5.5)$$

This method is known as “Forward Euler” and has the drawback of diverging from the actual solution if this one has a constant sign second derivative. As an example, let us assume that the solution has a positive second derivative. For every step the first derivative calculation is performed at the beginning of the interval, hence the actual step in the interval would be always greater than the calculated one, leading to a divergence from the actual solution. This approach however just requires to know the initial condition and the first-order time derivative function:

$$e(t=0); \quad \dot{e}(t, e) \quad (5.6)$$

Even with just these informations, it is possible to get better results. To simulate the time evolution of the fields I will use the Runge-Kutta[160] RK4 time-step integration. It consists of evaluating the increment in 4 points:

$$\begin{aligned} k_1 &= h \dot{e}(t_n, e_n) \\ k_2 &= h \dot{e}\left(t_n + \frac{h}{2}, e_n + \frac{k_1}{2}\right) \\ k_3 &= h \dot{e}\left(t_n + \frac{h}{2}, e_n + \frac{k_2}{2}\right) \\ k_4 &= h \dot{e}(t_n + h, e_n + k_3) \end{aligned} \quad (5.7)$$

And finally calculating the step as:

$$e(t+h) = e(t) + \frac{k_1 + 2k_2 + 2k_3 + k_4}{6} \quad (5.8)$$

Looking at Eq. (5.7) we can see that k_1 is the same as the increment typical of the forward Euler method. However, three more increments are calculated: k_2 and k_3 are evaluated in the middle on the interval and k_4 is evaluated at the end of the interval. Each calculation is based on the previous, this improves the accuracy but prevents computational parallelisation of this method. The final increment is calculated in Eq. (5.8) as a weighted average of the 4 increments with a bigger weight assigned to the increments in the middle of the time-step. This approach prevents the drifts from the real function of the simple forward Euler method without adding too much computational effort. It also allows a longer time-step without compromising the accuracy of the results.

I optimise the length of the time-step by reducing it until the reduction provides no difference in the results. The most sensitive simulations are the ones at high power that require from 20 to 50 steps per unit of time defined as the inverse of the resonator half linewidth $1/\gamma$. The simulations in this thesis are all performed with 100 steps per $1/\gamma$ as a margin of safety.

Initial conditions for the numerical integration

There are two approaches to finding the initial conditions. First, it is possible to use the mathematical approach presented in Chapter 3 to obtain the initial power if it corresponds to a steady-state. The main problem of this approach is that the solution provides the power, i.e. the magnitude of the electric field but not the phase, that matters for the simulation. Also, the mathematical approach produces more than one solution if the parameters lie in the symmetry broken or multistable region, including the unstable solutions, hence it is not always easy to identify the solution of interest.

An alternative approach is to use the properties described in Section 3.2.3 to set the fields close to the solution of interest and let the simulation evolve with constant input fields until it stabilises. This simulation can be performed with coarse discretization to reduce the computational effort. The steady-state is found by checking the difference of the phase and amplitude of the circulating field between an iteration and the next one. Once the difference is below an arbitrary threshold,

I assume that the steady-state has been reached and I use it as the initial condition of the time-dependent simulation.

What can be simulated

The main input parameter for this simulation is the forcing field \tilde{e} and the laser detuning δ as a function of time. These parameters can be provided as functions of time or as a look-up table, allowing to simulate the response to any imaginable input. A few examples include sudden changes in power or power ramps for constant detuning while the laser frequency is scanned across the resonance. Also power, frequency and phase noise can be added.

Thermal effects are generally not included in the model since they do not produce any resonance frequency splitting. Still, they can be added to the simulation as a power and time-dependent change in detuning. However, the difficulty in obtaining realistic and accurate parameters for modelling the thermal effects, specifically the thermal capacities and conductivities of the system, makes it very difficult to build a reliable model.

5.4 Methods

The optical setup used to test the switching characteristics, shown in Fig. 5.1, is an improved version of the one used in the first symmetry breaking experiment. Light from an amplified external cavity diode laser (ECDL) laser is split equally into two branches that are connected to the two ends of the resonator input taper. There is, however, an extra component: since fast and accurate modulation of the

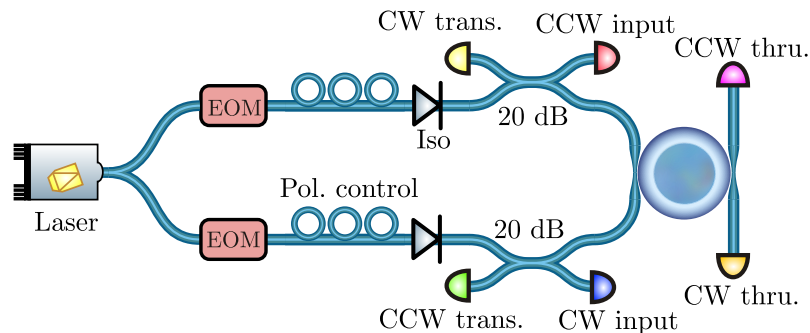


Figure 5.1: Scheme of the experimental setup used in the switching experiment.

light is needed to test the time response of the resonator, an optical modulator is

implemented on each branch. Initially, an acousto-optic modulator (AOM) was used but it was then replaced with an electro-optic modulator (EOM) for the reasons discussed in the following session. After each EOM an optical isolator protects the laser from return light, and a 20 dB directional coupler taps a small fraction of the light in both directions to measure the light input on the branch and the transmission from the other branch. The coupling setup used for the experiment is the same as the isolator experiment that allows coupling a second taper. As I will show in Section 5.5.3, this is not critical for the experiment but significantly simplifies the data analysis and makes the results clearer.

5.4.1 Square waves: AOM vs EOM

One of the key requirements of this experiment is to generate sharp step changes in the input power. Matching an ideal step function is necessary to observe the pure response of the resonator instead of a convolution between the input signal and the response. The timescale of the system response is the cavity lifetime of the resonator. As a reference value a loaded Q-factor of 10^8 corresponds to a cavity lifetime of $\tau_c = 165$ ns (the definition of τ_c can be found in Section 5.5.2).

In considering the possible modulator I aim to have transitions much faster than this timescale. Mechanical modulators such as shutters or choppers are excluded because the typical transition time is orders of magnitude too long. As an example, the Thorlabs SH05 shutter requires 750 μ s to switch and there are no intermediate levels between fully open and fully closed. Choppers are marginally faster but, in addition, they impose limitations on the modulation waveform. MEMS-based electronic variable attenuators such as the Thorlabs V1550PA provide intermediate attenuation levels but the bandwidth is still limited to 1 kHz. Two devices can provide a fast enough modulation: acousto-optic modulators (AOMs) and electro-optic modulators (EOMs). Let us quickly analyse the differences between the two.

A telecom grade AOM has a modulation frequency in the range between 80 MHz to 200 MHz. The switching time is not directly related to this frequency but it is the time it takes the acoustic wave to travel across the laser beam and steer it to the output fibre plus some transient for the wave to reach the final amplitude. I measured this time to be of the order of 30 ns in the AOM used in the experiment. However, this fast transition covers only about 80% of the total response, the remaining 20%

is probably due to the AOM heating up because of the acoustic wave power being dissipated in the device. This second part of the response is of the order of $3\ \mu\text{s}$ thus too slow for our purpose. Another drawback of an AOM is the amount of driving equipment needed. The AOM I used requires a high power RF input (2 W at 200 MHz). To generate such a carrier I need an RF generator, a splitter and two amplifiers. However, the generator cannot modulate the amplitude of the carrier RF frequency fast enough, hence I used a mixer on each branch to modulate the carrier (hence the AOM transmission) another 2 channel arbitrary waveform generator. Such a complex system makes the troubleshooting of every issue relatively time-consuming, involving a check of all the chain of components.

The other device considered for the modulation is an EOM. The EOM in its simple form is a waveguide interferometer comprising electro-optic materials such as LiNbO_3 , where the phase delay in one arm is controlled by the voltage applied to the electro-optic material. Generally, the input losses are worse in an EOM than in an AOM (-5 db vs -3 dB) but the driving electronics is just a voltage generator connected to it and the switching is generally much faster. The EOMs used in the setup take 8 ns to switch, just 3 ns slower than the transition of the signal generator, probably because of an impedance mismatch between the two. This makes sense given that the bandwidth of the EOM is 10 GHz. However, EOMs have a major problem that is the reason why they were not used in the first place. The fast response is only a third of the total response of the EOM followed by two thirds that takes place in a few microseconds. The slow component of the response is likely to be some spurious capacity of the EOM plates that slowly polarises the electro-optic medium. But there is a way around this effect.

5.4.2 EOM overdrive

The slow charging affects the phase delay accumulated in the interferometer arm, but this can be compensated by an additional voltage applied across the material. In other words, it is possible to overdrive the EOM for the charge not yet accumulated to change the transmission immediately to the final state and then lower the input voltage gradually as the slow charging completes.

A first way of implementing this is to drive the EOM with the desired profile and measure the resulting optical power. The measured optical power is then compared

with the desired one and the output of the arbitrary waveform generator is re-programmed adding the difference between the two signals to the original one. The process is then repeated a few times, modifying the signal generator output by the discrepancy between the last optical signal and the ideal one. This approach does not converge on the desired signal but instead oscillates around it. The simple solution is to correct the electrical signal by half of the error, this slows down the convergence but removes the oscillations.

Since programming a new waveform in both channels of the function generator requires almost a minute, I developed a quicker approach: The response to a step input is fitted with an instantaneous component and 3 exponential components with their time constant bound to the range of interest. This binding is necessary to avoid that some component drifts to very short time to compete with the instantaneous part, or overlap with the others. An example of this fit is shown in Fig. 5.2.

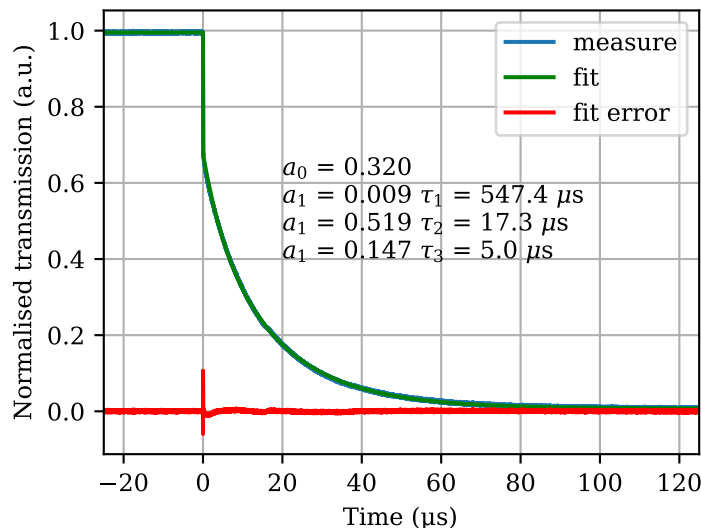


Figure 5.2: *Fit of the EOM response to a step function. The traces for the fit (green) and the measure (blue) are almost indistinguishable. The red trace is the difference between the two multiplied by a factor of 100.*

I use two different fitting functions for the falling slope:

$$P(t - t_0) = \Theta(t_0 - t) + \Theta(t - t_0) [a_1 e^{-(t-t_0)/\tau_1} + a_2 e^{-(t-t_0)/\tau_2} + a_3 e^{-(t-t_0)/\tau_3}] \quad (5.9)$$

And for the rising slope:

$$P(t - t_0) = \Theta(t - t_0) [1 - a_1 e^{-(t-t_0)/\tau_1} - a_2 e^{-(t-t_0)/\tau_2} - a_3 e^{-(t-t_0)/\tau_3}] \quad (5.10)$$

Where Θ is the Heaviside function², $\tau_{1,2,3}$ are the 3 time constants for the 3 exponential decays, and $a_{1,2,3}$ are their relative weights. The initial sharp transition is modelled as instantaneous and having an amplitude of a_0 . Since the fitted signal is normalised between 0 and 1, by definition:

$$a_0 \equiv 1 - (a_1 - a_2 - a_3) \quad 0 \leq a_{0,1,2,3} \leq 1 \quad (5.11)$$

The fitting function also includes t_0 which is the time where the switching begins.

Note how, in Fig. 5.2, the fit curve overlaps almost perfectly with the transmitted power. The fit is repeated for different modulation amplitudes and for both slopes resulting in values for the amplitudes and the time constants within 5%. The values, however, are different for the different EOM used. Also, note how the amplitude of the longer time constant is very low compared to the others, nevertheless, including the third exponential, helps the fit to converge to a lower error on the two principal components.

Once the EOM response is fitted it is possible to iterate the algorithm to calculate the input waveform in a simulated way and use the resulting waveform to drive the EOMs. As you can see in Fig. 5.3, the result is a huge improvement in the shape of the optical signal. This iterative technique to calculate the appropriate

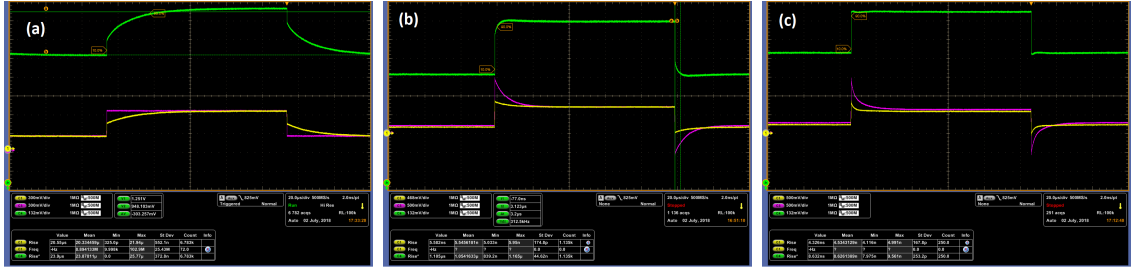


Figure 5.3: *The response of the EOM to a square wave input without modifications (a), with a single component exponential fit overdrive (b), and with three components overdrive (c). Pink \rightarrow the output voltage of the function generator on a high impedance load. Yellow \rightarrow the voltage at the EOM input. Green \rightarrow optical power transmitted through the EOM. The graphs represent a time span of 200 μ s.*

electrical input to achieve the desired output proves particularly useful when several transitions of different amplitude happen in rapid succession before the charging of

²One needs to be careful in defining the discontinuity point at $t = 0$ because it can affect the fitting. I defined the two functions differently such that one of the two includes the $t = 0$ point and the other doesn't. However a simpler approach could be to define $\Theta(0) \equiv 0.5$. This solution avoids spikes in this case even if it does not solve the discontinuity.

the EOM plates completes. See, for example, how an amplitude-modulated square wave signal improves once the algorithm is applied in Fig. 5.4.

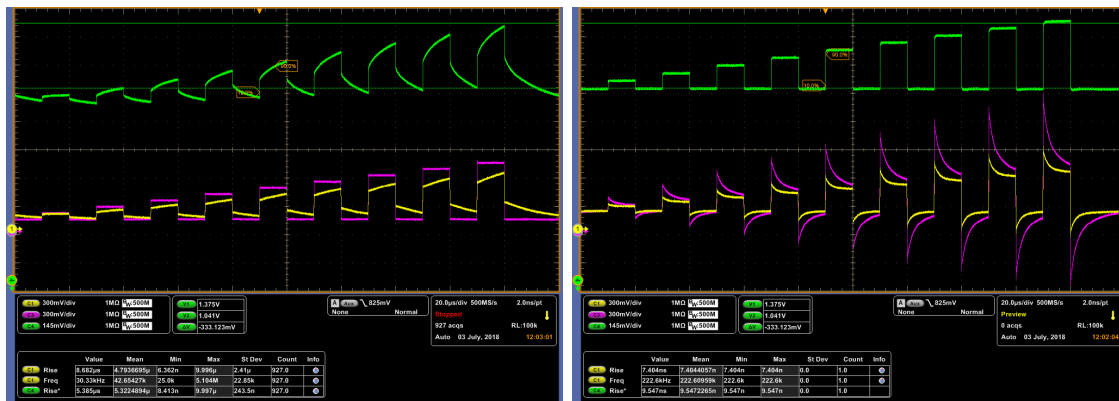


Figure 5.4: *The EOM response without overdrive (left) and with overdrive(right). Pink \rightarrow the output of the function generator on a high impedance load. Yellow \rightarrow the voltage at the EOM input. Green \rightarrow optical power transmitted through the EOM.*

5.5 Results and discussion

5.5.1 Hysteresis

I mentioned so far the Hysteresis in a qualitative manner. It is finally the time to discuss it more quantitatively. The procedure to solve the coupled equations described in Section 3.2.2 can be adapted to solve for imbalanced input powers. If the two power are imbalanced this corresponds to solving for $s = 1 - \tilde{p}_{CCW}/\tilde{p}_{CW}$ instead of $s = 0$. This is the method used to obtain Fig. 5.5(a). The solutions for different imbalances are colour coded in red and blue for the two possible directions of the imbalance. In the regime called “enhancement” in the figure, if the imbalance is swept from red to blue, also the solution sweep continuously but, close to the symmetry breaking points this imbalance is amplified in the circulating powers. In the “bistability” regime instead, this continuous sweep is not possible. Let us start with the resonator at the bottom of the bubble for $\delta = -3$ and with equal input power. The CCW direction is fully coupled in the resonator, while CW, the one plotted in the graph, is only marginally coupled. The first thing we can observe from the graph is that a small imbalance in either direction, i.e. faint colours, now do not cause a transition to the opposite side of the bubble but just a minor oscillation around the same side. Instead, if the imbalance drifts significantly towards the

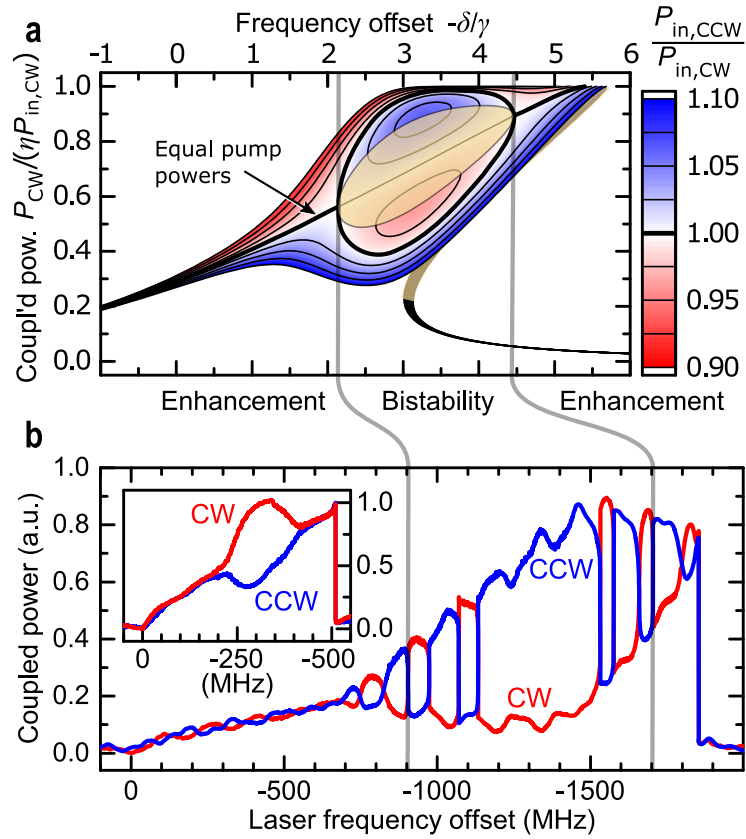


Figure 5.5: *Different regimes of symmetry breaking and hysteretical behaviour. (a) A contour plot of the solution of the symmetry breaking equations as a function of the detuning. The black thick line is the solution for equal input power in both directions as already seen in Chapter 3. The case of imbalanced input is colour coded in red and blue and the three regimes are highlighted. (b) A measure of the different regimes. The laser is scanned through the resonance while the power imbalance oscillates. The inset shows the same resonance with equal powers in both directions. Adapted from [87].*

CW direction, we can see that there are no solutions on the bottom side of the bubble but only on the upper branch. Hence the resonator will abruptly switch to the opposite branch. This is the signature of hysteresis: small modulations cannot start a transition, while a large one causes a sharp switching. The same can be seen experimentally in Fig. 5.5(b) where the laser is scanned through the resonance while the imbalance between the input powers in the two directions oscillates³. Before the symmetry breaking point, the oscillation is amplified more and more as the frequency approaches the symmetry breaking point. After the symmetry breaking point, the resonator keeps switching between the two branches but now the profile is not sinusoidal. Instead, we can see a sharp transition. In the middle

³this oscillation is obtained by “introducing” a dirty connector on the tapered fibre. This creates an interferometer that goes from constructive to destructive interference as the frequency changes. It is a poor-man amplitude modulator.

of the bistable regime, the modulation is too small to induce a transition and the resonator oscillates around the current solution. This has to be compared with the inset in Fig. 5.5(b) where the power in both directions is perfectly balanced and corresponds to the black curve in panel (a).

Let us now test how the hysteresis amplitude depends on the circulating power. For each panel in Fig. 5.6, the input power in both directions is modulated by a triangular wave at 4 kHz with opposite phase. By doing so the total power sent to the resonator is constant while the imbalance changes smoothly. Both the input powers in each direction and the corresponding transmission are measured. However, plotting these values over time does not show the hysteretical behaviour of the resonator in a readable manner. Hence I plotted these data as the coupled power in each direction as a function of the power imbalance.

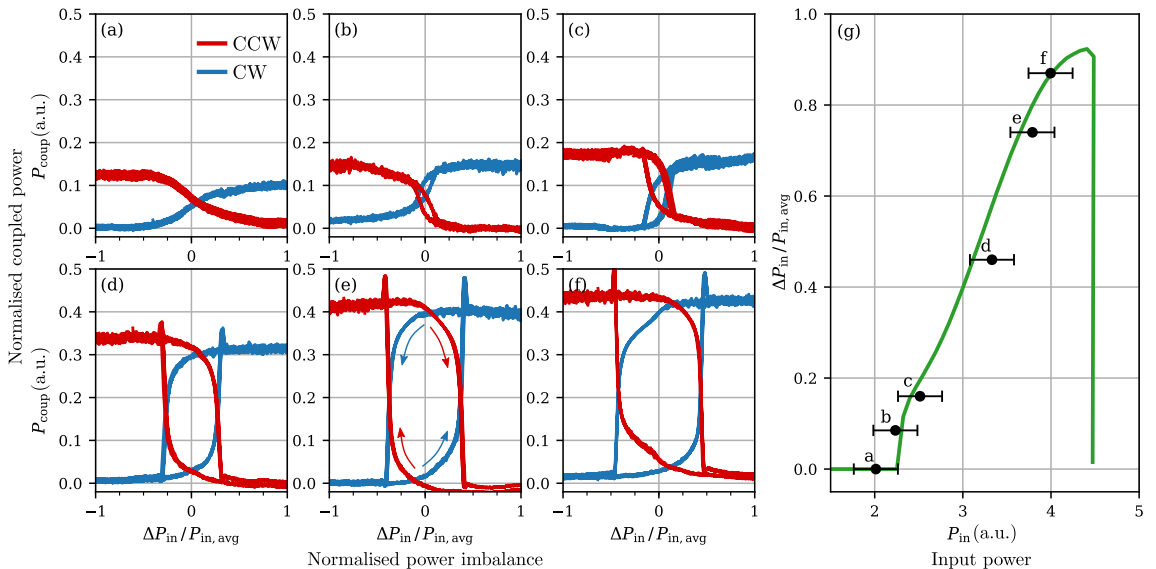


Figure 5.6: Panels (a-f) Hysteresis profile for increasing circulating power in the resonator. Panel (g) Amplitude of the hysteresis, a comparison between the theoretical model and the experiment. Adapted from [52].

The horizontal axis of each panel is calculated as:

$$\frac{P_{\text{in,CW}} - P_{\text{in,CCW}}}{(P_{\text{in,CW}} + P_{\text{in,CCW}})/2} = \frac{\Delta P_{\text{in}}}{P_{\text{in,AVG}}} \quad (5.12)$$

so that the value of 0 corresponds to both inputs having the same power, and positive values to the CW direction being stronger than the CCW direction. To obtain comparable results for different values of the circulating power, I change the detuning between one panel and the other. We have seen in Chapter 2 that both a

change in detuning or launched power can have an effect on the circulating power but using the detuning allows taking measurements in rapid succession, ensuring that no long term drift takes place. The vertical axis of each panel is the coupled power (i.e. the transmitted power out of resonance minus the actual transmitted power) normalised by the input power so that an increase in P_{coup} proportional to the input appears as a horizontal line. The configuration of the setup and the resonance under investigation has a coupling efficiency $\eta = 0.55$ so no value higher than this can be reached on the vertical axis. In the absence of nonlinearity, the two coupled powers would appear as a horizontal line at the corresponding coupling level.

We can see that already at low power the Kerr effect reduces P_{coup} for the weaker input but the two traces follow the same path, no matter if the power imbalance is swinging in one direction or the other. As the total power increases, the coupled power starts to follow two different paths while the imbalance is scanned in the two directions, with the resonator that tends to stay in the previous state even after the 0 imbalance point as indicated by the arrows. Note how the width of the hysteresis pattern increases with increasing circulating power. This is shown in the recap graph in Fig. 5.6(g). The vertical axis of this panel reports the width of the hysteresis from panel (a) to (f) measured at half maximum. The horizontal scale has been converted to circulating power in units of the characteristic power P_0 to allow comparison with a theoretical simulation that uses the same parameters for the resonator and also uses the detuning as a mean of controlling the coupled power. We can see how no hysteresis is expected at low power and how the increase in amplitude is described by the model. Note also how the hysteresis sharply drops in the model after a certain detuning is reached. This is caused by the laser passing on the blue side of the resonance, therefore losing the thermal lock. The same effect is observed in the experiment.

5.5.2 Effect of the input parameters on the switching profile

Once the existence of the hysteresis is proved, let us analyse how the switching dynamics is affected by the different parameters of the input. Since we are also interested in the speed of the switching process, let me define the notation I will be using for the timescale. I am interested in drawing a parallel between the mi-

microresonator based optical devices and the electronic devices I will assume that the microresonator behaves like an LC resonator. Hence, the achievable bitrate R can be defined as the inverse of the rise time τ_r . The rise time itself represents the time that a cavity takes to go from 10% to 90% of the transition. If we write the relation between the cavity lifetime τ_c and the rise time is:

$$\tau_r = 2.197 \tau_c \quad (5.13)$$

Finally the cavity lifetime is related to the loaded Q factor by the relation:

$$\tau_c = \frac{Q}{\omega} \quad (5.14)$$

Hence the achievable bitrate is inversely proportional to the loaded Q-factor of the cavity:

$$R = \frac{\omega}{2.197 Q} \quad (5.15)$$

To isolate the dependence of the switching speed and profile from each parameter independently, the total input amplitude sent to the resonator is kept constant. Every time the input power in one direction is increased, the other direction is attenuated by the same amount. By doing so we can expect that if the switching happens and the resonator ends in the opposite state, the circulating power in the initial and final state will be the same hence we can neglect the thermal effects.

I would like to highlight that our model is symmetric for exchange in $1 \leftrightarrow 2$ or $CW \leftrightarrow CCW$, but since it is also nonlinear, it is not guaranteed that the switching will happen or what is the final states, just that the same state for $1 \leftrightarrow 2$ exist.

Modulation amplitude

Let us define the modulation amplitude around a certain offset or average power. In this case by average power P_{avg} of a square wave or a signal that switches between 2 states, I do not mean the average over time of the power, but the value in between the HIGH and the LOW states as shown in Fig. 5.7:

$$P_{avg} = \frac{P_{HIGH} + P_{LOW}}{2} \quad (5.16)$$

The modulation amplitude M is defined as half of the power difference between the HIGH and LOW states, normalised by the average power:

$$M = \frac{P_{\text{HIGH}} - P_{\text{LOW}}}{2} \frac{1}{P_{\text{avg}}} = \frac{P_{\text{HIGH}} - P_{\text{LOW}}}{P_{\text{HIGH}} + P_{\text{LOW}}} \quad (5.17)$$

A modulation of 0 corresponds to a constant power at P_{avg} . A modulation of 100% corresponds to the power going between 0 and twice the average power. A modulation of 42% corresponds to $P_{\text{HIGH}} = 1.42P_{\text{avg}}$ and $P_{\text{LOW}} = 0.58P_{\text{avg}}$.

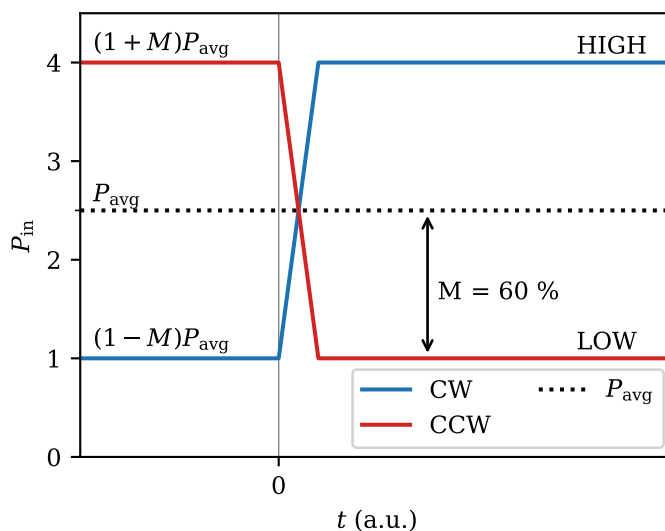


Figure 5.7: Definition of the modulation amplitude for a signal around its average power as used in this chapter. In this example $P_{\text{avg}} = 2.5P_0$ and $M = 60\%$

If not specified differently, I am considering the case where the two directions are in opposite states or, if the power change is gradual, that the total input power remains constant, i.e. if the input power in one direction increases, the input power in the opposite direction decreases by the same amount. By doing so we can separate the effects related to the change in total power from the ones related to the imbalance in power between the two directions.

To measure how the switching profile changes with different modulation amplitudes, the resonator needs to be set in an initial state and then different power modulations are applied while recording the power in the resonator through the drop fibre. The two input powers are opposite in sign around a common offset. I performed an initial test with a 50 kHz square wave, amplitude modulated by a sawtooth wave at 1 kHz in order to produce increasingly higher power steps.

This initial approach highlighted two problems. At small amplitudes the mod-

ulation is not enough to reset the resonator always in the same state because it cannot overcome the hysteresis, resulting in the first part of each measurement being affected by the initial random choice of the circulating direction. Even when the modulation becomes sufficient to overcome the hysteresis, the initial state is different for every cycle of the square wave because the initial conditions are different.

To overcome these problems I designed the test waveform shown in Fig. 5.8. Initially, a power imbalance large enough to overcome the hysteresis is applied to

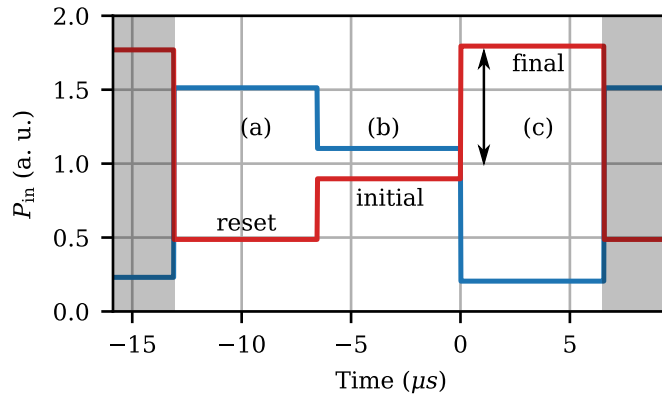


Figure 5.8: *The input signal in each direction (blue \rightarrow CW, red \rightarrow CCW) used to measure the response to different modulation amplitude. A cycle of the signal is highlighted: part (a) and (b) of the signal are constant while (c) changes slightly every cycle. Adapted from [52].*

reliably set the resonator in the CW state (a). Then the power imbalance is reduced to 10% of the average power (b): This constitutes the initial state for the experiment. Finally, the powers are switched to an imbalance that gradually increases every cycle for 200 cycles, starting from 0 up to switching off completely one direction and doubling the power in the other one (c). The time between the transitions is long enough to let the resonator settle to the steady-state before switching the input powers.

The input power and the output at the drop fibre are recorded with a fast oscilloscope (500 MHz bandwidth, 2 GSps sampling rate) and the resulting traces are analysed in Python.

All the measurements in this section are taken as follows. First, the analysis script identifies the steady-state and normalise the signals from 0 to 1. There is not a trigger for each cycle but I use one of the input traces to identify the start of the transitions and plot each one at the zero of the time scale. This small complication in the data analysis allows us to take all the measurements in a burst of 4 ms, preventing any long term drift of the system from affecting the measurements.

The results of this measurement are reported in Fig. 5.9 and compared with a simulation calculated for a resonator with the same Q-factor and a reasonable guess for the value of P/P_0 and δ/γ . Only a part of the 200 cycles is plotted for clarity

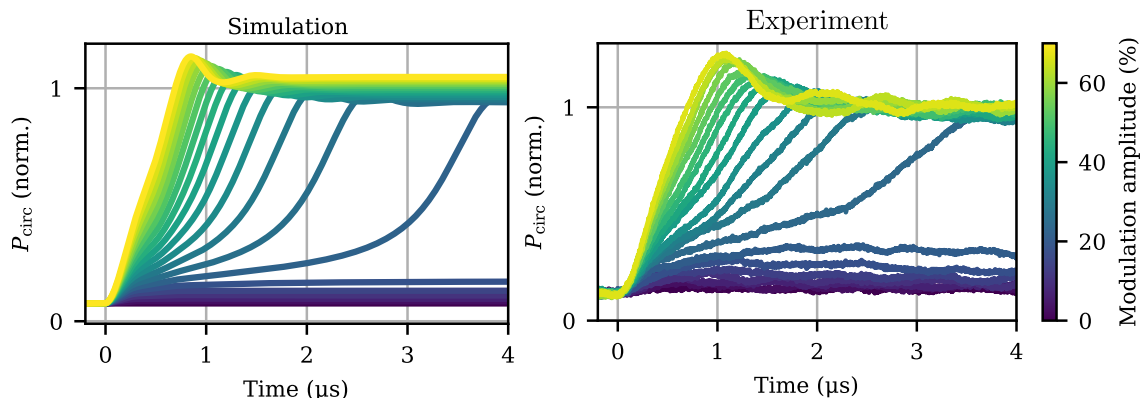


Figure 5.9: *Switching profile as a function of the modulation amplitude. On the left, a simulation of the switching profile for the input in Fig. 5.8 and the following parameters: $P_{\text{avg}} = 3.7P_0$, $\delta = -3.5\gamma$, $Q = 1.6 \times 10^8$, modulation amplitude ranging from 0% to 70%. On the right, the measurement of the switching profile with the same Q and the same input as the simulation. Adapted from [52].*

but there is no abrupt behaviour as the modulation amplitude changes.

For small modulation, the resonator cannot overcome the hysteresis. Still, since the launched power changes, a small difference in the LOW level can be observed. At 20% imbalance the modulation amplitude is enough to overcome the hysteresis and the resonator switches to the opposite circulating direction slowly. As the amplitude increases further, so does the switching speed up to saturation.

For high modulation amplitude, an overshoot and ring-down start to appear. This can be explained by remembering that the thermal locking is on the side of the resonance. As the switching happens the resonance frequency wobbles due to the Kerr dynamics of the system and the resonator temporarily access a smaller effective detuning than in the steady-state resulting in this overshoot. Locking the resonator closer to the peak of the resonance results in a smaller oscillation but also makes the thermal locking less stable because it may happen to end up on the red side of the resonance and lose the lock.

Note that the resonator used in this measurement has a $Q = 1.6 \times 10^8$ corresponding to a cavity lifetime $\tau_c = 130$ ns and a rise time $\tau_r = 290$ ns. The measured rise time of 570 ns for the highest modulation amplitude of 70% is still a bit slower than expected from the Q-factor. This is probably because the interaction between

the two directions is driven by nonlinear effects, while in the definition of cavity lifetime a linear model is assumed. A quick test of the time step algorithm, performed by removing the Kerr effect from the model, shows a transition time that agrees with the definition. This suggests that the Kerr interaction between counter-propagating light slightly increases the build-up time compared to the linear case.

Total power

Quite surprisingly the total power has a minor effect on the switching. It only affects the ring-down amplitude and frequency, and changes the intensity profile. However, the switching time is only marginally faster for higher input power.

The total power in Fig. 5.10 ranges from $1.7 P_0$ to $8 P_0$. The modulation amplitude used in the figure is from 1.7 to 0.3 of the P_{avg} and the detuning is appropriately changed to be just before the maximum coupling in the HIGH state.

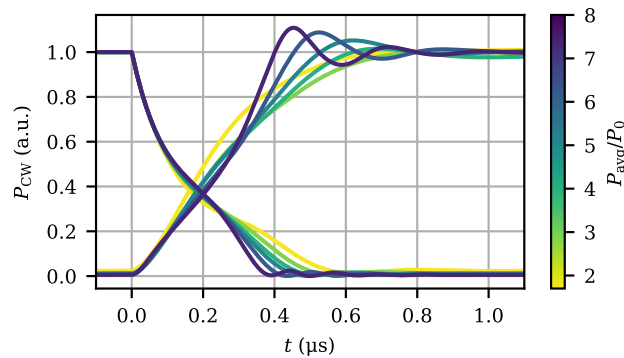


Figure 5.10: *Switching profile as a function of the total power in the resonator, for a modulation amplitude of 70% and a Q-factor of 10^8 . Adapted from [52].*

Power offset

The power offset picture does not provide additional insight in the dynamics. If the average power is offset, the switching in one direction will see a larger modulation amplitude and switch faster while the other direction will see a smaller modulation amplitude and switch slower. As an example, the darkest curve in Fig. 5.11 sees a power difference of $1P_0$ at $t = 0$ (modulation amplitude of 20%) while it sees a power difference of $5P_0$ at $t = 2 \mu\text{s}$ (modulation amplitude of 100%). This difference in switching speed between the rising and falling edge, can actually be used to ensure that input powers are indeed symmetric in the experiment.

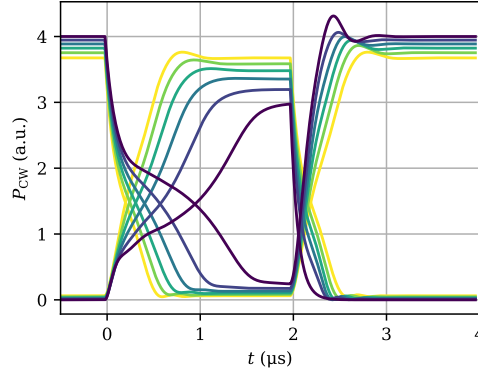


Figure 5.11: *Switching profile as a function of the average power offset between the two input directions. In the yellow curve the levels are equal for both directions $P_{\text{HIGH}} = 4P_0$ and $P_{\text{LOW}} = 1P_0$. This is gradually changed maintaining the absolute modulation amplitude to $P_{\text{CCW}} = 0 \sim 3$ and $P_{\text{CW}} = 2 \sim 5$. The other parameters are: $\gamma = 1 \text{ MHz}$, $\delta = -3.5\gamma$.*

Laser detuning

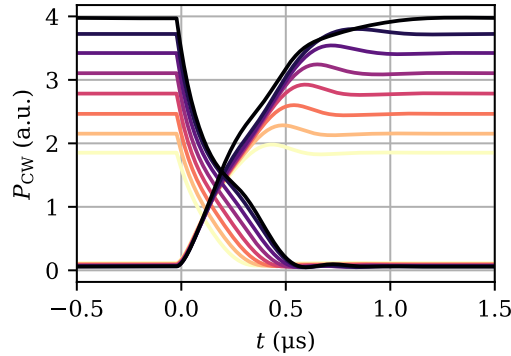


Figure 5.12: *Switching profile as a function of the detuning. The detuning varies from -1 (yellow) to -4 (black). The simulation parameters are: $P_{\text{avg}} = 2.5P_0$, modulation amplitude of 60%, $\gamma = 1 \text{ MHz}$ corresponding to $Q = 10^8$.*

Not much changes in the switching profile with the laser detuning from the resonance, as long as the power is enough to observe symmetry breaking and the detuning is in range (cf. Fig. 5.12). The only difference, for small values of the detuning, is that the final state is not well coupled in because the resonator is operating far from the Kerr shifted resonance.

5.5.3 Speed and Eye diagram

Figure 5.9 already provides an idea of the switching speed of the resonator. However to better characterize the device I measured its eye diagram. The eye diagram is a

representation of the switching characteristics of a digital device commonly used in electronics. It shows the response of the device to a random bit sequence input such as the one shown in Fig. 5.13. The input signal randomly switches or stays constant every clock cycle, marked by the vertical lines in the plot. The bitrate of the signal is the frequency of the clock.

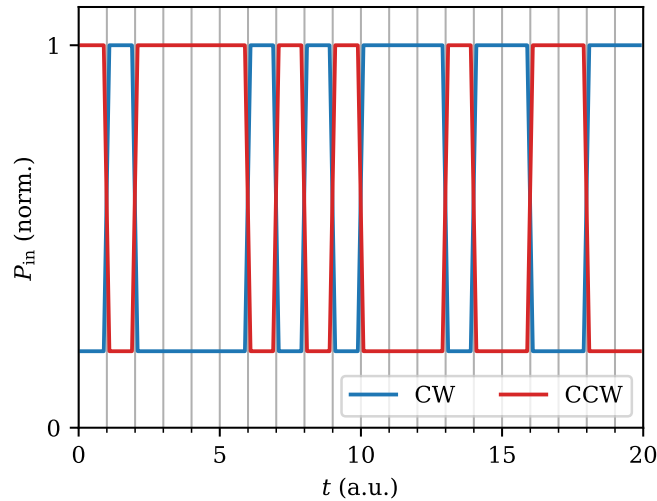


Figure 5.13: *An example of a random bit input sequence.*

The eye diagram consists of the output of the device over time, but instead of using a constantly increasing timescale, the trace is overlaid multiple times, each one translated by an integer multiple of the clock period. This allows us to zoom in on the time span of a single clock period comparing in details the responses to all the possible input sequences. An infinitely fast device facing a perfect step input should present a square-shaped eye diagram. In the real world, the transition takes time to happen so the square morphs into a plot that vaguely resembles a human eye, hence the name eye diagram. An “open” eye means that the device under test is responding correctly to the input signal. A “closed” eye indicates that the response to the signal is too slow and eventually the device does not reach the steady-state levels HIGH and LOW.

Figure 5.14 shows the eye diagram for the experiment. The Q-factor has been reduced compared to the previous measurements to 1×10^8 by increasing the coupling with the second taper to improve the speed.

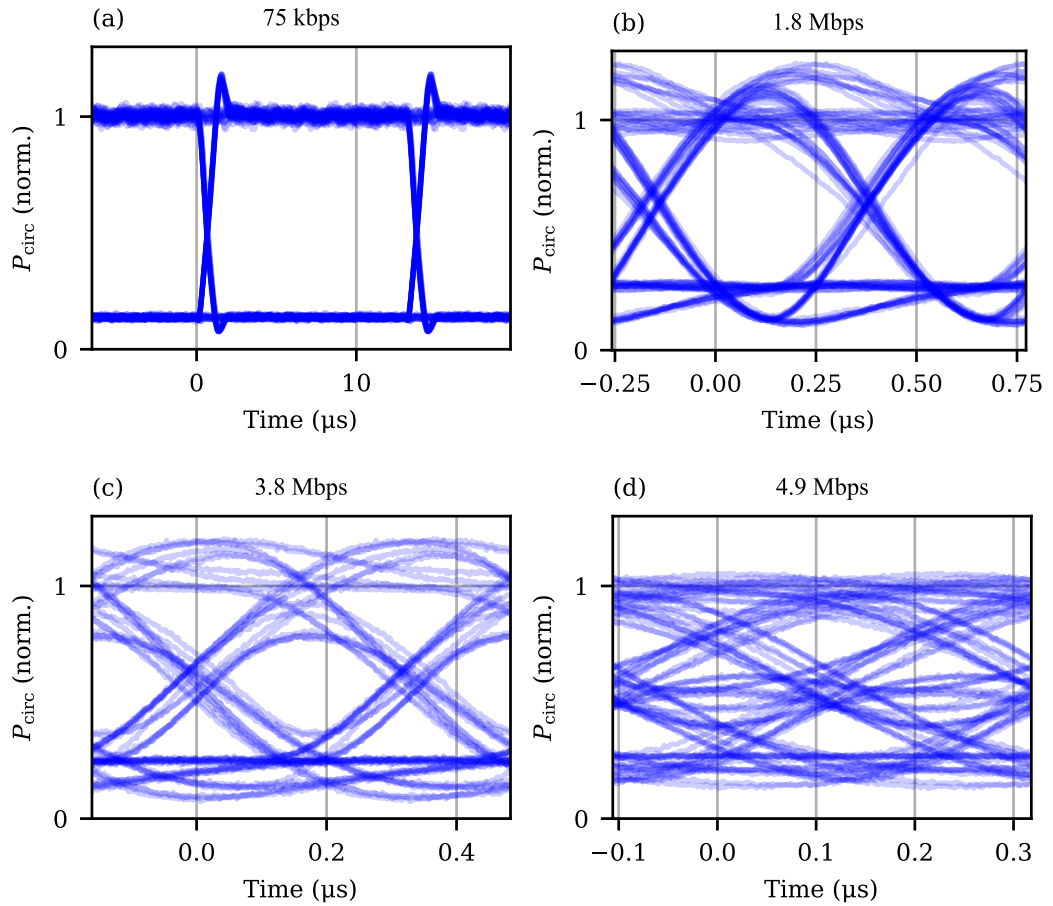


Figure 5.14: Eye diagram of the microresonator used as optical memory for different input bitrates. (a) 75 kbps, (b) 1.8 Mbps, (c) 3.8 Mbps, and (d) 4.9 Mbps. Adapted from [52].

At a clock period much longer than the calculated rise time ($\tau_r = 180$ ns) results in the diagram looking almost like a perfect square (a), just a small overshoot can be seen after the transitions. In panel (b) the resonator can follow the input at a bitrate of 1.8 Mbps. There is still a clear region in between the clock transitions where it is possible to discern if the resonator is in the HIGH or LOW state. Panel (c) shows the limit situation where the eye starts to close at 3.8 Mbps. Despite this, it is still possible to draw a separation line between the HIGH and LOW states, but the signal at the top and the bottom of the eye does not reach the steady-state level. Also, it starts to be clear how the switching profile depends on the previous states. If the resonator was in the initial state for more the one clock cycle, the profile differs from the one that happens when the resonator was in the initial state for more than one clock periods. Finally, in panel (d), the output of the device under test cannot follow any more the input bitrate of 4.9 Mbps. The eye is completely closed and the device cannot complete the switching when two transitions follow consecutively.

Consideration on the use of a second tapered fibre

All the measurements of the dynamics presented so far in this chapter are measured from the drop taper. Having a second taper coupled to the resonator not only makes it possible to monitor the switching speed, but it can also be used as a mean to change the effective Q-factor of a resonator without physically replacing or irreversibly damaging it. Also, the output of the second taper is always proportional to the circulating power. Instead, in a transient situation, the definition of coupled power is not proportional any more to the intracavity power so the single taper setup may not be the most suitable to study the transient situation.

Nevertheless, we will see how an optical memory can be built with a single taper if the transient profile is not crucial. Figure 5.15 shows one of the preliminary measurements of the eye diagram. Let us overlook the fact that these measurements

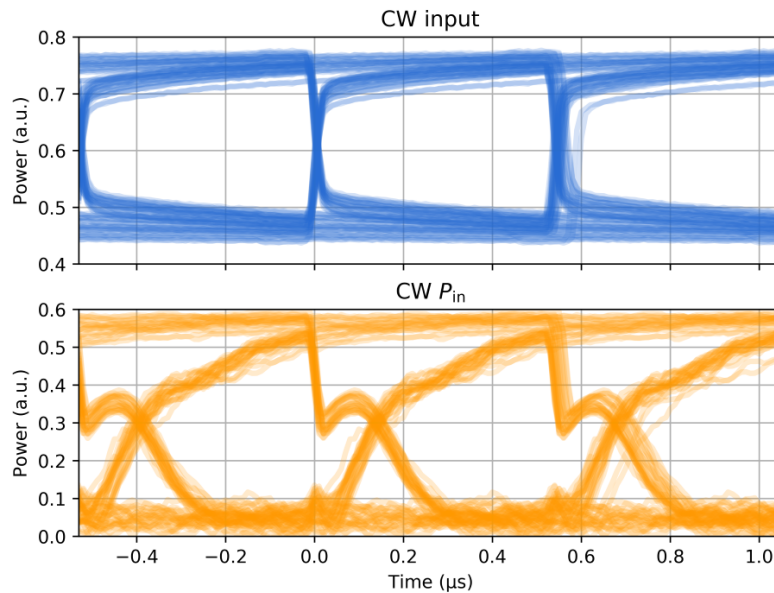


Figure 5.15: *One of the preliminary measurements of the eye diagram for a modulation amplitude of 50 % performed with a single tapered fibre coupled to the resonator. (Top) the input signal, (bottom) the coupled power calculated from the transmission.*

were performed with an AOM and the algorithm to identify and fold at the transition was not optimised, causing jitter in the data. I would like to highlight the curious switching pattern. The coupled power is calculated as the HIGH level input power minus the transmitted power in the same direction. This however, does not reflect the circulating power in the resonator since we cannot assume anymore that the intracavity power is proportional to the power missing from the transmission: the resonator is not in the steady-state. In the transition from HIGH to LOW, the first

sharp step is due to the reduction in the input power in that direction. Then the frequency detuning starts to change due to the exchanging roles of the two directions. As the light field leaks out of the resonator, also the relative phases of the circulating power with respect to the pump change, causing the peculiar bounce in the observed coupled power. The same effect is visible in the transition LOW \rightarrow HIGH but it is less accentuated since the power increase is masked by a far detuned resonance. Note that the duration of the switching process is the same if observed by the input or output taper, just the shape is different.

5.5.4 Different materials and platforms

As the reader may have noticed the bitrate of 3.8 Mbps is not competitive with the current electronic or even optical alternatives. This is because the resonator under test has a high Q-factor to reduce the modulation and threshold power requirements. We are mostly interested in 2 parameters: the switching speed and the threshold power, i.e. the minimum working power for the device. We already know from chapter 3, that the threshold power for the symmetry breaking is

$$P_{\text{th}} = \frac{1.54}{\eta} \frac{\pi n_0^2 V}{n_2 \lambda Q Q_0}, \quad (5.18)$$

where I kept η explicit because it is a parameter that I can use to optimise the speed. I defined the time parameters in Section 5.5.2. Here I will just remember that:

$$R = \frac{\omega}{2.197 Q}. \quad (5.19)$$

As discussed in Chapter 2, the intrinsic Q-factor depends on the losses in the resonator itself. Adding losses to the resonator via coating, scratches or an additional tapered fibre would increase the switching speed but also require more power to access the hysteresis regime. The loaded Q-factor instead can be tuned through the coupling of the input taper. Figure 5.16 is a map of the possible performances that can be achieved with different materials. Instead of plotting a single point for each material, the tunability given by the coupling strength is highlighted. For each curve, κ has been left free to change between $1/30\gamma_0$ and $30\gamma_0$, a realistic range of values. The Q_{eff} scale on top of the graph is obtained through Eq. (5.15) by assuming the operational wavelength of 1550 nm. This scale does not apply to silicon resonators

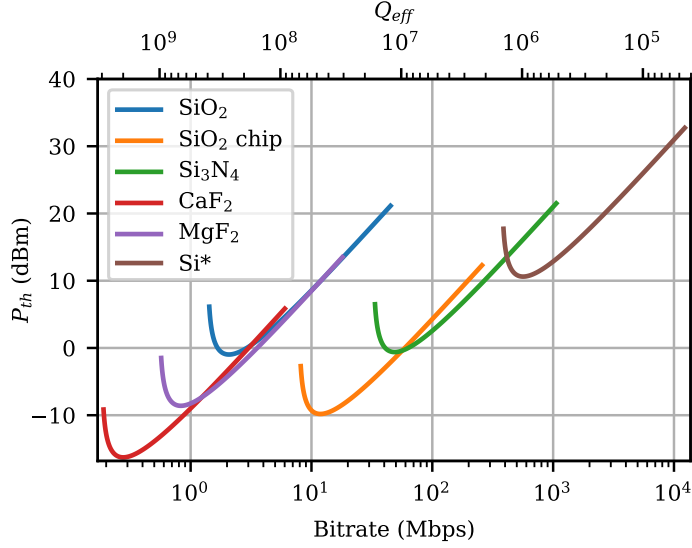


Figure 5.16: Expected bitrate and threshold power for different materials. *Only for silicon a wavelength of $3.1\ \mu\text{m}$ is used instead of $1.55\ \mu\text{m}$. Adapted from [52].

Table 5.1: Parameters used for the simulation in Fig. 5.16. A_{eff} is the effective mode area, n is the refractive index, n_2 is the nonlinear refractive index, and Q_0 is the intrinsic Q-factor. The values for silicon are reported at $3.1\ \mu\text{m}$, since it is not transparent at $1.55\ \mu\text{m}$. Adapted from [52].

Material	diam.	A_{eff}	n [151]	n_2 [cm^2/W]	Q_0
SiO ₂ rod	2 mm	$50\ \mu\text{m}^2$	1.444 [115]	2.7×10^{-16} [37]	4×10^8
SiO ₂ toroid	100 μm	$4\ \mu\text{m}^2$	1.444 [115]	2.7×10^{-16}	7×10^7
Si ₃ N ₄ [92]	600 μm	$1\ \mu\text{m}^2$	2.463 [152]	2.4×10^{-15}	1.7×10^7
CaF ₂ [153]	6 mm	$20\ \mu\text{m}^2$	1.426 [117]	1.9×10^{-16}	3×10^9
MgF ₂ [153]	2 mm	$20\ \mu\text{m}^2$	1.37 [116]	9×10^{-17}	1×10^9
Si* [161]	100 μm	$1\ \mu\text{m}^2$	3.43 [162]	1.7×10^{-14} [163]	7×10^5

because the material is not transparent at this wavelength. The parameters used to plot Fig. 5.16 are reported in Table 5.1.

Note how each curve presents the same shape in a log-log plot. The bottom of the curve represents the optimal coupling for energy efficiency, which is very close to critical coupling. As the coupling is reduced, a smaller fraction of the input light gets into the resonator increasing the required input power. This happens because the Q-factor cannot increase past the intrinsic Q factor. On the other side, if the input waveguide is strongly over-coupled the Q factor is reduced and the bitrate increases since light can get into or leak out of the resonator faster. However, the same leaks prevent the power build-up in the resonator requiring again more input power. It is

unrealistic to extend the curves on the right for too long because achieving strong over-coupling with tapered fibres requires strong overlap between the resonator and the taper evanescent fields, but this is possible just up to a certain extent. With waveguides instead, it would be possible to physically overlap the two.

Materials that can be fabricated with really high intrinsic Q-factors, such as CaF_2 and MgF_2 can extend the minimum working power down to less than 100 μW but they do not provide significant performances in terms of bitrate. On the other hand, materials with higher nonlinearity and can be fabricated with techniques that allow smaller mode volume show promising results in terms of bitrate, potentially reaching 10 Gbps.

5.6 Alternative technologies

Now that the mechanism of switching has been analysed in-depth let us move on the alternative technologies to realise bistable optical devices. As mentioned in the introduction, photonic circuits are an active topic of research. The main drive of this field is to overcome some of the limitations of the electronics circuits, propose an alternative technology for information transfer and processing, and finally to realise new kind of devices such as lab-on-a-chip. In this section I do not focus on the electronic devices but only on the data processing with optical means.

The control of light in waveguides is usually performed through devices that require an input different from light. As an example, in this experiment, I use EOMs and tested AOMs to modulate the amplitude of light. The working principle is different but both can reach modulation speeds of the order of hundreds of MHz in the case of AOMs and tens of GHz for EOMs. In the case of an EOM, different configurations can modulate not only the amplitude but also the frequency, phase and polarization of the light. An example is the quadrature phase-shift keying (QPSK) modulator that I used improperly in [120] to directly measure the Kerr shift in microresonators.

Another approach is to mechanically control the waveguide through micro-electro-mechanical systems (MEMS). These devices are easily integrated on-chip by using a microfabrication procedure similar to the one described in Chapter 2 for the microtoroid resonators. Oxidation of silicon is used to create the moving parts, then HF etching cut the geometry to shape and XeF_2 removes completely the silicon

from underneath the mechanism to make it free to move. In addition, conductive layers are applied to drive the motion with the application of potential differences. MEMS are used in a plethora of different geometries [164], and they can cover some of the application I showed for our device such as switches, by misaligning part of a waveguide, or tuning a racetrack resonator [165]. The driving of these structures does not need to be electric: as an example, thermal solutions have been proposed [166] but they result in a slower response.

All the devices mentioned so far require some form of electric input to work, let us move to all-optical devices. Even restricting the field to devices controlled only by light, the possible solutions are several [167]. Most of them are based on some form of nonlinear response of the optical media. Some examples consist of bistable changes in the material deposited on top of the waveguide [168]. Already in 1987, [169] used nonlinear coupling in a dual-core fibre to selectively couple light between the two cores depending on the optical power. Most of these applications require a configuration with two different laser frequencies to be used in a pump and probe configuration [170, 171]. An advantage of the solution presented in this chapter is that it requires a single wavelength for programming and reading the state of the device. The use of third-order Kerr nonlinearity, in general, allows fast switching because the response time of the device is almost instantaneous [172]. However, the light needs to be concentrated enough.

Encoding the state in the mode selection of multimode laser is used to generate extremely fast transition due to the gain of the system [173]. In particular ring lasers, with their two directions of lasing proved to be an ideal candidate for bandwidth above the GHz [174, 175, 176, 177]. The ring laser concept is similar to the experiment in this chapter: a nudge to the ring resonator sets the circulation direction to the corresponding direction. The physics, however, is completely different. In ring lasers, the direction with higher intensity takes over because of gain saturation for the other direction and the device is not passive since it requires pumping either electrically through carrier injection or optically through an additional laser at a different wavelength.

So far I mentioned active devices. Moving to the passive solution, photonic crystal cavities are the natural alternative to microresonators to concentrate the light and exploit nonlinear effects [178, 179, 180, 181, 182, 183]. Their mode volume can be smaller than whispering gallery modes resonators and waveguide resonator. As

we saw earlier, reducing the mode volume gives flexibility in terms of performance, either by reducing the threshold power for the same bitrate or by increasing the bitrate for the same input power. However, the thermal effects tend to detune the cavities making them unable to retain the state for a long time and affecting the stability in general.

Semiconductor resonators add yet another nonlinear effect to the mix; on top of the Kerr effect and the thermal effects, semiconductors show two-photon absorption (TPA), i.e. the conversion of two circulating photons in a carrier pair [184, 185, 178]. This is not only a nonlinear losses mechanism but also the carrier concentration contributes to the change in refractive index. This effect is also used to achieve bistability in nonresonant devices [186, 187]. The interplay between the three sources of nonlinearity, namely thermal [185], Kerr [188], and TPA leads to instabilities due to their different timescale. Hence, most of the work using semiconductors aims to exploit just one of the three effects, mitigating the contributions from the other two. Most of the work using nonlinearities exploits the s-shape response of the intra-cavity power with respect to the input power [189, 190]. This is a characteristic of frequency shifting nonlinearities in resonant structures and it is observable also in the device presented in this chapter. However, our device is used at higher power compared to the s-shaped region. This is surely a disadvantage for the power requirements but the symmetry-broken region extends in a much broader range of input power and detuning, improving the usage envelope and the resilience to noise.

5.7 Applications

5.7.1 Memory

The resonator maintains the state if the input power is equal and the average power and detuning are in the symmetry-broken region. If we assign the value of 1 and 0 to the two directions of circulation, it is clear how information can be stored as the circulation direction of light. The information is stored as long as the resonator is held in the symmetry broken region, i.e. as long as it is “powered”.

To modify the information one can act on both the input taper by changing the power imbalance but this is not necessary. An alternative is to have the two inputs with equal power in the resting state and modulate just one of them by

A	B	$A \& B$
0	0	0
0	1	0
1	0	0
1	1	1

Table 5.2: *Truth table of the logic operation A and B*

increasing and decreasing its power. Sending a power surge will set the resonator in the corresponding direction, a power decrease will set the opposite direction.

The information stored in the resonator can be read continuously, without destroying the stored information, by looking at the power coming back from the input taper or alternatively using a second taper to monitor the circulating power.

5.7.2 Router or switch

The device configured with two tapers can be used also to route light in different directions. Let us recall the two tapers configuration in Section 4.1. A resonant light input at port 1 it will reach port 2 if it is the only light in the system. To use the device as a switch we can connect the control input to port 2. If there is no control input, the signal will not continue in the input taper but, if the control light is switched on at a power higher than the signal, the resonator will not allow light in from port 1 and transmit it to port 4 instead.

The same situation can be imagined as a router. The device at port 2 will be outputting power at idle, letting the signal go through the bus $1 \rightarrow 3$. If the device wants to receive the information it switches off its output and the bus is redirected to port 2. This approach could be used to realise devices such as [191] but with optical inputs instead of electrical.

5.7.3 Logic gate

This idea of switching can be pushed forward to realise a logic gate. By appropriately driving the inputs, the output at one port is a logic combination of the inputs.

The A and B gate

An $A \& B$ gate outputs LOW unless both the inputs are HIGH. This can be realised

A	B	$A\&\bar{B}$
0	0	0
0	1	0
1	0	1
1	1	0

Table 5.3: *Truth table of the logic operation A AND (NOT B)*

with the dual taper configuration by using ports 1 and 4 as the A and B inputs and connecting ports 2 and 3 on the same side of a directional coupler.

The logic levels are encoded as follows. The LOW state corresponds to 0 optical power and the HIGH state is an input power high enough to access the symmetry broken region. If both the inputs are LOW, there is no light in the setup so the output is LOW. If only one of the two input is HIGH, the light will couple in the resonator and leave it from the other input without reaching the output. Finally, when both inputs are HIGH, only one of the two will couple to the resonator due to the symmetry breaking, while the other will stay in the taper and reach the output.

The $A \& \bar{B}$ gate

The $A \& B$ gate is not universal. This means that it is not possible to realise any logic function combining a series of these logic gates with additional fixed inputs [192]. The typical example of a universal logic gate is the NAND (i.e. an AND gate followed by a NOT gate), probably because the transistor-based electronics uses this gate to build all the other ones. Other universal logic gates are the NOR and the far less known AND NOT. Why am I citing a forgotten universal gate? Because it is the one that is easily implemented with a microresonator. Let us have a look at the truth table:

This idea has been formalised into a paper [53] by my colleague Niall Moroney and myself. The setup for the experiment is the same used for the switching. I mainly outlined the setup, performed the simulations and prepared the test signals while Niall took the experimental measures analysed the data and wrote the paper.

Working principle

Let us analyse how to realise the truth table 5.3 above in the two taper configuration. From line 3 we understand that A alone should propagate through the device hence referring to the port naming we adopted, port 1 is going to be the input A and port

2 is going to be the output. Lines 2 and 4 tell us that the input B should never reach the output and switch the output LOW even if A is HIGH. This suggests that B has to be counter-propagating to A and have a higher HIGH level to overcome the hysteresis. Since port 2 is already used as the output we will use port 4 as the B input.

In this case the logic levels are encoded as:

$$\begin{aligned}\tilde{p}_A &= P_m A \\ \tilde{p}_B &= P_m B + \xi\end{aligned}\tag{5.20}$$

Where A, B represent the logic state 0 and 1, P_m is the modulation power and ξ is the offset in units of P_m .

An intuitive representation of why an offset is needed. One can think of the light inputs competing to get control of the resonator. However, we do not want the inputs to behave symmetrically: B should be able to overcome the hysteresis and “kick out” A from the resonator while the opposite should not be true. Let us now prepare a test for this device.

Analysis of all the possible switching combinations

In designing the test routine it is important to remember that an increase in the input power in one direction causes a different change in the circulating power if the resonance for that direction is shifted or not by the cross-phase modulation. In other words, looking back at Chapter 3 we saw that for the same combination of input power and detuning there are multiple possible states of the resonator hence, to verify that the device is working, one needs to test not only all the 4 possible combinations of the inputs but all the possible transition to those combinations. At each transition, the signal in each direction can stay HIGH or stay LOW, go HIGH, or go LOW.

I designed the test signal shown in Fig. 5.17 that makes it possible to analyse all 16 possible types of transitions. Panel (a) shows why this test is important. The logic gate output is supposed to be HIGH only when A is HIGH and B is LOW but this is not the case between $t = 30 \mu\text{s}$ and $t = 40 \mu\text{s}$. This happens because direction A is coupled into the resonator and the power increase in the B direction is not enough to cause a switching due to the hysteresis. The same state accessed from

both directions being LOW or from B staying in the HIGH state produces the correct output of LOW. To ensure the functionality of the logic gate, the B input power levels need an offset by the intermediate power of direction A . If the offset is too low, the particular transition analysed above does not produce the correct output (Fig. 5.17(a)). If the offset is too high, the output will never go HIGH (Fig. 5.17(c)).

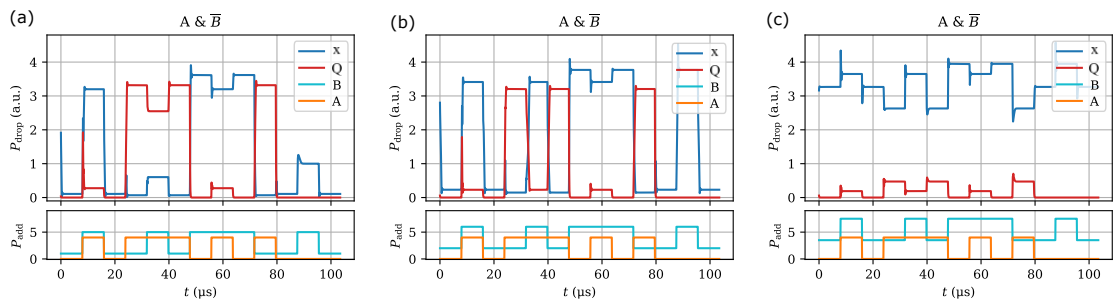


Figure 5.17: Simulation of the logic gate $A \& \bar{B}$. The lower part of each panel shown the inputs A and B , while the upper part shows the output Q and the other circulating direction, not used in the logic gate x . The value of ξ for each panel is $0.2(a)$, $0.5(b)$, $0.8(c)$.

Increasing the input power or detuning the laser deeper into the symmetry broken region may prevent switching due to the too high hysteresis. Indeed, it is not even needed to set the resonator in the symmetry broken region because the Kerr effect is present even at lower circulating power, the only drawback of operating at low power is the significant reduction of the contrast between the HIGH and LOW power levels. We experimentally tested this logic gate as shown in Fig. 5.18.

Note that the output correctly rises only when the inputs are $A = 1$ and $B = 0$. When B is HIGH, the transmission of the input A to the output is attenuated by 11 dB.

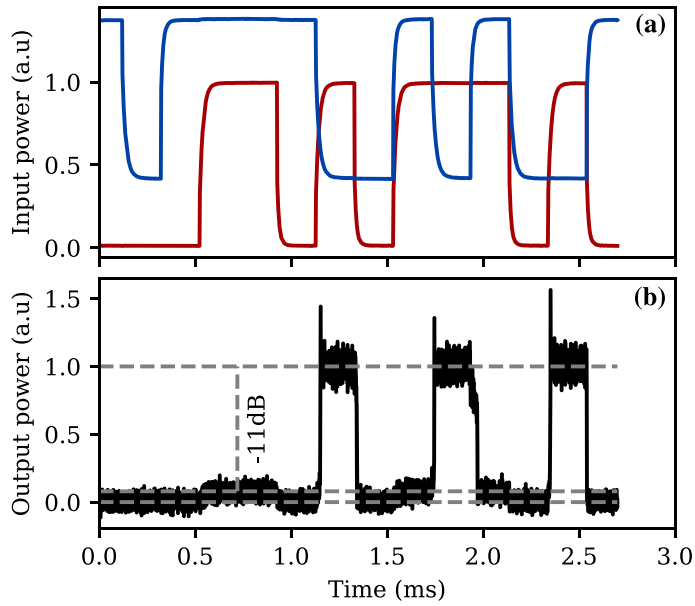


Figure 5.18: *Experimental results of the logic gate setup. Panel (a) shows the input powers A in red and B in blue, panel (b) shows the output. Adapted from [53].*

5.8 Conclusions

In this chapter, I showed how the direction of light circulating in a microresonator can be controlled via the input powers in each direction. Once the microresonator is set in the symmetry-broken regime by applying light input with power and detuning, it behaves as a bistable device. Multi-stability is the key feature of any digital device. In particular, I showed that it is possible to use the microresonator for information storage and processing by encoding the digital values 0 and 1 to the circulating directions CW and CCW. The resonator holds the state as long as the input light is on and the “optical memory” can be programmed by the light input. Furthermore, it is possible to implement digital signal processing by connecting the inputs appropriately. This method provides a passive, all-optical technique for the realisation of several elements at the foundations of optical computing.

The theoretical and experimental study of the dynamics of the symmetry broken state also led to the observations of two other effects. The critical slowing down of the system close to the symmetry breaking point [159], and the onset of a spontaneous dynamics [121, 122].

Chapter 6

Conclusions and outlook

6.1 Summary

In this thesis, I described the Kerr effect for counter-propagating light in a microresonator. Specifically, I described a theoretical model for the propagation of light in microresonators and the Kerr interaction both in the stationary and dynamic case. Then I presented the fabrication techniques for the experimental setup and three main experiments that exploit this effect. The first experiment showed how the Kerr interaction leads to symmetry breaking in the resonator, the second one exploited the symmetry-broken states to achieve non-reciprocal optical propagation and the third analysed how it is possible to switch between the states and the dynamics of the process.

6.2 Outcomes

The following points outline the main findings and results of this thesis.

I developed a complete mathematical model for the Kerr-mediated interaction between counter-propagating light in a ring resonator starting from a linear model of a ring resonator [66]. The model has been tailored to describe high-Q-factor microresonators in the steady-state as follows. First, an exact model is derived from the resonator and coupling characteristics and successively approximated for the conditions of high Q-factor. Then the model is expressed in terms of measurable quantities, by applying their definitions. Finally, after adding the Kerr effect as a power-dependent detuning, a suitable normalisation is implemented to obtain

dimensionless quantities that are both agile to use in computer simulations and provide a general description independent from the specific properties of the resonator used in the experiment.

I developed an additional model for the dynamic state as a special case of the Lugiato-Lefever equation that describes the dynamics of the light of the resonator during the transients and converges to the stationary model in the steady-state.

The symmetry breaking and the related applications are not affected by the thermal effects. Despite contributing to the resonance detuning about two orders of magnitude more than the Kerr effect, the thermal effects are equal for both directions hence they do not cause any resonance splitting. Therefore it is possible to exploit the thermal effects as a proportional feedback loop to lock the frequency of the resonator to the laser with a capture range of several GHz and a bandwidth over several tens of kHz ¹

I showed symmetry breaking of counter-propagating light in microresonators for the first time.

I demonstrated an all-optical isolator and circulator based on the Kerr nonreciprocity with an isolation up to 25 dB and insertion losses as low as 3 dB.

I have shown fabrication techniques for all the key components in the setup. The tapered optical fibres are fabricated by pulling a single-mode optical fibre using either a ceramic heater or a hydrogen flame. The fused silica resonators used in this thesis are fabricated from a glass rod ablated by a CO₂ laser. The microtoroids and microdisks are fabricated through photolithographic techniques.

I developed a new technique (to the best of my knowledge) to repurpose EOMs, designed for side-band generation, for arbitrary waveform amplitude modulation overcoming the intrinsic slow time constant of the device. This is achieved by analysing the response of the EOM and producing an over-driven input signal that compensates for the slow part of the response. This technique reduced the rise time of the EOMs from several μ s to 8 ns (with a driving signal rise time of 5 ns).

I demonstrated how the bistability induced by the Kerr interaction between counter-propagating light constitutes a new approach to bistable photonic devices such as optical memories, switches, routers and logic gates. It is possible to switch between the symmetry-broken states by an appropriate control of the inputs. The

¹These are typical values. Depending on the geometry and type of the resonator these may change by an order of magnitude.

intrinsic resonant structure imposes a trade-off between the switching speed and the power required. This technique has the advantage of being all-optical and completely passive, furthermore, the devices realised with this technique are noise resilient and do not suffer from limited holding time since they hold the state as long as the input light is on.

6.3 Outlook

In the experiments presented in this thesis and others performed in my research group, we used external lasers to pump the microresonators. An interesting avenue to pursue is to introduce gain via erbium doping either in the tapered fibre or in the microresonator. This would provide a new ground for the study of non-hermitian PT-symmetric systems. The introduction of gain also provides technical advantages such as increased Q-factor due to the compensation of losses in the resonator or the possibility to use the resonator as the laser cavity, eliminating the need for any form of frequency locking. A first experiment in this direction produced interesting effects as we found out in a collaboration with the University of Sussex [193]. The experiment consisted in coupling the resonator inside an erbium-doped fibre laser operating in continuous wave. The paper presents the dynamics caused by the interplay of the thermal effect with the two cavity resonances that deserve further investigation together with the case where the thermal effect contribution is minimised.

Another planned experiment involves the case where the fibre laser is constituted by a laser cavity where the gain medium is enclosed on one side by a standard mirror and, on the other, by a microresonator that provides injection locking through backscattering. This configuration could, in principle, replace the ECDL tunable laser with a much simpler and cheaper 980 nm diode laser pump. The resonant radiation would be intrinsically resonant with the microresonator because the laser cavity would be closed just at that frequency.

Finally, doping the resonator itself to introduce gain, would provide a mechanism to compensate for losses when multiple resonators are chained together, not to mention also the possibility of studying the physics of gain ($\alpha > 1$ as described in Chapter 2).

As presented in Chapters 4 and 5, the fused silica rod resonators provide an

exceptional platform for proof-of-principle experiments thanks to fast fabrication turnaround and their high Q factor that allows testing the dynamic characteristics without using equipment that may not be present in a photonics laboratory. However, it is undeniable that a commercial device would require much higher speed and lower power thresholds than the ones demonstrated in this thesis. Hence, one of my future works is continuing the development of micro-fabrication techniques for microresonators. The latest results with fused silica toroids that I fabricated with my colleagues [120] showed a reduction of the characteristic power of a factor of 100 compared to silica rods. This mostly arises from the smaller mode area and the smaller diameter since the Q-factor is of the same order of magnitude and the material is the same. To further reduce the power requirements and footprint improve the switching speed, I will investigate the use of other materials. The choice of materials is fundamentally limited by their transparency at the wavelength of interest and their nonlinear refractive index. But in practice, the scattering introduced by surface roughness is currently the limiting factor preventing the use of several materials. The availability of suitable machinery for fabrication and growth in the cleanroom, and the development of procedures to obtain a smooth surface are crucial to proceed in this direction. Silicon nitride (Si_3N_4) is an ideal candidate for non-reciprocity application given that its n_2 is 10 times higher than fused silica and the fabrication of high-Q ring cavities has already been demonstrated [194].

Another challenge in the microfabrication would be to integrate the waveguides on the same chip as the resonator. This is an existing technique [92, 134] that would greatly reduce the size of the setup allowing integration [195] not to mention the reduction in the phase noise coming from thermal expansion and the mechanical forces on the optical fibres as observed in [196]. An alternative solution is presented in [197, 154], where instead of building all the setup on the same chip, they realise optical interconnects between different chips.

The results in this thesis are all based on a single laser input. Using an additional laser, we obtained promising results for the stabilization of frequency combs in microresonators [23]. The same technique can be used as a means of tuning the resonator in the case of counter-propagating light since an auxiliary beam at a different frequency interacts via XPM with both directions. But it also opens new avenues where the Kerr interaction involves more than just two propagating directions.

Bibliography

- [1] John Kerr. “XL. A new relation between electricity and light: Dielectrified media birefringent”. In: *The London, Edinburgh, and Dublin Philosophical Magazine and Journal of Science* 50.332 (Nov. 1875), pp. 337–348. DOI: 10.1080/14786447508641302.
- [2] John Kerr. “LIV. A new relation between electricity and light: Dielectrified media birefringent (Second paper)”. In: *The London, Edinburgh, and Dublin Philosophical Magazine and Journal of Science* 50.333 (Dec. 1875), pp. 446–458. DOI: 10.1080/14786447508641319.
- [3] Robert W. Boyd and Debbie Prato. *Nonlinear Optics*. Elsevier Science, May 13, 2008. 640 pp.
- [4] Bruce A. Garetz. “The Kerr effect”. In: *Optics News* 12.10 (Oct. 1986), p. 28. DOI: 10.1364/on.12.10.000028.
- [5] E. Cumberbatch. “Self-focusing in Non-linear Optics”. In: *IMA Journal of Applied Mathematics* 6.3 (1970), pp. 250–262. DOI: 10.1093/imamat/6.3.250.
- [6] G. P. Agrawal. *Nonlinear Fiber Optics*. Academic Press, 2006.
- [7] R. H. Stolen and Chinlon Lin. “Self-phase-modulation in silica optical fibers”. In: *Physical Review A* 17.4 (Apr. 1978), pp. 1448–1453. DOI: 10.1103/physreva.17.1448.
- [8] George Gabriel Stokes. “On the theory of oscillatory waves”. In: *Transactions of the Cambridge Philosophical Society* 8 (1847), pp. 441–455.
- [9] Thomas B. Benjamin, K. Hasselmann, and Michael James Lighthill. “Instability of periodic wavetrains in nonlinear dispersive systems”. In: *Proceedings of the Royal Society of London. Series A. Mathematical and Physical Sciences* 299.1456 (June 1967), pp. 59–76. DOI: 10.1098/rspa.1967.0123.

- [10] H. C. Yuen and B. M. Lake. “Instabilities of Waves on Deep Water”. In: *Annual Review of Fluid Mechanics* 12.1 (Jan. 1980), pp. 303–334. DOI: 10.1146/annurev.fl.12.010180.001511.
- [11] Peter A. E. M. Janssen. “Nonlinear Four-Wave Interactions and Freak Waves”. In: *Journal of Physical Oceanography* 33.4 (Apr. 2003), pp. 863–884. DOI: 10.1175/1520-0485(2003)33<863:nfiafw>2.0.co;2.
- [12] S. Trillo and S. Wabnitz. “Dynamics of the nonlinear modulational instability in optical fibers”. In: *Optics Letters* 16.13 (July 1991), p. 986. DOI: 10.1364/ol.16.000986.
- [13] Andrey B. Matsko et al. “Optical hyperparametric oscillations in a whispering-gallery-mode resonator: Threshold and phase diffusion”. In: *Physical Review A* 71.3 (Mar. 2005). DOI: 10.1103/physreva.71.033804.
- [14] A. B. Matsko et al. “Hard and soft excitation regimes of Kerr frequency combs”. In: *Physical Review A* 85.2 (Feb. 2012). DOI: 10.1103/physreva.85.023830.
- [15] T. Hansson, D. Modotto, and S. Wabnitz. “Dynamics of the modulational instability in microresonator frequency combs”. In: *Physical Review A* 88.2 (Aug. 2013). DOI: 10.1103/physreva.88.023819.
- [16] Lord Rayleigh. “The problem of the whispering gallery”. In: *The London, Edinburgh, and Dublin Philosophical Magazine and Journal of Science* 20.120 (Dec. 1910), pp. 1001–1004. DOI: 10.1080/14786441008636993.
- [17] R. D. Richtmyer. “Dielectric Resonators”. In: *Journal of Applied Physics* 10.6 (June 1939), pp. 391–398. DOI: 10.1063/1.1707320.
- [18] V.B. Braginsky, M.L. Gorodetsky, and V.S. Ilchenko. “Quality-factor and nonlinear properties of optical whispering-gallery modes”. In: *Physics Letters A* 137.7-8 (May 1989), pp. 393–397. DOI: 10.1016/0375-9601(89)90912-2.
- [19] Guoping Lin, Aurélien Coillet, and Yanne K. Chembo. “Nonlinear photonics with high-Q whispering-gallery-mode resonators”. In: *Advances in Optics and Photonics* 9.4 (Nov. 2017), p. 828. DOI: 10.1364/aop.9.000828.
- [20] P. Del’Haye, S. A. Diddams, and S. B. Papp. “Laser-machined ultra-high-Q microrod resonators for nonlinear optics”. In: *Applied Physics Letters* 102 (2013), p. 221119.

- [21] Ki Youl Yang et al. “Integrated Ultra-High-Q Optical Resonator”. In: *ArXiv* (Feb. 16, 2017). arXiv: 1702.05076v3 [physics.optics].
- [22] J. Hofer, A. Schliesser, and T. J. Kippenberg. “Cavity optomechanics with ultrahigh-Q crystalline microresonators”. In: *Physical Review A* 82.3 (2010), p. 031804. DOI: 10.1103/PhysRevA.82.031804.
- [23] Shuangyou Zhang et al. “Sub-milliwatt-level microresonator solitons with extended access range using an auxiliary laser”. In: *Optica* 6.2 (Feb. 2019), p. 206. DOI: 10.1364/optica.6.000206.
- [24] P. Del’Haye et al. “Optical frequency comb generation from a monolithic microresonator”. In: *Nature* 450.7173 (Dec. 2007), pp. 1214–1217. DOI: 10.1038/nature06401.
- [25] T. J. Kippenberg, R. Holzwarth, and S. A. Diddams. “Microresonator-Based Optical Frequency Combs”. In: *Science* 332.6029 (Apr. 2011), pp. 555–559. DOI: 10.1126/science.1193968.
- [26] A. V. Gaponov, L. A. Ostrovskii, and G. I. Freidman. “Electromagnetic shock waves”. In: *Radiophysics and Quantum Electronics* 10.9-10 (1971), pp. 772–793. DOI: 10.1007/bf01031606.
- [27] V. I. Bespalov and V. I. Talanov. “Filamentary Structure of Light Beams in Nonlinear Liquids”. In: *Soviet Journal of Experimental and Theoretical Physics Letters* 3 (June 1966), p. 307.
- [28] T. J. Kippenberg, S. M. Spillane, and K. J. Vahala. “Kerr-nonlinearity Optical Parametric Oscillation in an Ultrahigh-Q Toroid Microcavity”. In: *Physical Review Letters* 93.8 (Aug. 2004). DOI: 10.1103/physrevlett.93.083904.
- [29] Anatoliy A. Savchenkov et al. “Low Threshold Optical Oscillations in a Whispering Gallery Mode CaF₂ Resonator”. In: *Physical Review Letters* 93.24 (Dec. 2004). DOI: 10.1103/physrevlett.93.243905.
- [30] Pascal Del’Haye. “Optical Frequency Comb Generation in Monolithic Microresonators”. PhD thesis. Ludwig Maximilians Universitat Munchen, 2011.
- [31] T. Herr et al. “Temporal solitons in optical microresonators”. In: *Nature Photonics* 8.2 (Dec. 2013), pp. 145–152. DOI: 10.1038/nphoton.2013.343.

- [32] L. A. Lugiato and R. Lefever. “Spatial Dissipative Structures in Passive Optical Systems”. In: *Physical Review Letters* 58.21 (May 1987), pp. 2209–2211. DOI: 10.1103/physrevlett.58.2209.
- [33] Nathalie Picqué and Theodor W. Hänsch. “Frequency comb spectroscopy”. In: *Nature Photonics* 13.3 (Feb. 2019), pp. 146–157. DOI: 10.1038/s41566-018-0347-5.
- [34] Tara Fortier and Esther Baumann. “20 years of developments in optical frequency comb technology and applications”. In: *Communications Physics* 2.1 (Dec. 2019). DOI: 10.1038/s42005-019-0249-y.
- [35] L. Razzari et al. “CMOS-compatible integrated optical hyper-parametric oscillator”. In: *Nature Photonics* 4.1 (Jan. 2010), pp. 41–45. ISSN: 1749-4885. DOI: 10.1038/nphoton.2009.236.
- [36] Charlie E. M. Strauss. “Synthetic-array heterodyne detection: a single-element detector acts as an array”. In: *Optics Letters* 19.20 (Oct. 1994), p. 1609. DOI: 10.1364/ol.19.001609.
- [37] T. Kato et al. “Measurement of the nonlinear refractive index in optical fiber by the cross-phase-modulation method with depolarized pump light”. In: *Opt. Lett.* 20.9 (May 1995), pp. 988–990. DOI: 10.1364/ol.20.000988.
- [38] Govind P. Agrawal. “Modulation instability induced by cross-phase modulation”. In: *Physical Review Letters* 59.8 (Aug. 1987), pp. 880–883. DOI: 10.1103/physrevlett.59.880.
- [39] A. E. Kaplan and P. Meystre. “Directionally asymmetrical bistability in a symmetrically pumped nonlinear ring interferometer”. In: *Optics Communications* 40.3 (1982), pp. 229–32. DOI: 10.1016/0030-4018(82)90267-X.
- [40] A. E. Kaplan and P. Meystre. “Enhancement of the Sagnac effect due to nonlinearly induced nonreciprocity”. In: *Optics Letters* 6.12 (Dec. 1981), p. 590. DOI: 10.1364/ol.6.000590.
- [41] S. Ezekiel, R. W. Hellwarth, and J. L. Davis. “Observation of intensity-induced nonreciprocity in a fiber-optic gyroscope”. In: *Optics Letters* 7.9 (Sept. 1982), p. 457. DOI: 10.1364/ol.7.000457.

- [42] Qi-Fan Yang et al. “Counter-propagating solitons in microresonators”. In: *Nature Photonics* 11.9 (Aug. 2017), pp. 560–564. DOI: 10.1038/nphoton.2017.117.
- [43] Douglas Adams. *The Hitchhiker’s Guide to the Galaxy*. Pan Books, 1979. ISBN: 0-330-25864-8.
- [44] Chaitanya Joshi et al. “Counter-rotating cavity solitons in a silicon nitride microresonator”. In: *Optics Letters* 43.3 (Jan. 2018), p. 547. DOI: 10.1364/ol.43.000547.
- [45] Xu Yi et al. “Active capture and stabilization of temporal solitons in microresonators”. In: *Optics Letters* 41.9 (Apr. 2016), p. 2037. DOI: 10.1364/ol.41.002037.
- [46] Peter W. Higgs. “Broken Symmetries and the Masses of Gauge Bosons”. In: *Physical Review Letters* 13.16 (Oct. 1964), pp. 508–509. DOI: 10.1103/physrevlett.13.508.
- [47] Georges Sagnac. “L’*é*ther lumineux démontré par l’effet du vent relatif d’*é*ther dans un interféromètre en rotation uniforme”. In: *Comptes Rendus* 157 (1913), pp. 708–710.
- [48] Georges Sagnac. “Sur la preuve de la réalité de l’*é*ther lumineux par l’expérience de l’interféromètre tournant”. In: *Comptes Rendus* 157 (1913), pp. 1410–1413.
- [49] Jonathan Silver, Leonardo Del Bino, and Pascal Del’Haye. “A nonlinear enhanced microresonator gyroscope”. In: *2017 Conference on Lasers and Electro-Optics Europe & European Quantum Electronics Conference (CLEO/Europe-EQEC)*. IEEE, June 2017. DOI: 10.1109/cleoe-eqec.2017.8086527.
- [50] Andreas Ø. Svela et al. “Spontaneous Symmetry Breaking Based Near-Field Sensing with a Microresonator”. In: *Conference on Lasers and Electro-Optics*. OSA, 2019. DOI: 10.1364/cleo_at.2019.jm3b.3.
- [51] Leonardo Del Bino et al. “Microresonator isolators and circulators based on the intrinsic nonreciprocity of the Kerr effect”. In: *Optica* 5.3 (2018), pp. 279–282. DOI: 10.1364/OPTICA.5.000279.

- [52] Leonardo Del Bino, Niall Moroney, and Pascal Del’Haye. “Optical memories and switching dynamics of counterpropagating light states in microresonators”. In: (Feb. 7, 2020). arXiv: <http://arxiv.org/abs/2002.02954v1> [physics.optics].
- [53] Niall Moroney et al. “Logic Gates Based on Interaction of Counterpropagating Light in Microresonators”. In: *Journal of Lightwave Technology* 38.6 (Mar. 2020), pp. 1414–1419. DOI: 10.1109/jlt.2020.2975119.
- [54] *Photonics Market*. Prescient and Strategic Intelligence Private Limited. Feb. 2020.
- [55] Max Born and Emil Wolf. *Principles of Optics: Electromagnetic Theory of Propagation, Interference and Diffraction of Light*. Cambridge University Press, 1999. ISBN: 978-0521642224.
- [56] Xiangyi Xu et al. “Phone-sized whispering-gallery microresonator sensing system”. In: *Optics Express* 24.23 (Oct. 2016), p. 25905. DOI: 10.1364/oe.24.025905.
- [57] Yanyan Zhi et al. “Single Nanoparticle Detection Using Optical Microcavities”. In: *Advanced Materials* 29.12 (Jan. 2017), p. 1604920. DOI: 10.1002/adma.201604920.
- [58] Andreas Ø. Svela et al. “Coherent suppression of backscattering in optical microresonators”. In: (Feb. 27, 2020). arXiv: <http://arxiv.org/abs/2002.12379v1> [physics.optics].
- [59] Hermann A. Haus. *Waves and Fields in Optoelectronics (Prentice-Hall series in solid state physical electronics)*. Prentice Hall, 1983. ISBN: 0-13-946053-5.
- [60] C. A. Millar, M. C. Brierley, and S. R. Mallinson. “Exposed-core single-mode-fiber channel-dropping filter using a high-index overlay waveguide”. In: *Optics Letters* 12.4 (Apr. 1987), p. 284. DOI: 10.1364/ol.12.000284.
- [61] M. L. Gorodetskii et al. “High-Q Factor Optical Whispering-Gallery Mode Microresonators and Their Use in Precision Measurements”. In: *Measurement Techniques* 57.12 (Mar. 2015), pp. 1386–1395. DOI: 10.1007/s11018-015-0639-9.

- [62] Vladimir S. Ilchenko et al. “Nonlinear Optics and Crystalline Whispering Gallery Mode Cavities”. In: *Physical Review Letters* 92.4 (Jan. 2004). DOI: 10.1103/physrevlett.92.043903.
- [63] J. C. Knight et al. “Phase-matched excitation of whispering-gallery-mode resonances by a fiber taper”. In: *Optics Letters* 22.15 (Aug. 1997), p. 1129. DOI: 10.1364/ol.22.001129.
- [64] S. M. Spillane et al. “Ideality in a Fiber-Taper-Coupled Microresonator System for Application to Cavity Quantum Electrodynamics”. In: *Physical Review Letters* 91.4 (July 2003). DOI: 10.1103/physrevlett.91.043902.
- [65] Martin H. P. Pfeiffer et al. “Coupling Ideality of Integrated Planar High-Q Microresonators”. In: *Physical Review Applied* 7.2 (Feb. 2017). DOI: 10.1103/physrevapplied.7.024026.
- [66] Dominik G. Rabus. *Integrated Ring Resonators, the compendium*. Optical sciences. Springer, 2007. ISBN: 978-3-540-68786-3.
- [67] Ming Cai, Oskar Painter, and Kerry J. Vahala. “Observation of Critical Coupling in a Fiber Taper to a Silica-Microsphere Whispering-Gallery Mode System”. In: *Physical Review Letters* 85.1 (July 2000), pp. 74–77. DOI: 10.1103/physrevlett.85.74.
- [68] M. L. Gorodetsky, A. A. Savchenkov, and V. S. Ilchenko. “Ultimate Q of optical microsphere resonators”. In: *Optics Letters* 21.7 (Apr. 1996), p. 453. DOI: 10.1364/ol.21.000453.
- [69] D. W. Vernooy et al. “High-Q measurements of fused-silica microspheres in the near infrared”. In: *Optics Letters* 23.4 (Feb. 1998), p. 247. DOI: 10.1364/ol.23.000247.
- [70] D. S. Weiss et al. “Splitting of high-Q Mie modes induced by light backscattering in silica microspheres”. In: *Optics Letters* 20.18 (Sept. 1995), p. 1835. DOI: 10.1364/ol.20.001835.
- [71] S. M. Spillane, T. J. Kippenberg, and K. J. Vahala. “Ultralow-threshold Raman laser using a spherical dielectric microcavity”. In: *Nature* 415.6872 (Feb. 2002), pp. 621–623. DOI: 10.1038/415621a.

- [72] I. S. Grudinin, N. Yu, and L. Maleki. “Generation of optical frequency combs with a CaF₂ resonator”. In: *Optics Letters* 34.7 (2009), pp. 878–880. DOI: 10.1364/OL.34.000878.
- [73] A. V. Cherenkov et al. “Raman-Kerr frequency combs in microresonators with normal dispersion”. In: *Optics Express* 25.25 (Nov. 2017), p. 31148. DOI: 10.1364/oe.25.031148.
- [74] Alan S. Pine. “Brillouin Scattering Study of Acoustic Attenuation in Fused Quartz”. In: *Physical Review* 185.3 (Sept. 1969), pp. 1187–1193. DOI: 10.1103/physrev.185.1187.
- [75] Gregory W. Faris et al. “High-resolution Brillouin gain spectroscopy in fused silica”. In: *Optics Letters* 15.12 (June 1990), p. 703. DOI: 10.1364/ol.15.000703.
- [76] David Griffiths. *Introduction to electrodynamics*. Boston: Pearson Education, 2013. ISBN: 9780321856562.
- [77] N.M. Kondratiev and M.L. Gorodetsky. “Thermorefractive noise in whispering gallery mode microresonators: Analytical results and numerical simulation”. In: *Physics Letters A* 382.33 (Aug. 2018), pp. 2265–2268. DOI: 10.1016/j.physleta.2017.04.043.
- [78] Andrey B. Matsko et al. “Whispering-gallery-mode resonators as frequency references I Fundamental limitations”. In: *Journal of the Optical Society of America B* 24.6 (May 2007), p. 1324. DOI: 10.1364/josab.24.001324.
- [79] Alexey E. Fomin et al. “Nonstationary nonlinear effects in optical microspheres”. In: *Journal of the Optical Society of America B* 22.2 (Feb. 2005), p. 459. DOI: 10.1364/josab.22.000459.
- [80] Qing Li et al. “Stably accessing octave-spanning microresonator frequency combs in the soliton regime”. In: *Optica* 4.2 (Feb. 2017), p. 193. DOI: 10.1364/optica.4.000193.
- [81] T. Carmon, L. Yang, and K. J. Vahala. “Dynamical thermal behavior and thermal self-stability of microcavities”. In: *Optics Express* 12.20 (2004), pp. 4742–4750. DOI: 10.1364/OPEX.12.004742.

- [82] Stefano Grillanda et al. “Post-fabrication trimming of athermal silicon waveguides”. In: *Optics Letters* 38.24 (Dec. 2013), p. 5450. DOI: 10.1364/ol.38.005450.
- [83] Vivek Raghunathan et al. “Athermal operation of Silicon waveguides: spectral, second order and footprint dependencies”. In: *Optics Express* 18.17 (Aug. 2010), p. 17631. DOI: 10.1364/oe.18.017631.
- [84] François Copie et al. “Interplay of Polarization and Time-Reversal Symmetry Breaking in Synchronously Pumped Ring Resonators”. In: *Physical Review Letters* 122.1 (Jan. 2019). DOI: 10.1103/physrevlett.122.013905.
- [85] M. Haelterman, S. Trillo, and S. Wabnitz. “Polarization multistability and instability in a nonlinear dispersive ring cavity”. In: *Journal of the Optical Society of America B* 11.3 (Mar. 1994), p. 446. DOI: 10.1364/josab.11.000446.
- [86] Mark Oxborrow. “Traceable 2-D Finite-Element Simulation of the Whispering-Gallery Modes of Axisymmetric Electromagnetic Resonators”. In: *IEEE Transactions on Microwave Theory and Techniques* 55.6 (June 2007), pp. 1209–1218. DOI: 10.1109/tmtt.2007.897850.
- [87] Leonardo Del Bino et al. “Symmetry Breaking of Counter-Propagating Light in a Nonlinear Resonator”. In: *Scientific Reports* 7 (Feb. 2017), p. 43142. DOI: 10.1038/srep43142.
- [88] Ivan S. Grudin and Nan Yu. “Dispersion engineering of crystalline resonators via microstructuring”. In: *Optica* 2.3 (Mar. 2015), p. 221. DOI: 10.1364/optica.2.000221.
- [89] Tzyy-Jiann Wang et al. “On-Chip Optical Microresonators With High Electro-Optic Tuning Efficiency”. In: *Journal of Lightwave Technology* 38.7 (Apr. 2020), pp. 1851–1857. DOI: 10.1109/jlt.2019.2959345.
- [90] B. Gayral et al. “High-Q wet-etched GaAs microdisks containing InAs quantum boxes”. In: *Applied Physics Letters* 75.13 (Sept. 1999), pp. 1908–1910. DOI: 10.1063/1.124894.
- [91] M. Borghi et al. “Nonlinear silicon photonics”. In: *Journal of Optics* 19.9 (2017), p. 093002. DOI: 10.1088/2040-8986/aa7a6d.

- [92] Yi Xuan et al. “High-Q silicon nitride microresonators exhibiting low-power frequency comb initiation”. In: *Optica* 3.11 (Oct. 2016), p. 1171. DOI: 10.1364/optica.3.001171.
- [93] Xiaomin Zhang and Andrea M. Armani. “Silica microtoroid resonator sensor with monolithically integrated waveguides”. In: *Optics Express* 21.20 (Sept. 2013), p. 23592. DOI: 10.1364/oe.21.023592.
- [94] D. K. Armani et al. “Ultra-high-Q toroid microcavity on a chip”. In: *Nature* 421.6926 (Feb. 2003), pp. 925–928. DOI: 10.1038/nature01371.
- [95] B. E. Deal and A. S. Grove. “General Relationship for the Thermal Oxidation of Silicon”. In: *Journal of Applied Physics* 36.12 (Dec. 1965), pp. 3770–3778. DOI: 10.1063/1.1713945.
- [96] Dale E. Ibbotson et al. “Comparison of XeF₂ and F-atom reactions with Si and SiO₂”. In: *Applied Physics Letters* 44.12 (June 1984), pp. 1129–1131. DOI: 10.1063/1.94665.
- [97] H. F. Winters and J. W. Coburn. “The etching of silicon with XeF₂vapor”. In: *Applied Physics Letters* 34.1 (Jan. 1979), pp. 70–73. DOI: 10.1063/1.90562.
- [98] Hansuek Lee et al. “Chemically etched ultrahigh-Q wedge-resonator on a silicon chip”. In: *Nature Photonics* 6.6 (May 2012), pp. 369–373. DOI: 10.1038/nphoton.2012.109.
- [99] Misha Sumetsky. “Lasing microbottles”. In: *Light: Science & Applications* 6.10 (Oct. 2017), e17102–e17102. DOI: 10.1038/lsa.2017.102.
- [100] Jonathan M. Ward, Yong Yang, and Sile Nic Chormaic. “Glass-on-Glass Fabrication of Bottle-Shaped Tunable Microlasers and their Applications”. In: *Scientific Reports* 6.1 (Apr. 2016). DOI: 10.1038/srep25152.
- [101] Sivaraman Subramanian et al. “Label-Free Optical Single-Molecule Micro- and Nanosensors”. In: *Advanced Materials* 30.51 (Aug. 2018), p. 1801246. DOI: 10.1002/adma.201801246.
- [102] Erol Ozgur et al. “Label-Free Biosensing with High Selectivity in Complex Media using Microtoroidal Optical Resonators”. In: *Scientific Reports* 5.1 (Aug. 2015). DOI: 10.1038/srep13173.

- [103] Jianguang Zhu et al. “On-chip single nanoparticle detection and sizing by mode splitting in an ultrahigh-Q microresonator”. In: *Nature Photonics* 4.1 (Dec. 2009), pp. 46–49. DOI: 10.1038/nphoton.2009.237.
- [104] Pengfei Wang et al. “Lead-silicate glass optical microbubble resonator”. In: *Applied Physics Letters* 106.6 (Feb. 2015), p. 061101. DOI: 10.1063/1.4908054.
- [105] G. Persichetti et al. “Self-assembling and packaging of microbottle resonators for all-polymer lab-on-chip platform”. In: *Sensors and Actuators A: Physical* 280 (Sept. 2018), pp. 271–276. DOI: 10.1016/j.sna.2018.07.055.
- [106] Ming-Chun Tien et al. “Ultra-low loss Si₃N₄ waveguides with low nonlinearity and high power handling capability”. In: *Optics Express* 18.23 (Oct. 2010), p. 23562. DOI: 10.1364/oe.18.023562.
- [107] M. Ferrera et al. “Low-power continuous-wave nonlinear optics in doped silica glass integrated waveguide structures”. In: *Nat Photon* 2.12 (2008), pp. 737–740. ISSN: 1749-4885. URL: <http://dx.doi.org/10.1038/nphoton.2008.228>.
- [108] Zhiping Zhou, Bing Yin, and Jurgen Michel. “On-chip light sources for silicon photonics”. In: *Light: Science & Applications* 4.11 (Nov. 2015), e358. DOI: 10.1038/lsa.2015.131.
- [109] N. Lindenmann et al. “Photonic wire bonding: a novel concept for chip-scale interconnects”. In: *Optics Express* 20.16 (July 2012), p. 17667. DOI: 10.1364/oe.20.017667.
- [110] A.W. Snyder and J. Love. *Optical Waveguide Theory*. Chapman & Hall, 1983. ISBN: 978-0-412-09950-2.
- [111] J. M. Ward et al. “Contributed Review: Optical micro- and nanofiber pulling rig”. In: *Review of Scientific Instruments* 85.11 (Nov. 2014), p. 111501. DOI: 10.1063/1.4901098.
- [112] Anatoliy A. Savchenkov et al. “Generation of Kerr combs centered at 4.5 μ m in crystalline microresonators pumped with quantum-cascade lasers”. In: *Optics Letters* 40.15 (July 2015), p. 3468. DOI: 10.1364/ol.40.003468.

- [113] Ivan S. Grudinin, Kamjou Mansour, and Nan Yu. “Properties of fluoride microresonators for mid-IR applications”. In: *Optics Letters* 41.10 (2016), p. 2378. DOI: 10.1364/ol.41.002378.
- [114] Anatoliy A. Savchenkov et al. “Optical resonators with ten million finesse”. In: *Optics Express* 15.11 (2007), p. 6768. DOI: 10.1364/oe.15.006768.
- [115] I. H. Malitson. “Interspecimen Comparison of the Refractive Index of Fused Silica”. In: *Journal of the Optical Society of America* 55.10 (Oct. 1965), p. 1205. DOI: 10.1364/josa.55.001205.
- [116] Marilyn J. Dodge. “Refractive properties of magnesium fluoride”. In: *Applied Optics* 23.12 (June 1984), p. 1980. DOI: 10.1364/ao.23.001980.
- [117] Masahiko Daimon and Akira Masumura. “High-accuracy measurements of the refractive index and its temperature coefficient of calcium fluoride in a wide wavelength range from 138 to 2326 nm”. In: *Applied Optics* 41.25 (Sept. 2002), p. 5275. DOI: 10.1364/ao.41.005275.
- [118] Kevin Luke et al. “Broadband mid-infrared frequency comb generation in a Si₃N₄ microresonator”. In: *Optics Letters* 40.21 (Oct. 2015), p. 4823. DOI: 10.1364/ol.40.004823.
- [119] Makan Mohageg, Anatoliy A. Savchenkov, and Lute Maleki. “High-Q optical whispering gallery modes in elliptical LiNbO₃ resonant cavities”. In: *Optics Express* 15.8 (2007), p. 4869. DOI: 10.1364/oe.15.004869.
- [120] George N. Ghalanos et al. “Direct Measurement of Cross-Phase Modulation in Microresonators”. In: *2019 Conference on Lasers and Electro-Optics Europe & European Quantum Electronics Conference (CLEO/Europe-EQEC)*. IEEE, June 2019. DOI: 10.1109/cleoe-eqec.2019.8872237.
- [121] Michael T. M. Woodley et al. “Universal symmetry-breaking dynamics for the Kerr interaction of counterpropagating light in dielectric ring resonators”. In: *Physical Review A* 98.5 (Nov. 2018). DOI: 10.1103/physreva.98.053863.
- [122] Lewis Hill et al. “Effects of self- and cross-phase modulation on the spontaneous symmetry breaking of light in ring resonators”. In: *Physical Review A* 101.1 (Jan. 2020). DOI: 10.1103/physreva.101.013823.

- [123] Qi-Tao Cao et al. “Experimental Demonstration of Spontaneous Chirality in a Nonlinear Microresonator”. In: *Phys. Rev. Lett.* 118 (3 2017), p. 033901. DOI: 10.1103/PhysRevLett.118.033901.
- [124] Bahaa E. A. Saleh and Malvin Carl Teich. *Fundamentals of Photonics*. John Wiley & Sons, Inc., Aug. 1991. DOI: 10.1002/0471213748.
- [125] R. J. Potton. “Reciprocity in optics”. In: *Reports On Progress In Physics* 67.5 (2004), p. 717. DOI: 10.1088/0034-4885/67/5/R03.
- [126] Dirk Jalas et al. “What is — and what is not — an optical isolator”. In: *Nature Photonics* 7.8 (2013), pp. 579–582. DOI: 10.1038/nphoton.2013.185.
- [127] Liang Feng et al. “Nonreciprocal Light Propagation in a Silicon Photonic Circuit”. In: *Science* 333.6043 (2011), pp. 729–733. DOI: 10.1126/science.1206038.
- [128] L. Fan et al. “An All-Silicon Passive Optical Diode”. In: *Science* 335.6067 (2011), pp. 447–450. DOI: 10.1126/science.1214383.
- [129] Yu Shi, Zongfu Yu, and Shanhui Fan. “Limitations of nonlinear optical isolators due to dynamic reciprocity”. In: *Nature Photonics* 9.6 (2015), pp. 388–392. DOI: 10.1038/nphoton.2015.79.
- [130] H Dotsch et al. “Applications of magneto-optical waveguides in integrated optics: review”. In: *Journal of the Optical Society of America B-Optical Physics* 22.1 (2005), 240–253. ISSN: 0740-3224. DOI: 10.1364/JOSAB.22.000240.
- [131] Yuya Shoji et al. “Magneto-optical isolator with silicon waveguides fabricated by direct bonding”. In: *Applied Physics Letters* 92.7 (2008). ISSN: 0003-6951. DOI: 10.1063/1.2884855.
- [132] Lei Bi et al. “On-chip optical isolation in monolithically integrated non-reciprocal optical resonators”. In: *Nature Photonics* 5.12 (2011), pp. 758–762. DOI: <https://doi.org/10.1038/nphoton.2011.270>.
- [133] Naoya Kono et al. “Nonreciprocal microresonators for the miniaturization of optical waveguide isolators”. In: *Optics express* 15.12 (2007), pp. 7737–7751. DOI: 10.1364/OE.15.007737.
- [134] Paolo Pintus, Fabrizio Di Pasquale, and John E. Bowers. “Integrated TE and TM optical circulators on ultra-low-loss silicon nitride platform”. In: *Optics Express* 21.4 (2013), p. 5041. DOI: 10.1364/oe.21.005041.

- [135] Paolo Pintus et al. “Microring-Based Optical Isolator and Circulator with Integrated Electromagnet for Silicon Photonics”. In: *Journal of Lightwave Technology* 35.8 (2017), pp. 1429–1437. DOI: 10.1109/jlt.2016.2644626.
- [136] K Gallo et al. “All-optical diode in a periodically poled lithium niobate waveguide”. In: *Applied Physics Letters* 79.3 (2001), 314–316. ISSN: 0003-6951. DOI: 10.1063/1.1386407.
- [137] K. Fang et al. “Generalized non-reciprocity in an optomechanical circuit via synthetic magnetism and reservoir engineering”. In: *Nature Physics* 13 (2017), pp. 465–471. DOI: 10.1038/nphys4009.
- [138] Sasikanth Manipatruni, Jacob T Robinson, and Michal Lipson. “Optical non-reciprocity in optomechanical structures”. In: *Physical review letters* 102.21 (2009), p. 213903. DOI: 10.1103/physrevlett.102.213903.
- [139] Freek Ruesink et al. “Nonreciprocity and magnetic-free isolation based on optomechanical interactions”. In: *Nature Communications* 7 (2016). DOI: 10.1038/ncomms13662.
- [140] Zhen Shen et al. “Experimental realization of optomechanically induced non-reciprocity”. In: *Nature Photonics* (2016). DOI: 10.1038/nphoton.2016.161.
- [141] Zheqi Wang et al. “Optical nonreciprocity in asymmetric optomechanical couplers”. In: *Scientific reports* 5 (2015). DOI: 10.1038/srep08657.
- [142] Long Chang et al. “Parity-time symmetry and variable optical isolation in active-passive-coupled microresonators”. In: *Nat Photon* 8.7 (2014), pp. 524–529. ISSN: 1749-4885. DOI: 10.1038/nphoton.2014.133.
- [143] Bo Peng et al. “Parity-time-symmetric whispering-gallery microcavities”. In: *Nature Physics* 10.5 (2014), pp. 394–8. DOI: 10.1038/nphys2927.
- [144] Hugo Lira et al. “Electrically Driven Nonreciprocity Induced by Interband Photonic Transition on a Silicon Chip”. In: *Physical Review Letters* 109.3 (2012). ISSN: 0031-9007. DOI: 10.1103/PhysRevLett.109.033901.
- [145] Zongfu Yu and Shanhui Fan. “Complete optical isolation created by indirect interband photonic transitions”. In: *Nature Photonics* 3.2 (2009), pp. 91–94. DOI: 10.1038/NPHOTON.2008.273.

- [146] Xinpeng Huang and Shanhui Fan. “Complete all-optical silica fiber isolator via stimulated Brillouin scattering”. In: *Journal of Lightwave Technology* 29.15 (2011), pp. 2267–2275.
- [147] MS Kang, A Butsch, and P St J Russell. “Reconfigurable light-driven optoacoustic isolators in photonic crystal fibre”. In: *Nature Photonics* 5.9 (2011), pp. 549–553.
- [148] G. Frigenti et al. “Coupling analysis of high Q resonators in add-drop configuration through cavity ringdown spectroscopy”. In: *Journal of Optics* 20.6 (May 2018), p. 065706. DOI: 10.1088/2040-8986/aac459.
- [149] F. Monifi et al. “A Robust and Tunable Add-Drop Filter Using Whispering Gallery Mode Microtoroid Resonator”. In: *IEEE J. of Lightwave Tech.*, 30, 3306-3315 (2012) (Apr. 27, 2013). DOI: 10.1109/JLT.2012.2214026. arXiv: <http://arxiv.org/abs/1304.7315v1> [physics.optics].
- [150] A. Yariv. “Critical coupling and its control in optical waveguide-ring resonator systems”. In: *IEEE Photonics Technology Letters* 14.4 (Apr. 2002), pp. 483–485. DOI: 10.1109/68.992585.
- [151] Mikhail N. Polyanskiy. *Refractive index database*. <https://refractiveindex.info>.
- [152] Jan Kischkat et al. “Mid-infrared optical properties of thin films of aluminum oxide, titanium dioxide, silicon dioxide, aluminum nitride, and silicon nitride”. In: *Applied Optics* 51.28 (Sept. 2012), p. 6789. DOI: 10.1364/ao.51.006789.
- [153] A. A. Savchenkov et al. “Stabilization of a Kerr frequency comb oscillator”. In: *Optics Letters* 38.15 (July 2013), p. 2636. DOI: 10.1364/ol.38.002636.
- [154] Brian Stern et al. “Battery-operated integrated frequency comb generator”. In: *Nature* 562.7727 (Oct. 2018), pp. 401–405. DOI: 10.1038/s41586-018-0598-9.
- [155] François Leo et al. “Temporal cavity solitons in one-dimensional Kerr media as bits in an all-optical buffer”. In: *Nature Photonics* 4.7 (May 2010), pp. 471–476. DOI: 10.1038/nphoton.2010.120.

- [156] Stéphane Coen et al. “Modeling of octave-spanning Kerr frequency combs using a generalized mean-field Lugiato–Lefever model”. In: *Optics Letters* 38.1 (Dec. 2012), p. 37. DOI: 10.1364/ol.38.000037.
- [157] Yanne K. Chembo and Curtis R. Menyuk. “Spatiotemporal Lugiato-Lefever formalism for Kerr-comb generation in whispering-gallery-mode resonators”. In: *Physical Review A* 87.5 (May 2013). DOI: 10.1103/physreva.87.053852.
- [158] François Leo et al. “Dynamics of one-dimensional Kerr cavity solitons”. In: *Optics Express* 21.7 (Apr. 2013), p. 9180. DOI: 10.1364/oe.21.009180.
- [159] Jonathan M. Silver, Kenneth T. V. Grattan, and Pascal Del’Haye. “Critical Dynamics of an Asymmetrically Bidirectionally Pumped Optical Microresonator”. In: (Dec. 17, 2019). arXiv: 1912.08262v1 [physics.optics].
- [160] C. Runge. “Ueber die numerische Auflosung von Differentialgleichungen”. In: *Mathematische Annalen* 46.2 (June 1895), pp. 167–178. DOI: 10.1007/bf01446807.
- [161] Mengjie Yu et al. “Mode-locked mid-infrared frequency combs in a silicon microresonator”. In: *Optica* 3.8 (2016), p. 854. DOI: 10.1364/optica.3.000854.
- [162] Deane Chandler-Horowitz and Paul M. Amirtharaj. “High-accuracy, midinfrared (450 cm⁻¹ - 4000 cm⁻¹) refractive index values of silicon”. In: *Journal of Applied Physics* 97.12 (June 2005), p. 123526. DOI: 10.1063/1.1923612.
- [163] Q. Lin et al. “Dispersion of silicon nonlinearities in the near infrared region”. In: *Applied Physics Letters* 91.2 (2007), p. 021111. DOI: 10.1063/1.2750523.
- [164] Carlos Errando-Herranz et al. “MEMS for Photonic Integrated Circuits”. In: *IEEE Journal of Selected Topics in Quantum Electronics* 26.2 (Mar. 2020), pp. 1–16. DOI: 10.1109/jstqe.2019.2943384.
- [165] S.M.C. Abdulla et al. “Tuning a racetrack ring resonator by an integrated dielectric MEMS cantilever”. In: *Optics Express* 19.17 (2011), p. 15864. DOI: 10.1364/oe.19.015864.
- [166] Kai Chen, Fei Duan, and Yonglin Yu. “High-performance thermo-optic tunable grating filters based on laterally supported suspended silicon ridge waveguide”. In: *Optics Express* 26.15 (2018), p. 19479. DOI: 10.1364/oe.26.019479.

- [167] Zhen Chai et al. “Ultrafast All-Optical Switching”. In: *Advanced Optical Materials* 5.7 (Dec. 2016), p. 1600665. DOI: 10.1002/adom.201600665.
- [168] Carlos Rios et al. “Integrated all-photonics non-volatile multi-level memory”. In: *Nature Photonics* 9.11 (Sept. 2015), pp. 725–732. DOI: 10.1038/nphoton.2015.182.
- [169] S. R. Friberg et al. “Ultrafast all-optical switching in a dual-core fiber nonlinear coupler”. In: *Applied Physics Letters* 51.15 (Oct. 1987), pp. 1135–1137. DOI: 10.1063/1.98762.
- [170] R. Takahashi, Y. Kawamura, and H. Iwamura. “Ultrafast 1.55 μm all-optical switching using low-temperature-grown multiple quantum wells”. In: *Applied Physics Letters* 68.2 (Jan. 1996), pp. 153–155. DOI: 10.1063/1.116131.
- [171] Changjun Min et al. “All-optical switching in subwavelength metallic grating structure containing nonlinear optical materials”. In: *Optics Letters* 33.8 (Apr. 2008), p. 869. DOI: 10.1364/ol.33.000869.
- [172] Marc Currie. “Low-temperature grown Gallium Arsenide (LT-GaAs) high-speed detectors”. In: *Photodetectors*. Elsevier, 2016, pp. 121–155. DOI: 10.1016/b978-1-78242-445-1.00005-1.
- [173] S. Osborne et al. “All-optical memory based on the injection locking bistability of a two-color laser diode”. In: *Optics Express* 17.8 (Apr. 2009), p. 6293. DOI: 10.1364/oe.17.006293.
- [174] Y. Liu et al. “Three-state all-optical memory based on coupled ring lasers”. In: *IEEE Photonics Technology Letters* 15.10 (Oct. 2003), pp. 1461–1463. DOI: 10.1109/lpt.2003.818221.
- [175] Liu Liu et al. “An ultra-small, low-power, all-optical flip-flop memory on a silicon chip”. In: *Nature Photonics* 4.3 (Jan. 2010), pp. 182–187. DOI: 10.1038/nphoton.2009.268.
- [176] Chin-Hui Chen et al. “All-optical memory based on injection-locking bistability in photonic crystal lasers”. In: *Optics Express* 19.4 (Feb. 2011), p. 3387. DOI: 10.1364/oe.19.003387.
- [177] Martin T. Hill et al. “A fast low-power optical memory based on coupled micro-ring lasers”. In: *Nature* 432.7014 (Nov. 2004), pp. 206–209. DOI: 10.1038/nature03045.

- [178] Akihiko Shinya et al. “All-optical on-chip bit memory based on ultra high Q InGaAsP photonic crystal”. In: *Optics Express* 16.23 (Nov. 2008), p. 19382. DOI: 10.1364/oe.16.019382.
- [179] Kengo Nozaki et al. “All-optical switching for 10-Gb/s packet data by using an ultralow-power optical bistability of photonic-crystal nanocavities”. In: *Optics Express* 23.23 (2015), p. 30379. DOI: 10.1364/oe.23.030379.
- [180] Marin Soljačić et al. “Optimal bistable switching in nonlinear photonic crystals”. In: *Physical Review E* 66.5 (2002). DOI: 10.1103/physreve.66.055601.
- [181] Takasumi Tanabe et al. “Fast bistable all-optical switch and memory on a silicon photonic crystal on-chip”. In: *Optics Letters* 30.19 (Oct. 2005), p. 2575. DOI: 10.1364/ol.30.002575.
- [182] Masaya Notomi et al. “Optical bistable switching action of Si high-Q photonic-crystal nanocavities”. In: *Optics Express* 13.7 (2005), p. 2678. DOI: 10.1364/opex.13.002678.
- [183] Hitoshi Nakamura et al. “Ultra-fast photonic crystal/quantum dot alloptical switch for future photonic networks”. In: *Optics Express* 12.26 (2004), p. 6606. DOI: 10.1364/opex.12.006606.
- [184] Y. Henry Wen et al. “All-Optical Control of an Individual Resonance in a Silicon Microresonator”. In: *Physical Review Letters* 108.22 (June 2012). DOI: 10.1103/physrevlett.108.223907.
- [185] Vilson R. Almeida and Michal Lipson. “Optical bistability on a silicon chip”. In: *Optics Letters* 29.20 (2004), p. 2387. DOI: 10.1364/ol.29.002387.
- [186] Xu Fang et al. “Ultrafast all-optical switching via coherent modulation of metamaterial absorption”. In: *Applied Physics Letters* 104.14 (Apr. 2014), p. 141102. DOI: 10.1063/1.4870635.
- [187] Lei Chen et al. “Chip-scale nanophotonic switch based on a waveguide-metamaterial coupling mechanism”. In: *Optics Letters* 42.20 (2017), p. 4199. DOI: 10.1364/ol.42.004199.
- [188] Wataru Yoshiki and Takasumi Tanabe. “All-optical switching using Kerr effect in a silica toroid microcavity”. In: *Optics Express* 22.20 (Sept. 2014), p. 24332. DOI: 10.1364/oe.22.024332.

- [189] Yu-Long Liu et al. “Controllable optical response by modifying the gain and loss of a mechanical resonator and cavity mode in an optomechanical system”. In: *Phys. Rev. A* 95 (1 Jan. 2017), p. 013843. DOI: 10.1103/PhysRevA.95.013843. URL: <https://link.aps.org/doi/10.1103/PhysRevA.95.013843>.
- [190] Wataru Yoshiki and Takasumi Tanabe. “Performance of Kerr bistable memory in silicon nitride microring and silica microtoroid”. In: *Japanese Journal of Applied Physics* 53.12 (Nov. 2014), p. 122202. DOI: 10.7567/jjap.53.122202.
- [191] Ruiqiang Ji et al. “Microring-resonator-based four-port optical router for photonic networks-on-chip”. In: *Optics Express* 19.20 (Sept. 2011), p. 18945. DOI: 10.1364/oe.19.018945.
- [192] Herbert B. *A Mathematical Introduction to Logic*. Elsevier Science Publishing Co Inc, Jan. 23, 2001. 336 pp. ISBN: 0122384520.
- [193] Maxwell Rowley et al. “Thermo-optical pulsing in a microresonator filtered fiber-laser: a route towards all-optical control and synchronization”. In: *Optics Express* 27.14 (June 2019), p. 19242. DOI: 10.1364/oe.27.019242.
- [194] Yoshitomo Okawachi et al. “Octave-spanning frequency comb generation in a silicon nitride chip”. In: *Optics Letters* 36.17 (Aug. 2011), p. 3398. DOI: 10.1364/ol.36.003398.
- [195] Wesley D. Sacher et al. “Multilayer Silicon Nitride-on-Silicon Integrated Photonic Platform for 3D Photonic Circuits”. In: *Conference on Lasers and Electro-Optics*. Demonstration of the viability of silicon nitride optical circuits. OSA, 2016. DOI: 10.1364/cleo_at.2016.jth4c.3.
- [196] Jonathan M. Silver et al. “A Nonlinear Enhanced Microresonator Gyroscope”. In: (Jan. 15, 2020). arXiv: 2001.05479v1 [physics.optics].
- [197] P. Trocha et al. “Ultrafast optical ranging using microresonator soliton frequency combs”. In: *Science* 359.6378 (Feb. 2018). presented by Michael at literature club, pp. 887–891. DOI: 10.1126/science.aao3924.